Electronic Transport and Photoconductive Properties of Resorcinol-Formaldehyde-Based Carbon Aerogels

by

Gillian Althea Maria Reynolds

B.A./M.A., Hunter College of CUNY (1989)

Submitted to the Department of Physics
in partial fulfillment of the requirements for the degree of

Doctor of Philosophy in Physics

at the

MASSACHUSETTS INSTITUTE OF TECHNOLOGY

September 1995

Author .....
Department of Physics
July 27, 1995

Certified by .....
Mildred S. Dresselhaus
Institute Professor
Thesis Supervisor

Accepted by .....
Prof. George F. Koster
Chairman, Physics Graduate Committee

Electronic Transport and Photoconductive Properties of Resorcinol-Formaldehyde-Based Carbon Aerogels

by

Gillian Althea Maria Reynolds

Submitted to the Department of Physics
on July 27, 1995, in partial fulfillment of the
requirements for the degree of
Doctor of Philosophy in Physics

Abstract

Carbon aerogels are a new class of low-density micro-cellular materials derived from a chemical sol-gel polymerization of various precursors (resorcinol-formaldehyde (RF) or phenolic-furfural (PF)) which allows the tailoring of the internal structure of these porous materials on a nanometer scale. In general, carbon aerogels have an interconnected porosity with large specific surface areas (500 - 800 m^2/g), low mass densities, ($\rho_m \sim 0.1 - 0.6$ g/cm^3), and a solid matrix composed of interconnected particles (grains). For the RF-based carbon aerogels, the grain sizes can be chemically varied from $\sim$ 70 Å to 150 Å, resulting in *colloidal* and *polymeric* carbon aerogels.

The carbon aerogel provides a way of examining a highly disordered cluster-assembled system. By varying parameters such as the density, particle size and heat-treatment temperature, a model platform of disorder could be created for study. Effects of these externally controllable parameters on the internal structure and properties of the carbon aerogel material were examined using techniques such as room-temperature Raman spectroscopy and TEM, temperature-dependent dark- and photoconductivity, magnetoresistance and magnetic susceptibility.

For the solid matrix, the conductivity exhibits an $\exp[-\sqrt{T_0/T}]$ dependence for all samples at low temperature. This strong localization behaviour can be explained by a Coulomb gap variable range hopping mechanism, and this identification has been further corroborated by low-temperature magnetoresistance data obtained in magnetic fields up to 15 Tesla. The results suggest that the particles (grains) themselves, and not the defect states, act as carrier localization sites in these materials. A model has been proposed to explain the observed temperature-dependence of the photoconductivity, which has been attributed to photoholes present in the system. A novel TEM imaging analysis technique has allowed visualization of the mesopores and an inference of the fractal dimension, D, of polymeric and colloidal carbon aerogels.

Thesis Supervisor: Mildred S. Dresselhaus
Title: Institute Professor

To my parents:

mummy, daddy and mama

Acknowledgments

It took many years for me to get to this point in my life, and there are many people who played pivotal roles in this process.

First, I would like to thank my thesis advisor, Prof. Mildred Dresselhaus. She is very understanding and helpful with all her students, always remembering the human being that has to factor into the equation. She has taught me a lot about what it means to be a physicist and how to interact with people on a scientific and a personal level. She has also impressed upon me the need to excel in all aspects of life. Thanks also to Dr. Gene Dresselhaus for his scientific comments and help with papers (and all things LaTeX). There is a lot of potential in the present MGM gang: Manyalibo, Boris, Lyndon, James, Siegfried, Sun, Nathan and Joe, have been good at challenging my ideas and knowing the right questions to ask. Other MGMers such as Drs. Alex Fung and Joey Wang have been very instrumental in helping me with setting up my experiments, data interpretation and presentation. Then there is Laura, the secretary to the Dresselhaus', who has been very efficient at helping to organize my paperwork for conferences and journals, making the load a little lighter.

I have had the opportunity while here to colloborate with people from as far away as Japan and California. The interactions always left me with a new way to approach the answers to the questions being asked. Thanks to Dr. Moodera and Prof. Endo for their interest in my work. Thanks especially to Dr. Pekala and Cynthia Alviso at Livermore for their guidance during my visit there. Dr. Pekala has also been instrumental in my work, providing me with samples and new ideas and approaches, from a chemist's point of view.

Financially speaking, I could never dream of attending graduate school at MIT if not for the funding from the National Institutes of Health, the Physics department and Lawrence Livermore National Laboratory. Peggy Berkovitz has been wonderful in keeping all the financial paperwork straight. However, to me she is more than just the physics graduate administrator. She is a friend who always greets you with a smile, and she has been pretty helpful in terms of keeping me cheerful and encouraged.

I have to acknowledge Dr. Steven Greenbaum, my undergraduate advisor who always has my best interests in mind. Whatever the difficulties I faced here, he always bet on me, and has never lost. He is amazed that I still ask for his opinions on things, but this just attests to the fact that I consider him very influential in my physics career and value his opinion.

But my time here has not all been roses. MIT is a tough place, academically and socially. I will not gripe here, but I will say this: the good times were great, though few and far between, and the bad times were simply horrific, but very frequent. I could write a whole chapter on my painful experiences here, but that would be futile. Instead, I will concentrate my efforts on thanking the other people here that provided lifelong friendships and helped to make the good times wonderful for me. If not for Dr. Frank DiFilippo and Michael Titko, I would have lost more of my mind. Thank you both for being there for me in your own very special ways; for always having a literal shoulder for me to cry on and for knowing what to do to keep me focused, motivated and chugging ahead. Pamela Blakeslee, Marta Dark and Sandra Brown have been just wonderful! We shared a lot of emotions together, as well as a lot of shopping, movies, lunches and knitting party get-togethers. Thanks to Dr. Côté for always having those great parties at just about the right time :) To the folks in the Tae Kwon Do club: Ron (& Nina), Ian, Steve, Brent, Lim, Karin, Arabella, Chris and Chris.....Thanks a bunch for the lessons and the nights at the Sunset!

To my West coast friends, Aaron Wynn and Meng Chiao, thanks for making your homes open and welcoming to me on a moments' notice. Aaron, thanks so much for taking those 3 am calls :)

To the people outside my physics world, Patrick Stewart and my 'sister' Charmaine Bartley, my cousins, uncles and aunts. Thanks for encouraging me and making me remember that there are other things of importance in life beyond these concrete-coloured columns of MIT.

Most importantly, to my mother, father and grandmother. Thank you for your prayers, your understanding, your encouragement, your support and your love.

Contents

List of Figures

List of Tables

Chapter 1

Introduction

Graphite assumes many forms, and it is this variety that makes this material of such widespread academic and commercial interest. One can go from highly oriented pyrolytic graphite to the more disordered amorphous forms of carbon. Although the local structure common to all these varied forms of carbon is graphitic in nature, differences in the microstructure lead to major changes in physical properties. As new forms of graphite and carbon are discovered, it is important to classify them in terms of their structure-property relationships.

Carbon aerogels are a form of cluster-assembled porous carbons which exhibit relatively large specific surface areas (500 - 1000 m^2/gm), low mass densities (0.1 - 0.9 g/cm^3 in this work) and an intricate structural morphology of macropores ($>$ 50 nm), mesopores (2 - 50 nm) and nanopores ($<$ 2 nm). These physical characteristics have resulted in aerogels being used in various new technological advances. For example, advantage is being taken of the large specific surface areas of the carbon aerogel in "aerocapacitors" [1]. Here, the carbon aerogel is being used as the electrode. The low thermal conductivities (see Table 2.1) are advantageous as insulation in windows. The porous nature is being used, among other things, as filters for poisonous compounds [2] and even as part of a prototype water filtering system [3].

New ways of using the aerogel are always being sought. By understanding the properties of these materials on a microscopic level, insight can gained into how they should be engineered for further viable technological use. In this vein, general techniques such as Brunauer-Emmett-Teller (BET) adsorption and small angle x-ray scattering have been used to examine the microstructure [4, 5, 6].

This work describes a systematic study done on carbon aerogels to not only understand the structure of these disordered carbon materials, but also to see how the structure relates to the observed electrical and optical properties. Most of the prior work done on these materials concentrated on their thermal properties and the structure and distribution of the porous network, using such techniques as gas adsorption, bulk moduli and thermal and mechanical studies [7, 8]. The work of this thesis is aimed at understanding the role the solid matrix plays in the electrical transport and photoconductive properties and takes the following format.

Chapter 2 reviews the experiments used to determine the structure of the aerogel material. Complementing the above-mentioned techniques with Raman spectroscopy gives a measure of the in-plane microcrystallite size as well as a measure of how homogeneous or ordered these materials are. Magnetic susceptibility studies have also been useful in determining the unpaired spin concentration as well as the amount of diamagnetism in these systems. Transmission electron microscopy (TEM) studies have been used mostly to examine the nanopores contained within the particles making up the carbon aerogel. Recently, TEM studies have been carried out to find the size distribution and shapes of the mesopores, as well as their fractal nature.

As the carbon aerogels are chemically tailorable, i.e., variations in chemical synthesis result in different morphologies and physical properties, we can create a model platform spanning the most disordered to the least disordered porous carbon aerogel. By using other tools such as electrical transport, magnetoresistance and photoconductivity, these materials have been characterized in terms of the effects of variations in mass density, heat-treatment temperature, specific surface area and particle size

over a wide range of disorder.

Chapter 3 summarizes the electrical transport measurements and there it is found that the most disordered carbon aerogels exhibit strong localization effects at low temperatures. By increasing the heat-treatment temperature, mass density and particle size, this localization effect can be reduced. In this way, changes in physical properties can be tracked as the system moves from an insulating to a more metallic state. The localization sites are also of interest. As the morphology of these materials lends itself to disorder, the question of what physical structures played the role of localization sites, the particles or the dangling bonds, was a question that was unanswered for some time. By studying the susceptibility and conductivity of carbon aerogels with various particle sizes, we were able to conclude that the localization sites were due to the particles themselves. This result was also important in confirming the transport mechanism at low temperatures, which has been proposed as Coulomb-gap variable range hopping. Further studies with magnetoresistance as a tool were also conducted to confirm the low-temperature transport mechanism. These studies have shown that the proposed transport mechanism is robust, even with changes in particle size and morphology.

Chapter 4 examines the temperature-dependent photoconductivity which shows the existence of a peak at low temperatures. On the low temperature side of the peak, the behaviour of the photoconductivity is similar to that of the dark conductivity in the same temperature regime. The conductivity measurements reveal that the material becomes more localized at low temperatures, and the observed activation energy for this process is similar to the one found via photoconductivity measurements. The behaviour of the photoconductivity on the low-temperature side of the peak has thus been attributed to a thermally-activated mobility. Light intensity measurements at low temperatures have shown the presence of monomolecular processes (in the low–light-intensity limit) which change over to bimolecular processes in the high–light-intensity limit. For the light intensities being used in most of the work in this thesis,

monomolecular processes are dominant, implying that the photo-generated carrier density is less than that of the thermal dark carriers. At high temperatures, the photoconductivity decreases as a result of recombination of photo-carriers with thermal dark carriers (monomolecular process). The decay times in carbon aerogels are very long at low temperatures (on the order of 20 seconds), suggesting the existence of traps in these systems. With increases in mass density and heat-treatment temperature (i.e., decreases in disorder), a reduction in the photoconductivity is achieved. This effect has been attributed to a reduction in the number of trap states that exist in the system.

Chapter 5 presents the conclusions of this work. There it is shown that control of the aerogel structure on a nanoscale is very important in determining the resultant macroscopic properties of these materials. All properties, from the fractal nature of the pores to the electrical transport and optical properties of the solid matrix can be affected on this level. The many physical parameters that can be varied, such as density and particle size can ultimately result in systems that have varied morphologies. Although there are two chemically defined RF-based carbon aerogels (colloidal and polymeric), they have been found to be similar in their transport properties.

Chapter 2

Aerogel Synthesis and Characterization

In order to understand the upcoming discussion on the transport properties of carbon aerogels, it is instructive to first have a handle on the structure of these materials. As described in Chapter 1, the carbon aerogel has a complicated structure of pores and clusters of particles, and to get a better understanding of any observed transport features, it is necessary to correlate experimental observations with this physical structure. This chapter investigates the structural properties of the carbon aerogels studied. First the chemical synthesis of carbon aerogels is examined. It is observed that variations in chemical synthesis and external parameters such as heat-treatment temperature, result in microstructural changes in the carbon aerogel system. Next, characterization techniques such as Raman spectroscopy and transmission electron microscopy are used to examine and understand the porous network and solid matrix of carbon aerogels.

2.1 Synthesis

2.1.1 Resorcinol-formaldehyde-based Carbon Aerogels

I have been fortunate to visit the Lawrence Livermore National Laboratory (LLNL) to obtain hands-on experience with part of the synthesis process of resorcinol-formaldehyde (RF) aerogels, the precursors to the carbon aerogels studied here. RF aerogels are derived from a process of chemically-induced phase separation (sol-gel processing) [9]. This involves the mixing of resorcinol (1,3 dihydroxy benzene) and formaldehyde at a 1:2 molar ratio. Sodium carbonate is added as a base catalyst (C), and distilled water acts as a diluent. The mixture is sealed in glass vials and is allowed to crosslink in an oven at 50-95°C for about three days. The crosslinking reaction takes place as follows [5, 10]. The sodium carbonate helps to activate the highly electrophilic 2, 4 and/or 6 ring positions of resorcinol. Hydroxymethyl derivatives of resorcinol are formed as is shown in Fig. 2-1. These further condense into polymer "clusters" (see Fig. 2-2) that crosslink to form a dark-red gel.

In order to dry the gel for further processing/application, the water trapped within the pores has to be removed. However, as the pores are easily collapsible under capillary forces, driving water out by heating can result in pore collapse. The process for liquid removal is thus a two-step procedure for RF-based aerogels. The first step involves placing the gels in an agitated acetone bath at room temperature. After multiple exchanges with fresh acetone, all the water is removed from the pores of the gel. By placing the RF aerogels into a jacketed Polaron ® vessel, a second solvent exchange can occur, whereby acetone is replaced by carbon dioxide (CO_2). The jacket is initially cooled to 10°C and liquid CO_2 is placed into the vessel. After purging to ensure that all the acetone is removed, the pressure and temperature of the vessel are raised to above the critical point of CO_2 (T_c = 31°C, P_c = 7.4 MPa). The carbon dioxide can then be removed without pore collapse. Monolithic samples can be produced in this fashion.

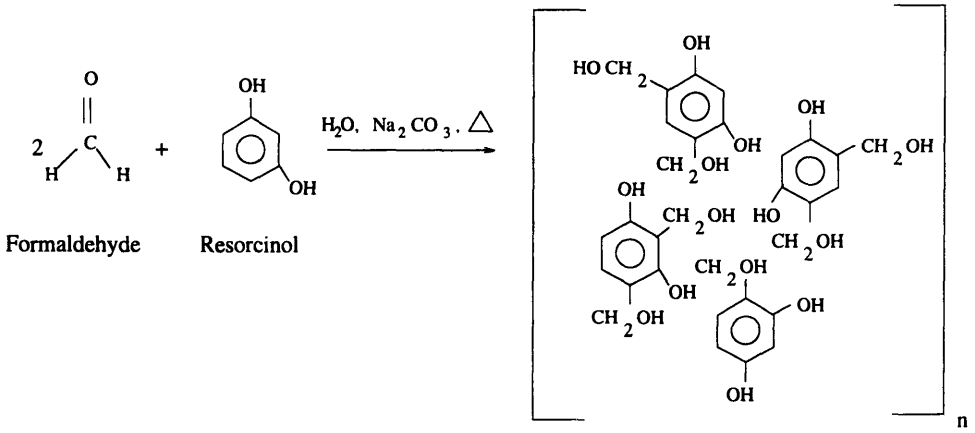

Figure 2-1: Synthesis reaction for crosslinking of resorcinol with formaldehyde to make RF aerogels. Distilled water and the catalyst Na_2CO_3 are added to the RF mixture. The triangle represents external heating that is supplied during the cross-linking process. The figure on the right hand side shows the hydroxymethyl substitution that occurs during the sol-gel process. The n shows that this structure has a higher molecular mass than shown.

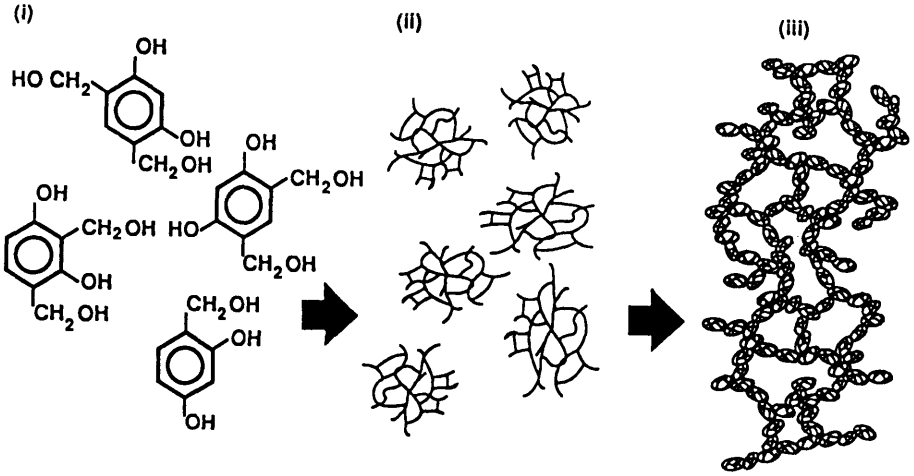

Figure 2-2: (i) After the hydroxymethyl substitution occurs, (ii) RF clusters form, (iii) which further develop into the particle structures inherent to the carbon aerogel system.

High resolution transmission electron microscopy (TEM) studies show [11] that the RF aerogels obtained, as described above, are highly porous, with nanometer-sized particles (grains)[1]. The resultant RF aerogels are pyrolyzed at 1050°C in a tube furnace under nitrogen flow for 4 hours, resulting in as-prepared carbon aerogels. This carbonization process is a violent reaction which results in the release of volatile by-products. The individual particles form additional pores and decrease in size, giving rise to microscopic disorder (as discussed below). Despite the volume shrinkage associated with pyrolysis in going from RF aerogels to carbon aerogels, aspects of the porous nanostructure remain fairly unchanged between the two aerogel types. Subsequent heat-treatment to higher temperatures (up to 1800°C in this work) results in heat-treated carbon aerogels.

By changing the resorcinol to catalyst (R/C) molar ratio, the rate at which formaldehyde consumption occurs during synthesis varies. This has an effect (on a microscopic scale) on the particle size, mass density (ρ_m), specific surface area (SSA) and interconnectivity of the carbon aerogel. In this work, a variety of carbon aerogels have been studied, with mass densities, ρ_m, ranging from 0.1 g/cm^3 to 0.8 g/cm^3, particle sizes from 70 Å to 150 Å, and SSAs [2] of 500 m^2/g to 850 m^2/g. These variations during RF synthesis result in two types of carbon aerogels; *polymeric* and *colloidal*. An in-depth description of the structural differences between these two types of RF-based aerogels is given below.

Figures 2-3(a)-(b) show the high-resolution TEM micrographs of the two types of RF-based carbon aerogels. Generally, both classes of aerogels consist of grains with nanopores (< 2 nm) between connected grains as well as inside the grains. In addition, mesopores (2 - 50 nm) are formed between chains of interconnected grains. The grains themselves consist of a network of carbon ribbons (or graphene sheets). The grain connectivity and the RF network vary for the two aerogel types. By increasing the

[1] The words *particles* and *grains* will be used interchangeably in this work.

[2] To appreciate these numbers, remember, a basketball court occupies 437m^2!

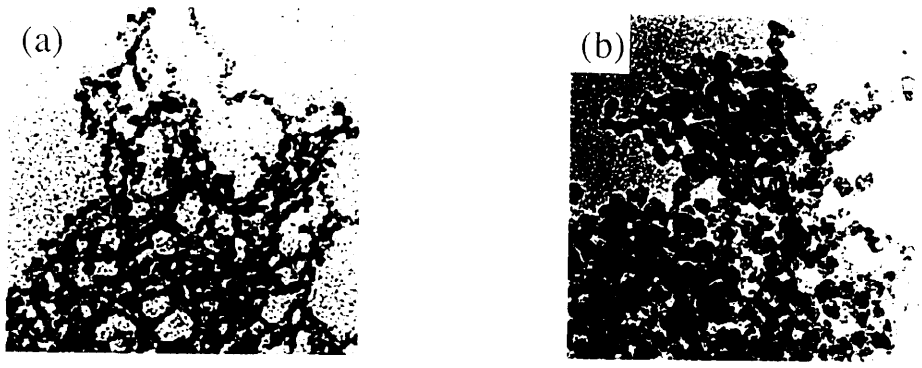

Figure 2-3: High resolution TEM micrographs showing the differences between (a) *polymeric* (R/C=50) and (b) *colloidal* (R/C=300) RF-based carbon aerogels.

packing ratio of the grains, the mass density of the carbon aerogel can be increased. The granularity associated with the packing of the grains leads to what we will define as mesoscopic disorder in the system (see below).

Polymeric carbon aerogels (high catalyst ratio, R/C=50) have few detectable spherical grains and hence, are morphologically different. For such aerogels, the spherical feature is smeared out as the cross-section of the connection between the grains is now on the order of the grain diameter (see Fig. 2-3(a)). These highly interconnected grains form a filamentous structure with characteristic diameters of 70-90 Å. The presence of the filaments in this aerogel results in a more intricate morphology and hence a larger specific surface area ($\sim$ 800 m^2/g). The larger specific area in polymeric carbon aerogels can also be understood from a synthesis point of view. A large catalyst concentration results in the rapid formation of RF chains which proceed to crosslink with each other, thus shortening the cluster formation lifetime and resulting in smaller particles.

For colloidal aerogels (low catalyst ratio, R/C=300), the grains are distinct and spherical in shape, with a fairly broad distribution (average diameter $\sim$ 150 Å), and a

specific surface area of ~ 550 m^2/g. The cross-section of the neck connection between the grains (see Fig. 2-3(b)) has a size much less than the grain radius. This loose connection between the grains is exhibited in the weak mechanical properties of this aerogel. Another type of colloidal aerogel (R/C=200) can be made, with features similar to its R/C=300 counterpart, except that now, the grain size is more uniform within individual samples (average diameter $\sim$ 120 Å), and the specific surface area is ~ 650 m^2/g.

For the later discussion of the characterization of disorder, we classify disorder by its spatial extent. The disorder associated with granularity is termed *mesoscopic* disorder. Hence, the R/C=50 carbon aerogel is more mesoscopically disordered than the R/C=300 aerogel because the former material has a smaller grain size. Structural defects contained within a grain, such as dangling bonds and other topological disorder, are collectively known as *microscopic* disorder. This type of disorder can arise during carbonization, as discussed above.

2.1.2 Phenolic-furfural-based Carbon Aerogels

The synthesis of these newer aerogels follows a path similar to that of the RF-based aerogels described above. However, as the synthesis can be conducted in alcohol, the solvent exchange step prior to supercritical drying from carbon dioxide can be eliminated. Figure 2-4 shows the chemical pathway for the synthesis of these newer aerogels. The synthesis is described in detail elsewhere [12]. Generally, a polymer solution such as FurCarb UP520 [3] is diluted with 1-propanol, and a mixture of aromatic acid chlorides (Q2001) is added [4]. The solution is sealed and allowed to cross-link by curing at 85°C for 7 days. The resultant highly crosslinked PF aerogels are dark brown in colour and can be converted, upon pyrolysis in an inert nitrogen atmosphere, into PF-based carbon aerogels. The carbonized derivatives of these new aerogels have sur-

[3] FurCarb consists of a 50:50 mixture of phenolic novolak dissolved in furfural.

[4] FurCarb UP520 and Q2001 are both obtained from QO Chemicals, Inc., West Lafayette, IN.

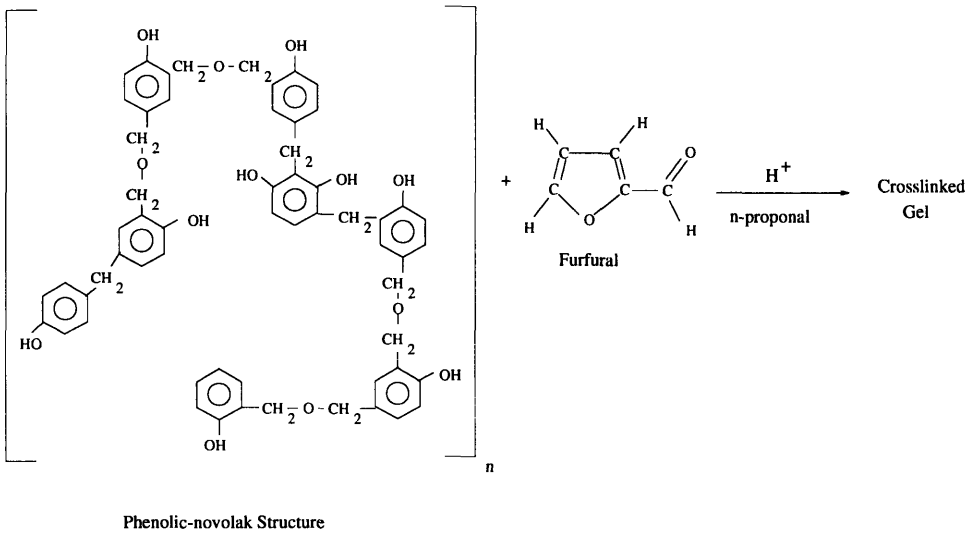

Figure 2-4: Synthesis reaction for PF aerogels. Crosslinking occurs between aromatic rings through the aldehyde group on furfural. The reaction takes place under acid catalyzed conditions (as denoted by H^+).

face areas on the order of 550 m^2/gm and consist of interconnected irregularly-shaped platelets of $\sim$ 100 Å in size, as revealed by TEM studies [12].

2.2 Applications

Before the organic RF aerogel was made, silica aerogels were the more common type of aerogel on the commercial market. They still are, due to their cheaper synthesis costs. At any rate, the carbon aerogel with its superior physical qualities (e.g., lower thermal conductivity) is coming into its own, as more economic approaches to synthesis are made available [13, 14].

Aerogels are used as thermal insulators in glass because of their low thermal conductivity. They have been used to capture cosmic dust, intact [15]. Researchers have taken advantage of their porous nature to create aerogels capable of absorbing volatile organic compounds such as nitric oxide and carbon monoxide. They are also being used as components in double layer capacitors [1, 16], here advantage is being

made of their large specific surface areas. On a larger scale, aerogels are being used at LLNL in a prototype water filtering system for use in California [3]. The aerogel, and in particular the carbon aerogel, is making an impact in the technological arena as time goes by.

2.3 Characterization Techniques

Many experiments have been done in order to obtain physical numbers for the various properties of the RF aerogel and its carbon derivative. Table 2.1 lists a few properties of carbon aerogels (PF- and RF-based), and compares them with graphite. The carbon aerogel densities quoted are typical of the values studied in this work; lower densities are achievable. The physical parameters of carbon aerogels are seen to be different from graphite. The carbon aerogels, for example, have lower mass densities and thermal conductivities than graphite. These numerical differences result from the structural differences between graphite and carbon aerogels. We now look at a few experiments that have been done to further understand the structure of aerogels and how this structure relates to observed physical properties.

2.3.1 Gas Adsorption

Gas adsorption experiments are one way in which the pore sizes in a porous material can be measured. Porous materials can be classified with a variety of pore sizes ranging from nanopores with average widths less than 20 Å , macropores with widths larger than 500 Å , and mesopores with widths between 20 Å and 500 Å. Adsorption[5] occurs when a gas (the adsorbate) condenses on the surface of the material (the adsorbent) whose surface area is being measured. By placing the adsorbent into a closed container of adsorbant gas at a fixed pressure, as the material adsorbs the gas, the pressure of the gas decreases. For a porous material, as the adsorption occurs, the

[5] As opposed to absorption which occurs when a gas penetrates the absorbing material.

	CRF	CPF	Graphite
ρ_m (g/cm^3)	0.1–0.8	0.4–0.7	2.26
Thermal Conductivity (RT) (W/m-K)	0.012[a]	0.015–0.017	3000[b]/6[c]
SSA (m^2/g)[d]	470-550	370-400	–
Particle sizes (Å)	70-160	100	–

Table 2.1: Showing some physical parameters for aerogels and graphite. CRF refers to the resorcinol-formaldehyde-based carbon aerogel, while CPF refers to the phenolic-furfural-based carbon aerogel. Comparisons of densities, thermal conductivities specific surface areas and particle sizes are given.
[a] Lowest value obtained with $\rho_m = 0.16$ g/cm^3 [17]
[b] In-plane
[c] Out-of-plane
[d] See [12]

rate at which the pressure decrease occurs depends on the pore sizes. A plot of the amount of gas adsorbed versus the relative pressure, for example, gives an adsorption isotherm. By applying the Brunauer, Emmett and Teller (BET) equation [18] to this isotherm, estimates of the specific surface area (SSA) can be made. Adsorption isotherms are also useful in determining the pore size distribution in a system. There are a few drawbacks to the adsorption technique, one being the inaccessibility of the gas to closed pores or extremely small nanopores. Table 2.2 shows the results of BET studies done on carbon aerogels [5]. As the R/C molar ratio is decreased, the specific surface area increases. This increase in surface area with decreasing particle size is partly attributed to the faster formation of particles that occurs at high catalyst concentrations. A high catalyst concentration causes the electrophilic resorcinol to react very quickly with formaldehyde. This in turn results in clusters that are ill-formed and do not have time to branch out and react to form other clusters. Consider the analogy of crystal growth. The slower the growth process, the more ordered and larger the generated crystals. If the crystal growth is stifled by quenching the temperature of the system, then smaller crystallites will form and the

R/C[a]	50	100	150	200	300
BET surface area (m^2/gm)	818	762	712	682	588

Table 2.2: Specific surface areas (SSA) for (RF) carbon aerogels as a function of R/C molar ratio, as obtained by BET analysis. Increases in R/C (corresponding to increases in particle sizes) result in a reduction of the SSA.

overall structure will be more polycrystalline.

2.3.2 Small Angle X-ray Scattering (SAXS)

SAXS experiments tend to have an advantage over gas adsorption, in that it is a less intrusive and less destructive technique. Generally X-rays are used to irradiate the sample. The resulting scattered intensity depends on the size and concentration of scattering centers as well as on the scattering vector **q**. The scattering vector is in turn a function of the scattering angle θ via:

$$\mathbf{q} = (4\pi/\lambda)sin(\theta/2) \tag{2.1}$$

Each length scale, L, in the sample has a corresponding scattering vector, with larger length scales corresponding to smaller wavevectors ($q = 2\pi/L$). As the dimensions in the aerogel are on the order of 1-100 nm, and X-rays have wavelengths on the order of 0.1-0.2 nm, the scattering angles are very small, on the order of 0.01-10°, hence the nomenclature, small-angle X-ray scattering. SAXS studies reveal [6] structural features with differing length scales ranging from a continuum to individual particle sizes. The SAXS studies have also been used to determine the fractal [6] nature of the particles in these materials. By finding the fractal dimension, the method by which aggregation occurs in these materials can be examined. SAXS studies carried out on

[a]Note that R/C will always refer to the Resorcinol/Catalyst molar ratio, where the catalyst is sodium carbonate (Na_2CO_3).

[6]Fractals deal with the self-similarity of objects. For more information, see [19].

the silica aerogels show that these materials are fractal over many decades of 1/q [7]. For the carbon aerogels, SAXS measurements are less convincing in showing that the particles are fractal. Evidence shall be given below to show that, although the particles are not fractal, the porous structure does tend to be fractal. The scattering experiments are also found to be generally more sensitive to the surface area as contributed by open and closed pores, unlike with gas adsorption.

2.3.3 Transmission Electron Microscopy

Transmission electron microscopy (TEM) studies have been previously carried out on RF aerogels and their pyrolyzed versions. However, emphasis was given to studying the structure within the carbon particles. These studies show that the carbon aerogel retains the pore features of its RF counterpart fairly well. The results of these studies for the polymeric and colloidal carbon aerogels have been described in Section 2.1.

Current TEM studies[7] on RF-based carbon aerogels with various densities and particle sizes (see Table 2.3) have in this thesis focused on the larger mesopores found between the interconnected particles. By definition, mesopores are considered to be between 20 to 500 Å in size. By studying the makeup of these larger pores, and the effect of density and other parameters on their size and shape, we hope to understand how the mesopores can be engineered for application purposes, such as molecular filters.

For the experiment, samples were pulverized in a crucible and placed on a holey amorphous carbon grid (microgrid). TEM micrographs were taken with a 400kV accelerating voltage and a magnification of 10^5. The samples were thin enough to allow electron beam transmission and result in a clear image. The TEM micrographs span a size of 250 Å × 250 Å, thus allowing for the sampling of large regions of carbon aerogel material. Figures. 2-5(a)-(d) show the TEM micrographs of low and high density polymeric and colloidal carbon aerogels. The characteristic particle sizes

[7]Graciously carried out by Prof. M. Endo and co-workers at Shinshu University, Japan.

Table 2.3: TEM Parameters for as-prepared (RF) Carbon Aerogels

R/C	50	50	200	200
Density(g/cm^3)	0.187	0.662	0.134	0.586
Particle Size (Å)	70–90	70–90	120	120

are on the order of ~80 Å and ~120 Å for the polymeric and colloidal carbon aerogels, respectively, independent of density. These results agree with TEM measurements by Pekala *et al.* on RF carbon aerogels [11] and their carbonized derivatives [5]. The high-density samples exhibit a more dense structure than the low-density samples. The arrows in Fig. 2-5 indicate the presence of mesopores which have dimensions on the order of 70 - 200 Å.

Once the TEM micrographs are taken, the images are scanned into a computer. This is the first step in being able to do quantitative analyses on the mesopore structure. The digitized images so obtained show white and dark areas which correspond to mesopores and particles, respectively (see Figs. 2-6(a)-(d)). There are two ways to visualize the pores once the TEM micrographs are digitized.

The first method involves carrying out a 2-dimensional fast Fourier transform (FFT) of the original TEM images. This frequency analysis approach to studying the TEM images provides an efficient means of analyzing highly disordered materials such as carbon aerogels. The results of this method are shown in the FFT power spectra of Figs. 2-7(a)-(d). The power spectra indicate the spatial frequency distribution of the lattice image, and highlight preferred spatial separations. The central area corresponds to low frequency, and the central point in particular indicates the brightness of the picture. The variations in brightness tell the amount of contribution of each $\mathbf{k}$ point. The frequencies obtained from the Fourier analysis become higher as the location moves further from the center. The power spectra in each figure looks concentric, suggestive of an isotropic cross-section and a random orientation of the pore structures observed in the TEM micrographs. These observations suggest that

the microstructure of the carbon aerogels is almost isotropic on large length scales, and has no long-range preferred spatial orientation.

In order to analyze the pore structure in more detail, the power spectrum images of Fig. 2-7 were represented by graphs obtained by integration around the central points of the images. The various **k**-values associated with each power spectrum (and thus the corresponding real-space dimension) can be plotted versus the intensity with which these **k**-values occur. This analysis is done for each sample, the results of which are plotted in Fig. 2-8. The graph exhibits many frequency components, but the spatial graphs are qualitatively different from each other. Since the x-axis denotes spatial wavelength, and the y- axis denotes intensity of the power spectrum, these graphs show the pore distribution. The location of a peak along the x-axis corresponds to the most probable pore size in a certain size range, and the height of the peak is sensitive to both the pore density and the brightness of the pore images. The high-density samples exhibit a larger distribution of smaller mesopores (from $\sim 100 - 200$ Å) while the low-density samples exhibit a greater distribution of larger-sized mesopores ($\sim 150 - 250$ Å). This implies that the structure of the low-density aerogels tend to form with more open spaces between particles than in the high-density case. A closely-packed particle structure, as would be found in the high-density case, will result in a smaller distribution of large mesopore sizes. The mesopore-size distribution will tend towards smaller sizes. These results correlate with Raman and conductivity measurements [20] that show that increases in mass density result in a closer packing of particles and therefore a higher probability of smaller mesopores distributed throughout.

The second analysis approach involves transforming the original TEM images into binary images. This is done to facilitate the observation of the pore shapes. Since the average brightness of the original image is different in places, it is difficult to transform the original image with the same threshold level. Therefore, a low frequency cut-off filter operation was used along with a FFT, followed by a masking operation, and

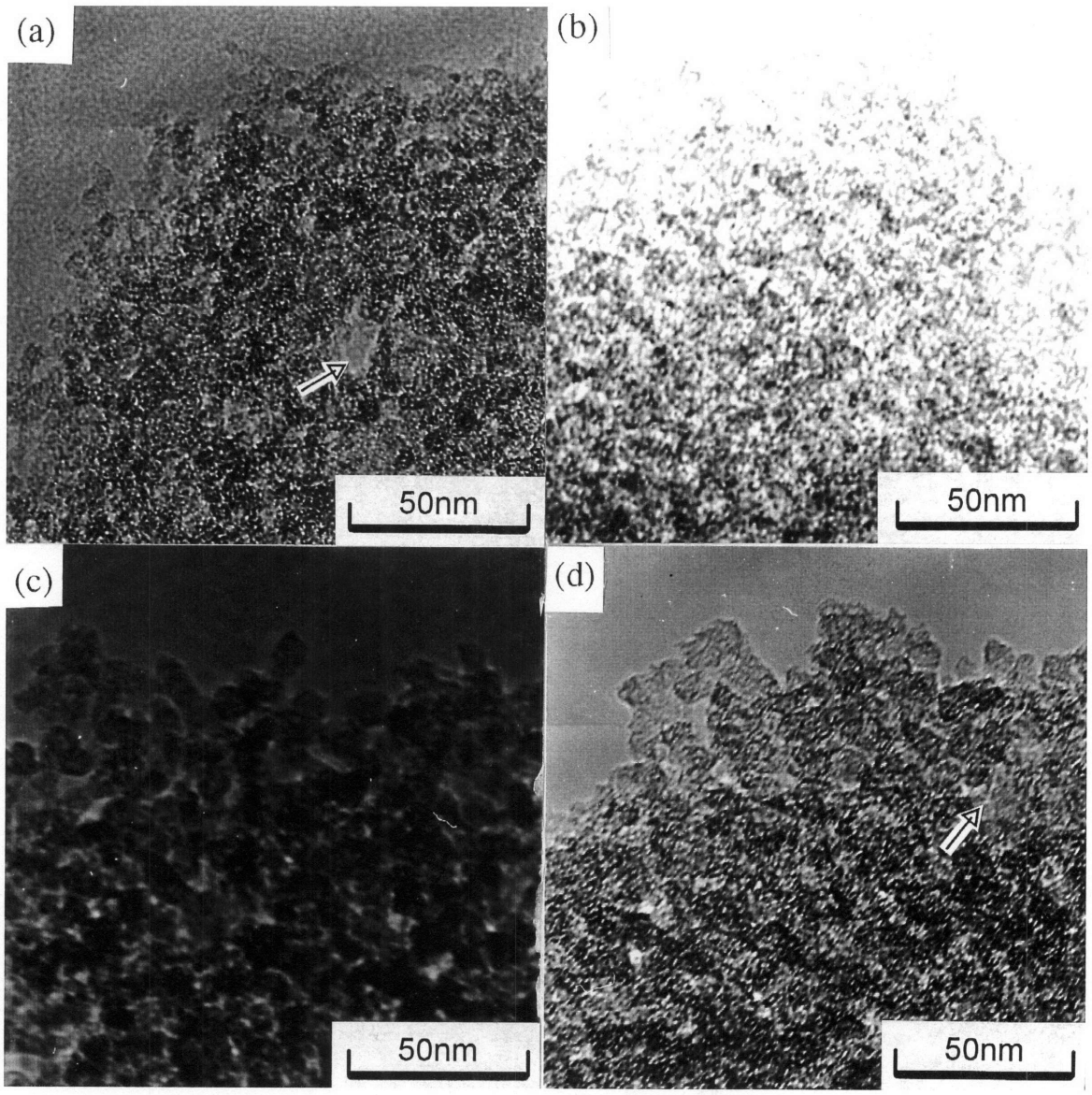

Figure 2-5: TEM micrographs (magnification X 10^5) of the polymeric and colloidal carbon aerogels studied. Labeling clockwise from the upper left- hand corner, R/C=50: (a) $\rho_m = 0.187$ g/cm^3, (b) $\rho_m = 0.662$ g/cm^3 and R/C=200: (c) $\rho_m = 0.134$ g/cm^3, (d) $\rho_m = 0.586$ g/cm^3. Arrows indicate mesopores in the system.

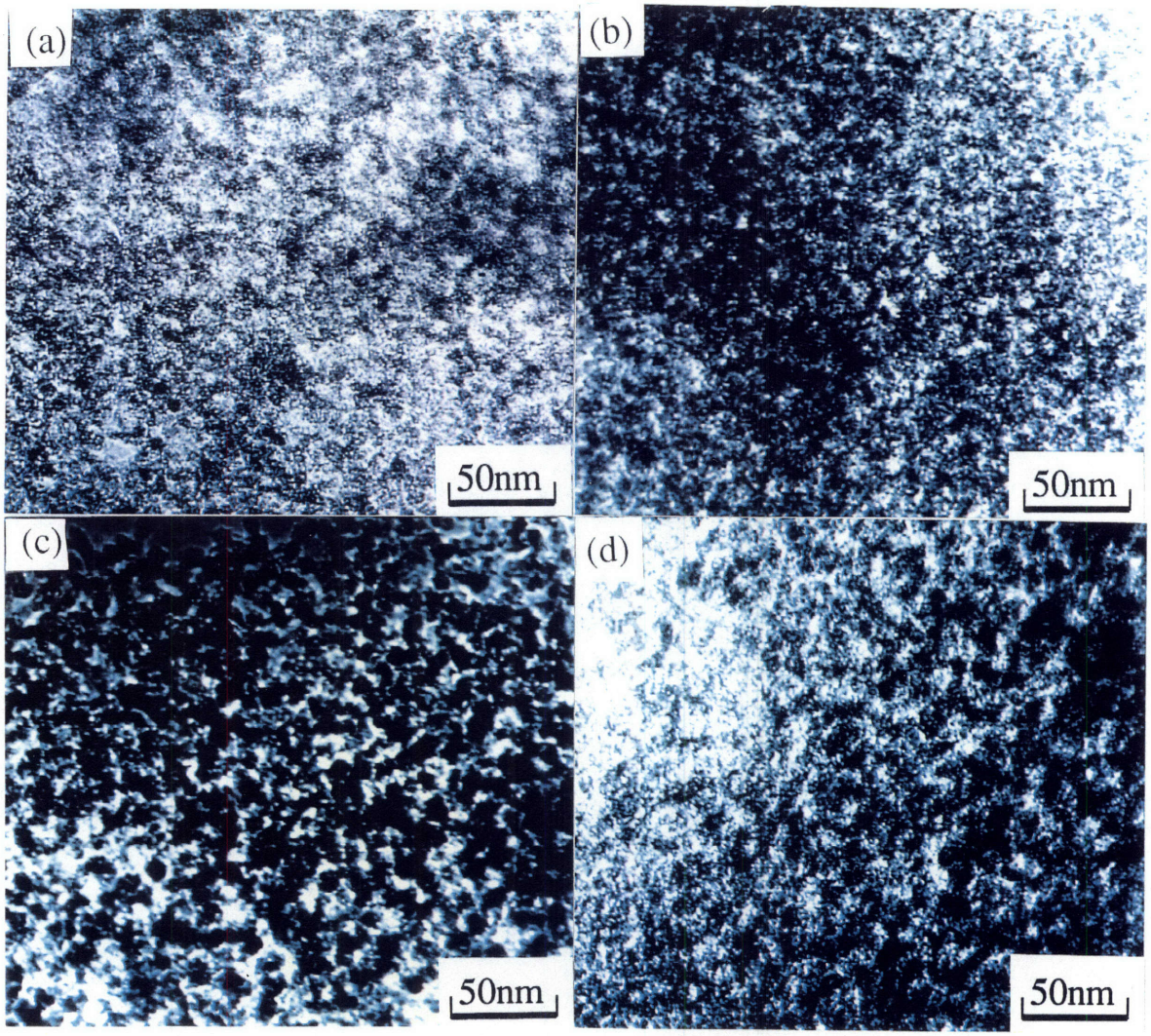

Figure 2-6: Digitized images of the original TEM micrographs from Fig. 2-5 showing the mesopores and particles. Labeling clockwise from the upper left-hand corner, (a) R/C=50; ρ_m = 0.187 g/cm^3 (b) R/C=50; ρ_m = 0.662 g/cm^3 (c) R/C=200; ρ_m = 0.134 g/cm^3 (d) R/C=200; ρ_m = 0.586 g/cm^3.

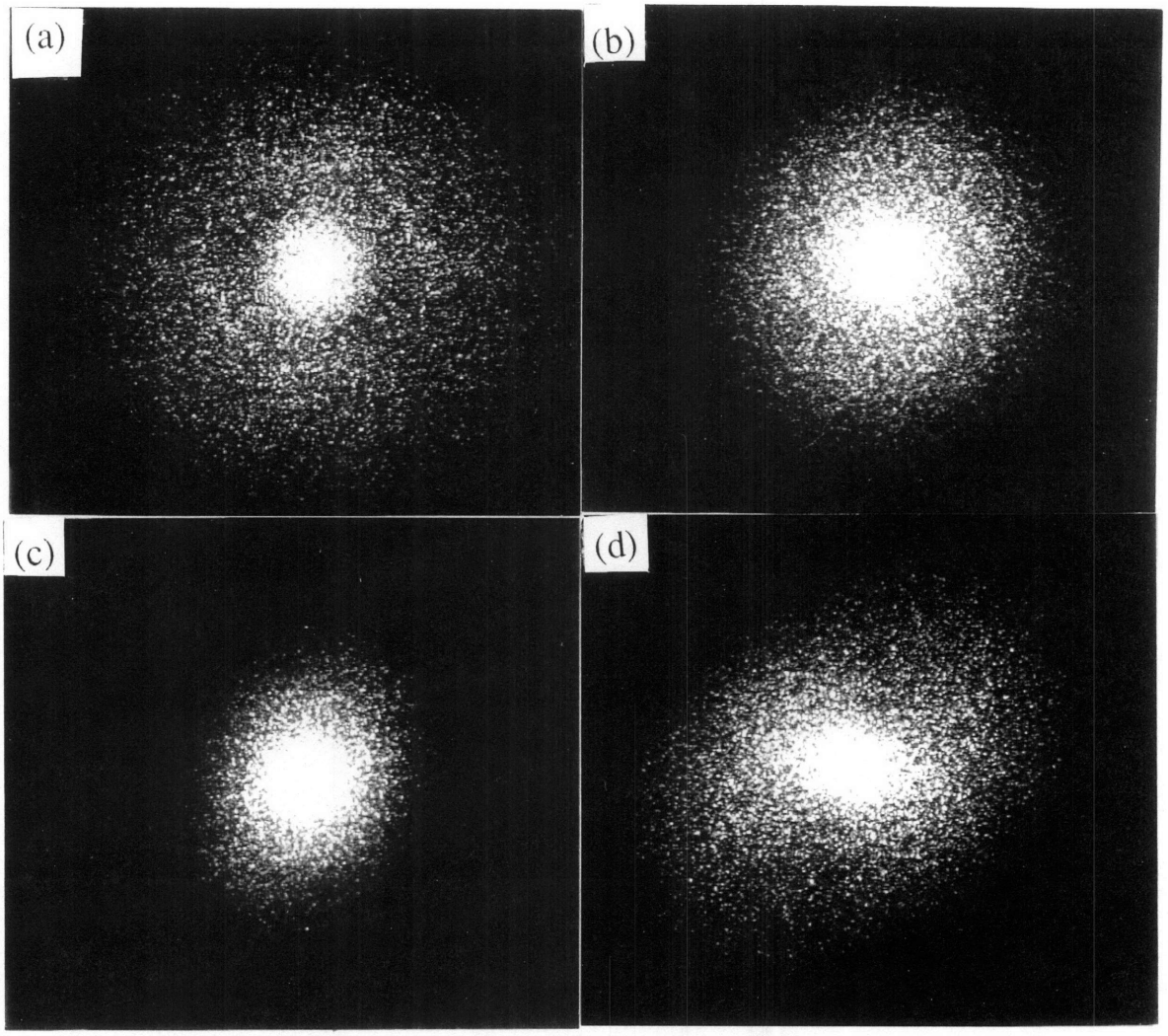

Figure 2-7: Power spectra of carbon aerogels studied as obtained from a FFT of the original TEM micrographs in Fig. 2-5. Labeling clockwise from the upper left-hand corner, (a) R/C=50; $\rho_m = 0.187$ g/cm^3 (b) R/C=50; $\rho_m = 0.662$ g/cm^3 (c) R/C=200; $\rho_m = 0.134$ g/cm^3 (d) R/C=200; $\rho_m = 0.586$ g/cm^3.

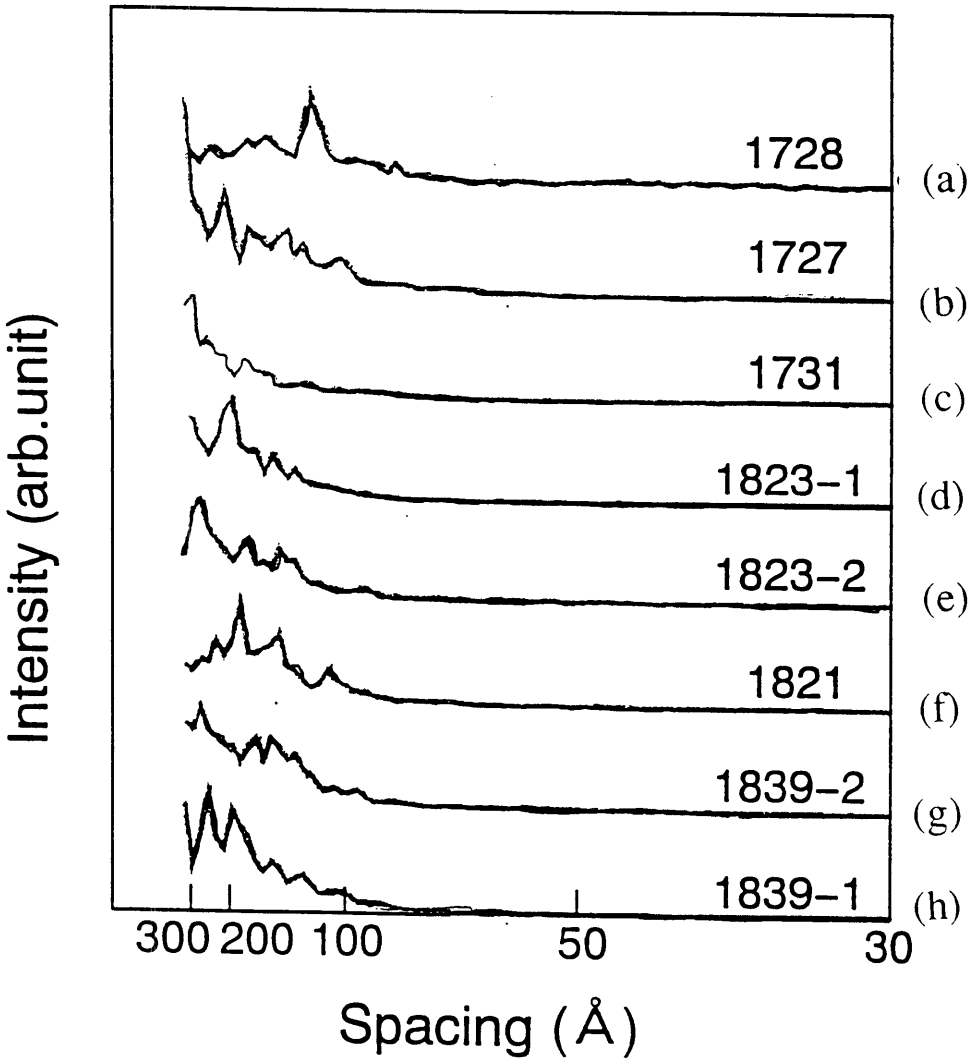

Figure 2-8: Power spectrum intensity versus spatial wavelength shows the pore distribution for all the samples studied. The spectra labeled (b)-(d) and (g) have corresponding TEM micrographs in Fig. 2-5. A 1 or 2 after a 4-digit number refers to the first and second runs performed on a separate piece of the same parent sample. Unless otherwise noted, the heat-treatment temperature is 1050° C. R/C=50: (a) (1728) ρ_m = 0.66 g/cm^3, T_{HT} = 1800° C (b) (1727) ρ_m = 0.662 g/cm^3 (c) (1731) ρ_m = 0.187 g/cm^3; R/C=200: (d) (1823-1) ρ_m = 0.586 g/cm^3 (e) (1823-2) ρ_m = 0.586 g/cm^3 (f) (1821) ρ_m = 0.401 g/cm^3 (g) (1839-2) ρ_m = 0.134 g/cm^3 (h) (1839-1) ρ_m = 0.134 g/cm^3.

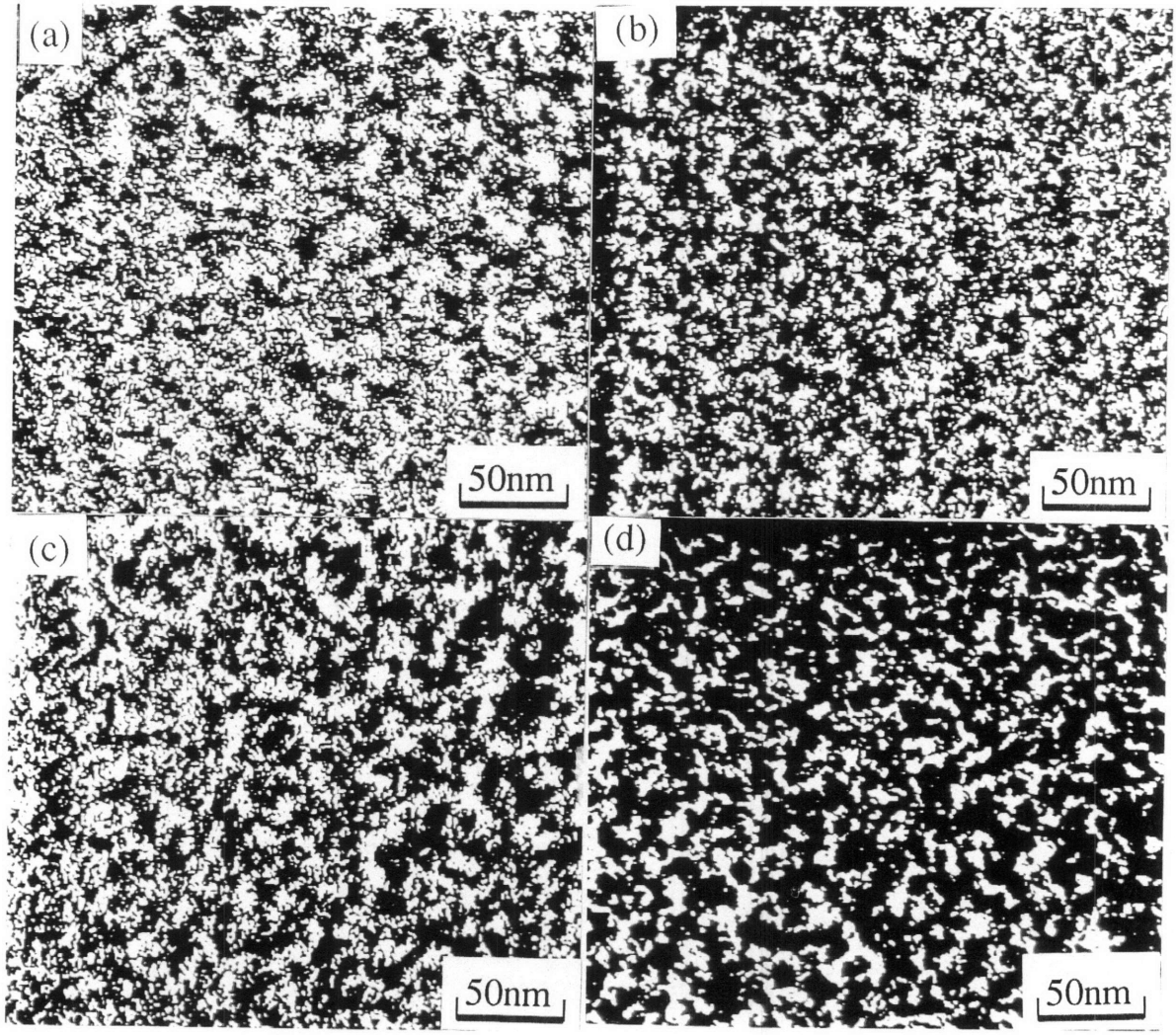

Figure 2-9: Binary images of original TEM micrographs, showing the pore shapes in real space. Labeling clockwise from the upper left-hand corner, R/C=50: (a) $\rho_m = 0.662$ g/cm^3 (b) $\rho_m = 0.187$ g/cm^3; R/C=200: (c) $\rho_m = 0.586$ g/cm^3 (d) $\rho_m = 0.134$ g/cm^3.

an inverse fast Fourier transform (IFFT) step to make the brightness uniform before the binary transformation. The mask is a ring-shaped pattern with radii from 2 to 3 pixels, corresponding to 131 Å to 87.5 Å in spatial wavelengths. In each pattern, the central points were preserved in order to maintain the brightness of the real space images. The image was then transformed linearly to a full brightness scale from 0 to 255. To form a binary image, any signal brighter than 128 was set at 255, and any signal with a brightness less than or equal to 128 was set to 0. The results give binary images (as obtained from Fig. 2-5) which show clearly the pore shapes in real space (see Figs. 2-9). There are many pore sizes, and each pore has a ragged outline, indicating the intricacy of the pore shapes.

As the quantity of gas adsorption is determined by the pore surface area, it is instructive to obtain the fractal connected with the pore surface. The pore surface of the samples are three-dimensional, whereas the TEM images of the pores is a projection of the 3-D pore onto a 2-D surface. Since the aerogel structure has no preferred orientation, the surface area in 3-D is related to the outline of the TEM image. The fractal dimension, D, can be calculated as discussed below.

Before the quantitative analysis began, islands which made contact with any of the edges of the picture frames, and islands smaller than 50 pixels in area were removed from the binary image. The area S and the length of the profile X of the remaining islands were measured. Figure 2-10 plots the perimeter X as a function of the area S for the remaining islands. The resulting pore structure is found to be fractal since S correlates with X, though there is some dispersion in the data. This same correlation holds between the number of pixels defining the surface area of the pores (S_{n}) and the number of pixels defining the perimeter of the binary image (X_{n}) i.e.,

$$S_{\mathrm{n}}^{1/2} = X_{\mathrm{n}}^{1/D} \tag{2.2}$$

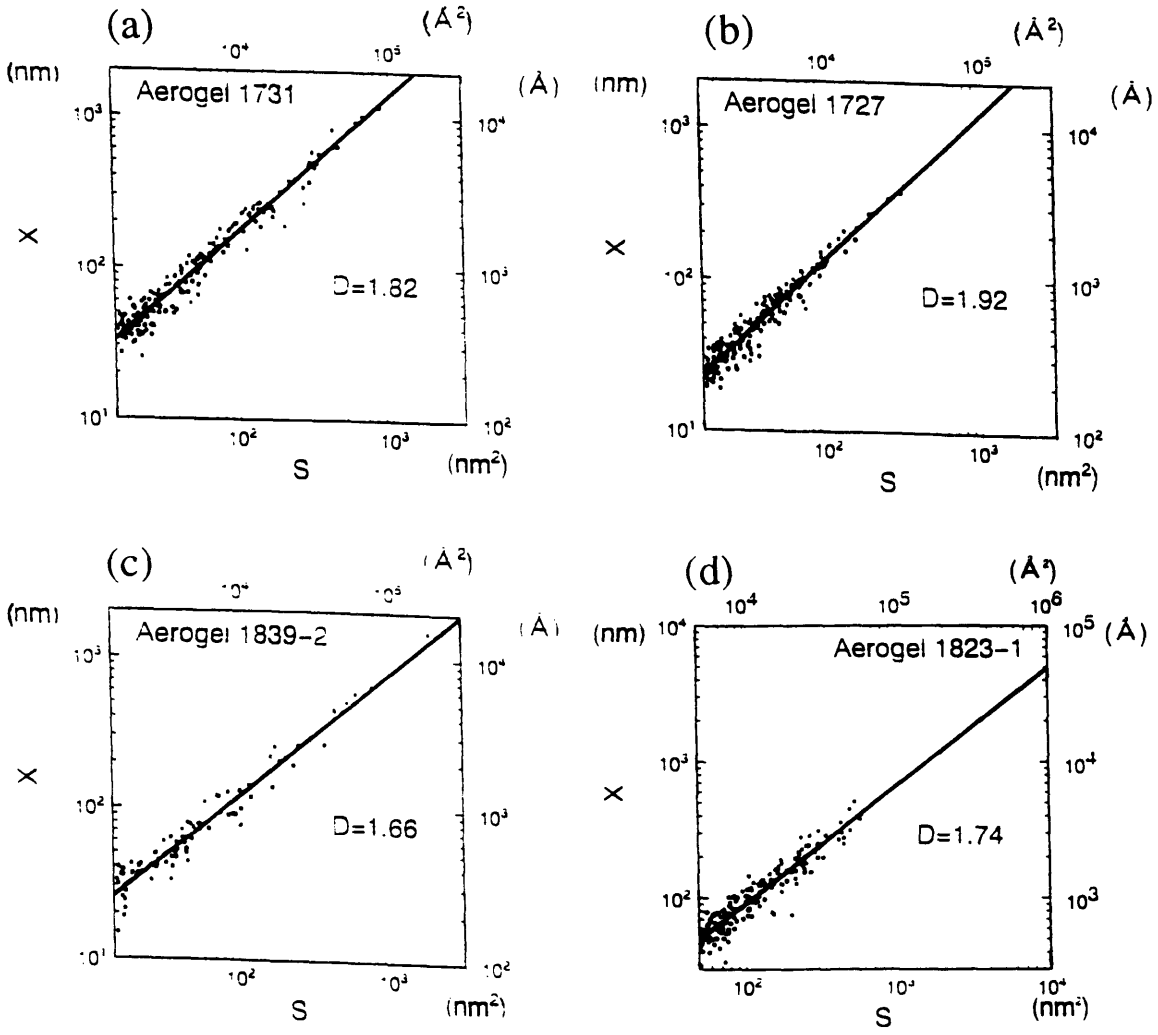

Figure 2-10: Length of outline (perimeter, X) versus square measure (area, S) of the binary image of the mesopores. The numbers with a -1 or -2 after them show the first or second experimental run carried out on a different piece of the same parent sample. (a) R/C=50; (1731) $\rho_m = 0.187 \text{g/cm}^3$ (b) R/C=50; (1727) $\rho_m = 0.662 \text{ g/cm}^3$ (c) R/C=200; (1839-2) $\rho_m = 0.134 \text{ g/cm}^3$ (d) R/C=200; (1823-1) $\rho_m = 0.586 \text{ g/cm}^3$.

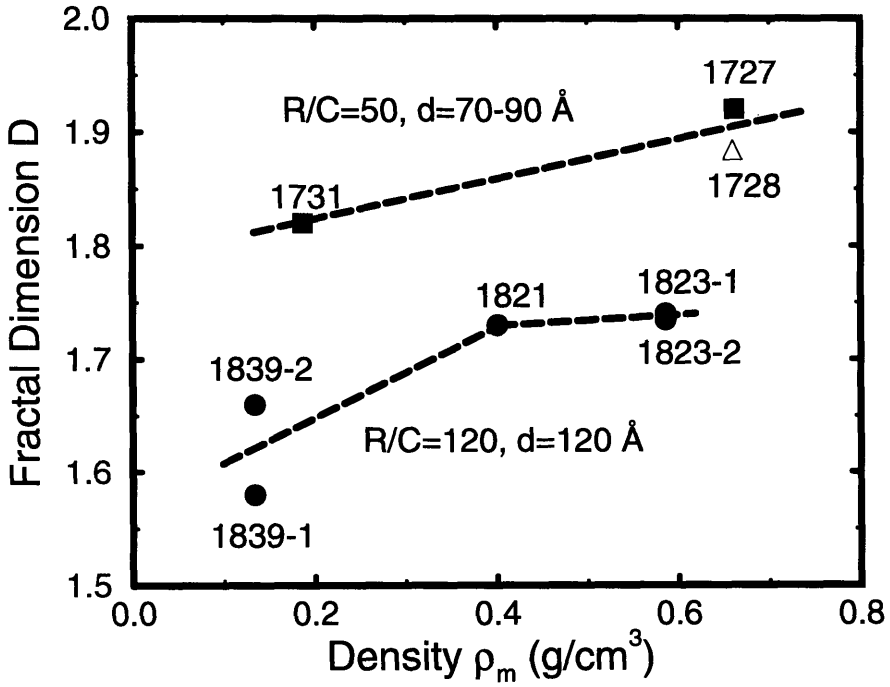

Figure 2-11: Fractal dimension, D, as a function of sample density for the mesopores (2 - 50 nm) in the carbon aerogels studied. The R/C molar ratios and corresponding particle sizes are shown. Dashed lines are drawn as guides to the eye. The magnification factor is 10^5. □, △ R/C=50: (1727) ρ_m = 0.662 g/cm^3; (1728) ρ_m = 0.662 g/cm^3, T_{HT} = 1800° C; (1731) ρ_m = 0.187 g/cm^3; • R/C=200: (1823-1)/(1823-2) ρ_m = 0.586 g/cm^3; (1821) ρ_m = 0.401 g/cm^3; (1839-1)/(1839-2) ρ_m = 0.134 g/cm^3.

where D is the fractal dimension, given by:

$$D = 2(\Delta \log X_{\rm n})/(\Delta \log S_{\rm n}) \ . \tag{2.3}$$

Using Eqn. (2.3) the binary images are analyzed to obtain the fractal dimensions, D, for carbon aerogels of various densities and particle sizes. The results shown in Fig. 2-10 indicate that the polymeric carbon aerogels (R/C=50) have a larger fractal dimension than the colloidal carbon aerogels (see below).

Figure 2-11 shows the fractal dimension, D, as a function of mass density, ρ_m for all the samples studied. For the colloidal samples (R/C=200) labeled 1839-1, 1839-2, 1823-1 and 1823-2, the experiments were carried out twice on a different piece of the same parent sample. The mesopores in polymeric carbon aerogels exhibit larger D values than those in colloidal carbon aerogels. For polymeric carbon aerogels, because of their smaller particle sizes, the outline of mesopores, as formed by these particles, will appear more regular in shape, and hence the larger fractal value. Figure 2-11 also shows that the fractal dimension for the mesopores is influenced by the mass density, with an increase in density resulting in an increase in D. With decreasing mass density, the results for the fractal dimension become slightly uncorrelated for the two runs of the sample with $\rho_m = 0.134$ g/cm^3 (labeled 1839-1 and 1839-2). Further averaging would result in better values for D. On a whole, the image processing/data analysis gives reproducible results.

The fractal dimension for the heat-treated polymeric aerogel ($\rho_m = 0.66$ g/cm^3; 1728) is similar to its high-density ($\rho_m = 0.662$ g/cm^3; 1727) as-prepared counterpart. This suggests that heat-treatment effects up to a temperature of 1800° C are minimal in causing collapse of the mesopores. Raman studies [20, 21] (and Section 2.3.4) show that heat-treatment is more effective in changing the internal structure (nanopores) of the particles in the aerogel.

Preliminary fractal dimension studies have been done on the nanopore structure

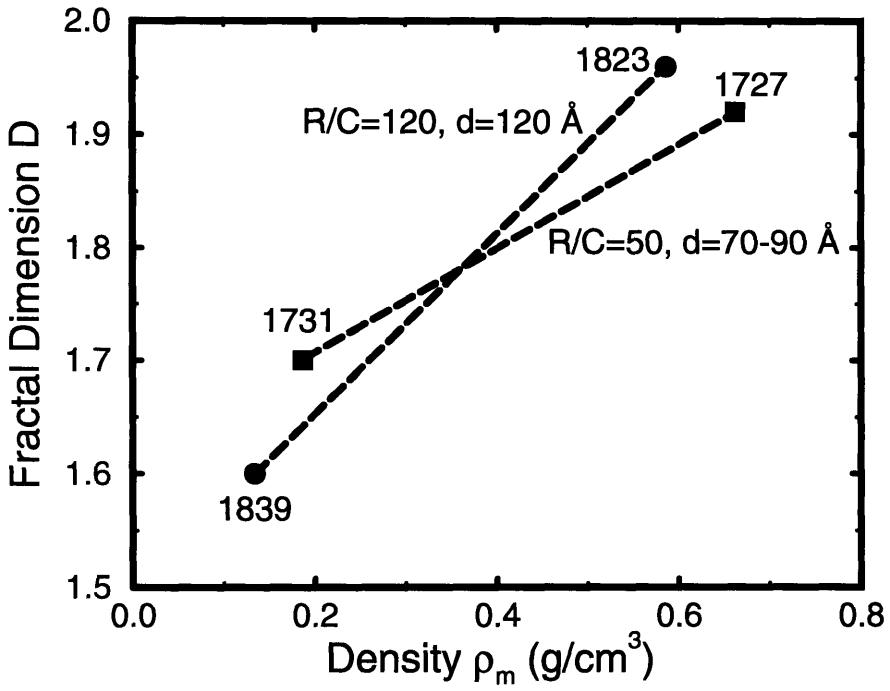

Figure 2-12: Fractal dimension, D, as a function of sample density for the nanopores (< 2 nm) in the carbon aerogels studied. The R/C molar ratios and corresponding particle sizes are shown. Dashed lines are drawn as guides to the eye. The magnification factor is 2×10^5. □ R/C=50: (1727) $\rho_m = 0.662$ g/cm^3; (1731) $\rho_m = 0.187$ g/cm^3; • R/C=200: (1823) $\rho_m = 0.586$ g/cm^3; (1839) $\rho_m = 0.134$ g/cm^3.

within the particles, under a magnification of 2×10^5. Figure 2-12 shows the fractal dimension versus ρ_m for a few polymeric and colloidal carbon aerogels listed in Table 2-3. The fractal dimension for the nanopores is seen to be independent of morphology/particle size, unlike that of the mesopores. As the nanopores are internal to the aerogel grains, this shows that the internal structure is similar for both polymeric and colloidal carbon aerogels, in agreement with the Raman studies to be discussed in the next section. Data were not available for the heat-treated sample. It will be interesting to note the heat-treatment effect on the nanopore structure.

The value of the fractal dimension $\sim 1.6 - 1.9$ for both the mesopores and the

nanopores, hints at the growth process for the carbon aerogel. Various aggregation models in 2 and 3 dimensional space have been assigned a corresponding fractal dimension. The values of D obtained here lean toward growth that is by a cluster-cluster formation. In other words, small clusters will form initially then stick to each other with some sticking probability to form larger and larger clusters. The appearance of the nanopores, mesopores and macropores in the carbon aerogel can be explained with this process. Nanopores are formed between clusters within the grains, mesopores are formed between individual clusters, and macropores are formed among groups of clusters. This model conforms to the growth pattern during the sol-gel synthesis.

2.3.4 Raman Spectroscopy

For a Raman spectroscopy measurement, the surface of the material being studied is illuminated with visible radiation (in the present work, an Argon ion laser source with an excitation energy of 4880 Å). Generally, the incident radiation interacts with the natural frequencies of the material, causing frequency shifts to lower or higher frequencies relative to the incident laser beam. These shifts in frequency (or wavenumber) are referred to as the Raman effect [22]. A plot of scattering intensity versus frequency shift constitutes a Raman spectrum. Each material has its own internal natural frequencies. Thus Raman spectroscopy serves as a way of identifying, or as it were, fingerprinting, any material.

The spectra in this work were taking at the Francis Bitter National Magnet Laboratory, using a 4880 Å Argon-ion laser as the excitation source. To avoid possible damage to the samples, the laser power applied to sample surfaces did not exceed 5 mW. The scattered radiation was collected with a series of optical lenses and mirrors, and focused onto a charge-coupled device (CCD) via a camera lens. By using a CCD detection system, a spectral range of $\sim$ 150 cm^{-1} could be collected simultaneously, as opposed to scanning the Raman shifts in a sequential fashion. The data collected

were plotted as Raman shift (in wavenumbers) versus intensity. To compare spectra, the intensities for each trace were plotted in arbitrary units. The general carbon aerogel spectra consist of two peaks, one Raman-allowed $E_{2_{g2}}$ mode centered at $\sim$ 1580 cm^{-1} (designated as the G band). This mode is close to the Raman-active mode of graphite at 1582 cm^{-1} [23]. The other peak, situated at $\sim$ 1355 cm^{-1}, corresponds to a maximal point in the phonon density of states, but not to a Raman-active mode. This second peak (designated as the D band), observed in disordered carbons, is attributed to in-plane disorder and a breakdown of $\mathbf{k}$=0 selection rules. Empirical studies [24] have shown that the ratio of the integrated intensity of the disorder-induced D band to that of the G band (i.e., I_D/I_G) is inversely proportional to the in-plane microcrystallite size, L_a. We can use the values of L_a as a measure of the structural order in disordered carbons.

The line shape of the peak near 1355 cm^{-1} is Lorentzian, while the line near 1580 cm^{-1} is generally asymmetric (due to a coupling between the discrete $E_{2_{g2}}$ Raman-allowed mode and a continuum of phonon states [25, 26]) and has a Breit-Wigner-Fano lineshape given by [27]:

$$I(\nu) = \frac{I_0[1 + 2(\nu - \nu_0)/q\Gamma]^2}{1 + [2(\nu - \nu_o)/\Gamma]^2} \quad , \tag{2.4}$$

where $I(\nu)$ is the frequency-dependent intensity, ν_0 the centre phonon position, Γ the full width at half maximum intensity of the Lorentzian line, and $1/q$ the coupling coefficient as described above ($1/q = 0$ for the Lorentzian line shape).

Raman spectrum of carbon aerogels

We can now examine the information obtained from Raman studies of RF- based carbon aerogels with various mass densities, ρ_m, particle sizes (R/C molar ratios) and heat-treatment temperatures (T_{HT}). Tables 2.4 and 2.5 list the parameters obtained by fitting the scattered intensity to Eqn. (2.4) via a least-squares-fit method.

Table 2.4: Raman parameters for polymeric (RF) carbon aerogels that were studied. The centre phonon frequency ν and full-width at half maximum Γ are shown for the graphite (1580 cm^{-1}) and the disorder-induced (1360 cm^{-1}) lines. Also shown are the values as obtained from fits to Eqn. (2.4) for the coupling coefficient 1/q, the ratio of the integrated intensities (I_{1360}/I_{1580}) and the in-plane microcrystallite size, L_a (as calculated using Knight's empirical formula).

R/C	50	50	50	50
Density(g/cm^3)	0.182	0.672	0.170	0.190
T_{HT}(° C)	1050	1050	1500	1800
ν_{1360} (cm^{-1})	1350	1355	1350	1348
Γ_{1360} (cm^{-1})	141	128	63	50
ν_{1580} (cm^{-1})	1609	1614	1599	1586
Γ_{1580} (cm^{-1})	82	77	61	50
$1/q$	-0.24	-0.23	-0.09	-0.02
I_{1360}/I_{1580}	1.8	1.8	1.4	1.1
L_a (Å)	24	24	31	40

Comparisons are then made with the PF-based carbon aerogel system.

Density effects

Figure 2-13(a) shows the Raman spectra (i.e., Raman intensity versus Raman frequency shift) for colloidal carbon aerogels with R/C=200 and various mass densities. Figure 2-13(b) shows the corresponding results for the polymeric aerogel with R/C=50. Solid lines represent a fit of the data to Eqn. (2.4). As the density of the aerogel is increased, the effect is a reduction in the integrated intensity of the disorder-induced peak, as is seen in Tables 2.4 and 2.5. The coupling constant, $1/q$, is not affected by density increases. This shows that the continuum and the distinct graphite mode do not decouple with an increase in mass density. The in-plane microcrystallite size, L_a, is not affected by changes in mass density. This suggests that the structure internal to both the polymeric and colloidal carbon aerogel particles is the same, irrespective of ρ_m. Hence, an increase in sample density affects only the packing of the particles within the aerogel, and not the internal structure of these particles.

Table 2.5: Raman parameters for colloidal (RF) carbon aerogels that were studied. The centre phonon frequency ν and full-width at half maximum Γ are shown for the graphite (1580 cm^{-1}) and the disorder-induced (1360 cm^{-1}) lines. Also shown are the values as obtained from fits to Eqn. (2.4) for the coupling coefficient 1/q, the ratio of the integrated intensities (I_{1360}/I_{1580}) and the in-plane microcrystallite size, L_a (as calculated using Knight's empirical formula).

R/C	200	200	200	300	300	300	300
Density(g/cm^3)	0.123	0.451	0.670	0.117	0.801	0.78	0.66
T_{HT}(° C)	1050	1050	1050	1050	1050	1500	1800
ν_{1360} (cm^{-1})	1349	1350	1350	1350	1354	1354	1349
Γ_{1360} (cm^{-1})	143	124	123	150	133	62	59
ν_{1580} (cm^{-1})	1604	1610	1607	1604	1613	1599	1596
Γ_{1580} (cm^{-1})	86	76	73	83	77	62	61
$1/q$	-0.23	-0.25	-0.25	-0.21	-0.22	-0.08	- 0.09
I_{1360}/I_{1580}	1.5	1.7	1.6	1.7	2.0	1.4	0.97
L_a(Å)	29	26	27	25	23	31	45

This internal structure, the smallest unit as measured by Raman spectroscopy, are graphitic ribbons, and are on the order of 25 Å. This result has been corroborated by high resolution TEM studies that show the aerogel particle to consist of interconnected graphitic ribbons [11]. Helium pycnometry [28] shows the skeletal density of these ribbons to be 2.06 ±0.06 g/cm^3 for carbon aerogels with R/C=200. This value is close to that of graphite (ρ_g = 2.26 g/cm^3), implying that these ribbons are fairly graphite-like in structure. It should be noted here that for these small values of L_a the Raman effect does not determine L_a very sensitively.

Particle size effects

Figure 2-14 shows the Raman spectra for three as-prepared (T_{HT} = 1050°C) low-density aerogel samples with various particle sizes, ranging from 70 Å to 150 Å. The order of magnitude of the in-plane crystallite size L_a (see Tables 2.4 and 2.5) implies once again that Raman spectroscopy is most likely probing the dimension of the graphitic filaments within the carbon aerogel particles. Again, the values of L_a are

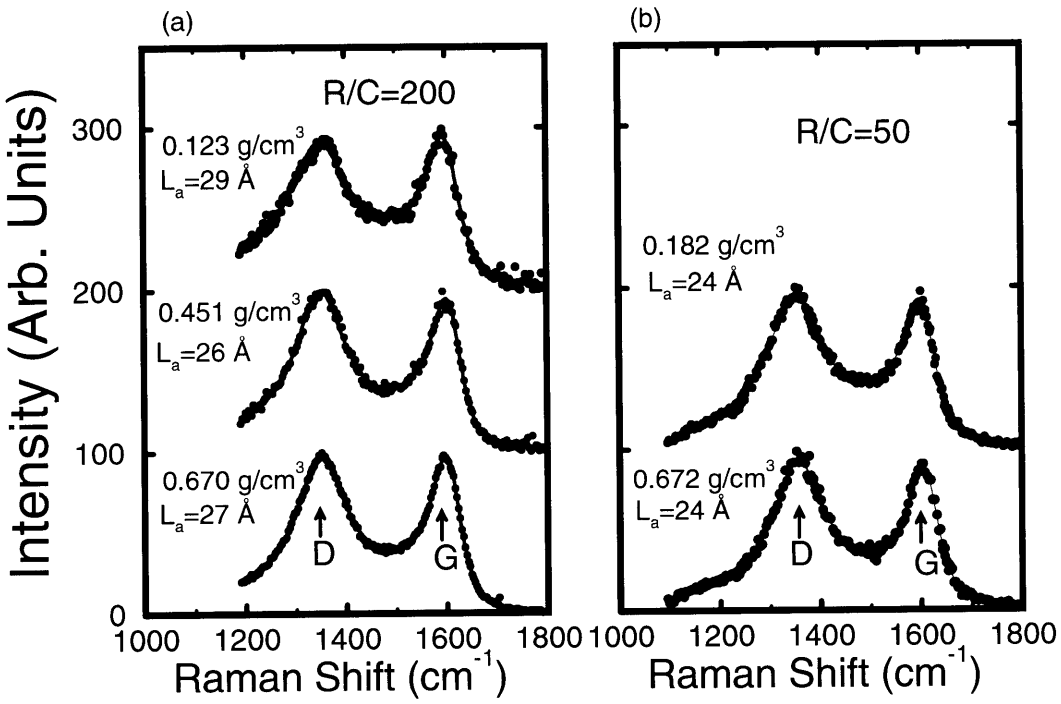

Figure 2-13: Density effects on the Raman spectra of as-prepared ($T_{\mathrm{HT}} = 1050°$ C) carbon aerogels with (a) R/C=200 and (b) R/C=50, showing the disorder-induced (D) (1360 cm^{-1}) and the Raman-active (G) (1580 cm^{-1}) lines. Solid lines are fits of the data to Eqn. (2.4).

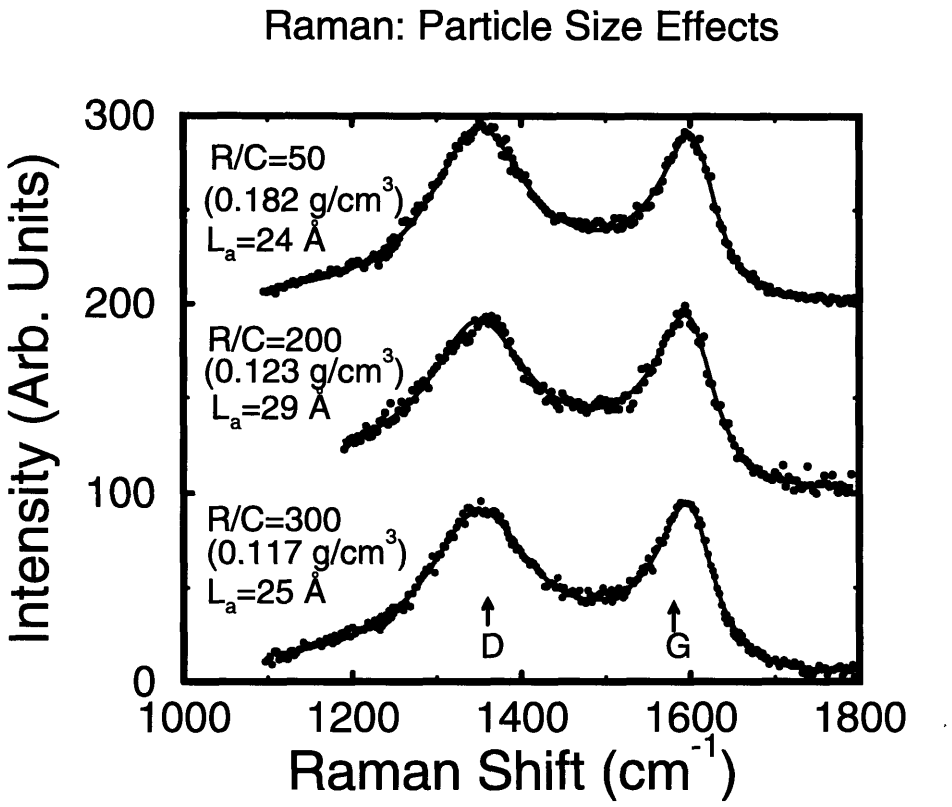

Figure 2-14: Particle size effects on the Raman spectra of three low-density as-prepared carbon aerogels, showing the disorder-induced (1360 cm^{-1}) and the Raman-active (1580 cm^{-1}) lines. The particle sizes can be determined from the R/C ratio as follows: R/C=50 $\sim$ 70 – 90 Å, R/C=200 $\sim$ 120 Å, R/C=300 $\sim$ 150 Å. Solid lines are fits of the data to Eqn. (2.4).

similar, suggesting that the structural order internal to the particles of the carbon aerogels is approximately the same, irrespective of the particle size (R/C molar ratio).

Heat-treatment effects

Figure 2-15 shows that, for the same R/C=50 molar ratio, increasing the heat-treatment temperature up to 1800°C reduces the integrated intensity of the disorder peak, resulting in a larger value of L_a (see Tables 2.4 and 2.5). This behaviour is also observed in the R/C=300 samples (Fig. 2-16) and is consistent with the idea that

heat-treatment anneals the microscopic disorder to a large degree (but not completely) and induces in-plane order development in carbon aerogels [29, 30]. Figure 2-17 summarizes the effects of heat-treatment on L_a.

Increases in T_{HT} tend to down-shift the G-band toward 1580 cm^{-1}. This can be explained by noting the presence of a peak at 1620 cm^{-1} in the phonon density of states for graphite. Increases in disorder tend to broaden this peak, causing it to overlap with the neighbouring 1580 cm^{-1} line and resulting in up-shifted peaks with decreases in heat-treatment temperature. Increases in T_{HT} reverse this trend. The lineshape of the G-band also becomes more symmetric ($1/q \rightarrow 0$). The aerogels are tending toward a more graphitic structure with heat-treatment above 1500°C.

It should be noted that all the RF-based aerogels tend to exhibit Raman-active lines that are up-shifted in frequency from the 'ideal' 1580 cm^{-1} line. Other than the presence of disorder, another reason for this shift is a transfer of charge to the graphite layers. The presence of p-type behaviour has been shown to cause frequency upshifts, while donor sites are responsible for frequencies shifted down from the 1580 cm^{-1} line [23].

Raman spectra of PF-based aerogels

Table 2.6 shows the Raman parameters of the PF-based aerogels that were studied. The in-plane microcrystallite sizes, L_a, are on the same order as those of the RF-based carbon aerogels. Figure 2-18 shows the in-plane microcrystallite size versus ρ_m for PF-based and RF-based aerogels with $T_{HT} = 1050$°C. Changes in ρ_m do not affect L_a, once again suggesting that the internal structure of these newer aerogels is also similar. Heat-treated samples of the PF-based aerogels were not available for study, but we surmise that the trends will be similar to the heat-treatment RF-based studies discussed above.

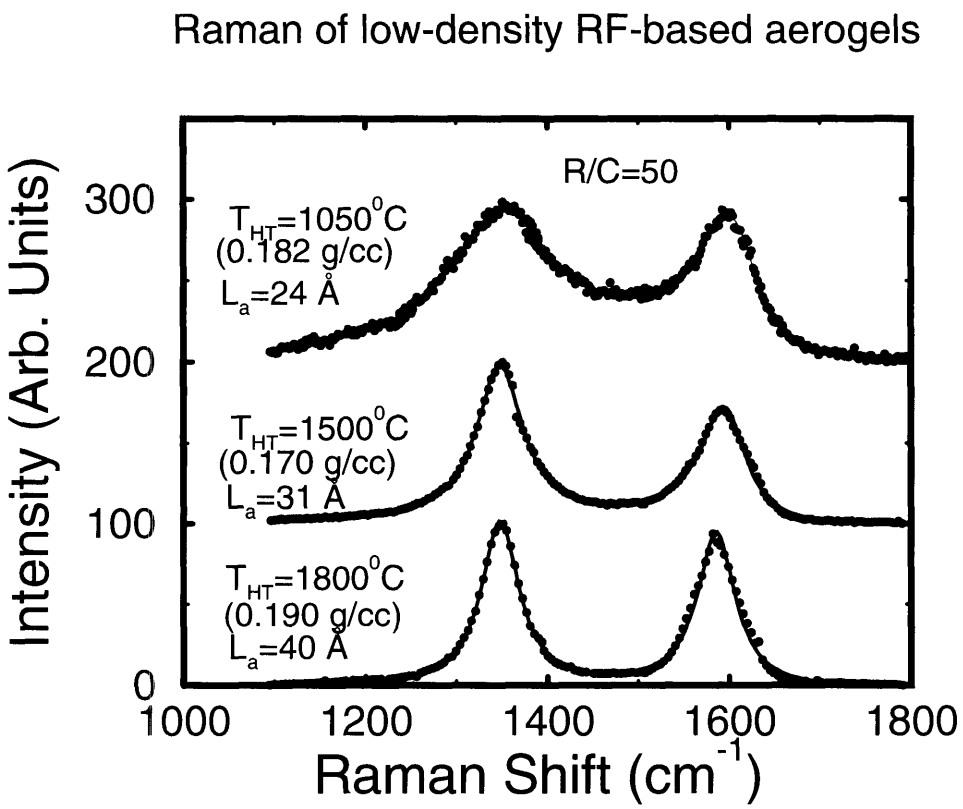

Figure 2-15: Heat-treatment effects on the Raman spectra of three low-density as-prepared polymeric carbon aerogel samples, showing the disorder-induced (1360 cm^{-1}) and the Raman-active (1580 cm^{-1}) lines. Solid lines are fits of the data to Eqn. (2.4).

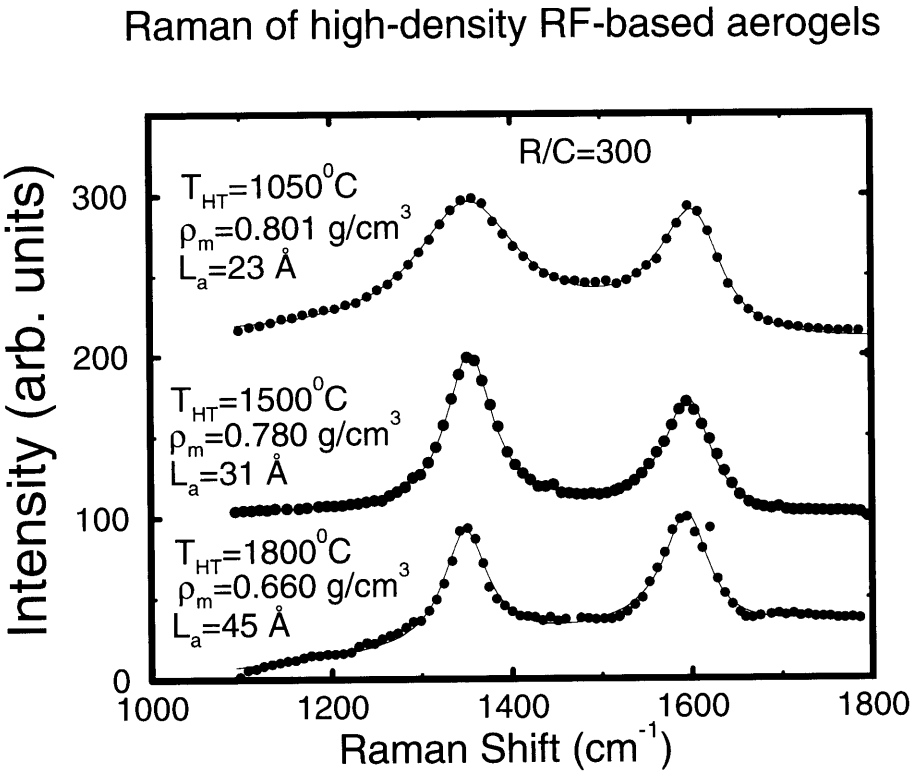

Figure 2-16: Raman spectra of three high-density as-prepared carbon aerogel samples with various heat-treatment temperatures and R/C=300, showing the disorder-induced (1360 cm^{-1}) and the Raman-active (1580 cm^{-1}) lines. Solid lines are fits of the data to Eqn. (2.4).

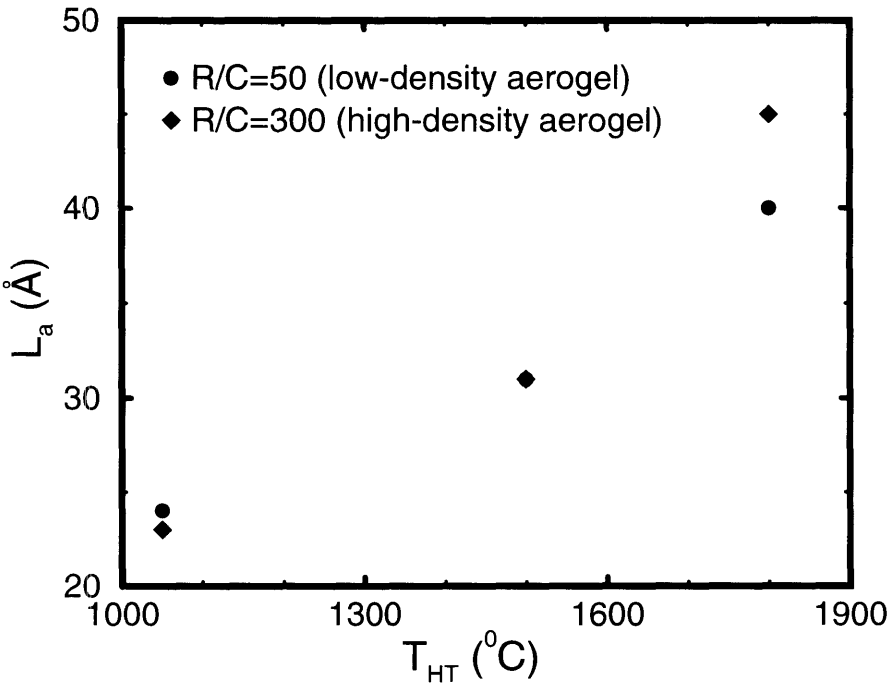

Figure 2-17: Heat-treatment effects on the in-plane microcrystallite size, L_a for the polymeric (R/C=50) and colloidal (R/C=300) carbon aerogels shown in Figs. 2-15 and 2-16, respectively.

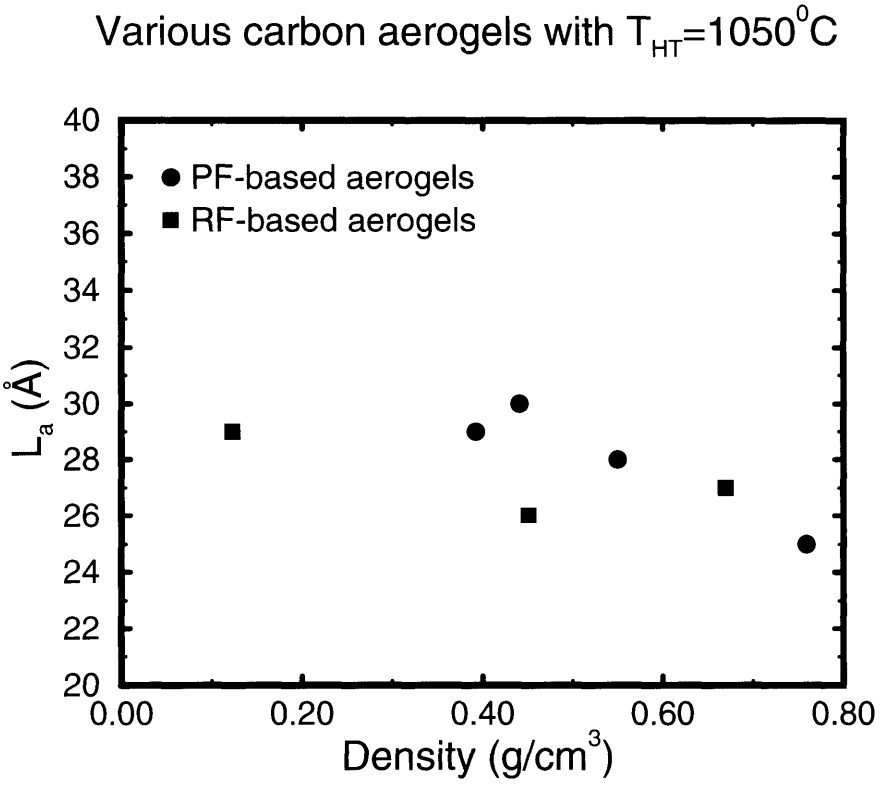

Figure 2-18: Comparison of the in-plane microcrystallite size L_a as a function of ρ_m for low-density PF- and RF-based carbon aerogels. There is evidence of a slight density dependence, with L_a decreasing with increases in ρ_m. However, this effect is very small when compared to the effects of changes in T_{HT} in Fig. 2-17.

Table 2.6: Raman parameters for (PF) carbon aerogels. The centre phonon frequency ν and full-width at half maximum Γ are shown for the graphite (1580 cm^{-1}) and the disorder-induced (1360 cm^{-1}) lines. Also shown are the values as obtained from fits to Eqn. (2.4) for the coupling coefficient 1/q, the ratio of the integrated intensities (I_{1360}/I_{1580}) and the in-plane microcrystallite size, L_a (as calculated using Knight's empirical formula).

Density(g/cm^3)	0.393	0.441	0.550	0.759
T_{HT}(° C)	1050	1050	1050	1050
ν_{1360} (cm^{-1})	1353	1353	1352	1353
Γ_{1360} (cm^{-1})	135	131	133	126
ν_{1580} (cm^{-1})	1603	1603	1605	1607
Γ_{1580} (cm^{-1})	82	83	82	69
$1/q$	-0.23	-0.15	-0.15	-0.18
I_{1360}/I_{1580}	1.5	1.5	1.6	1.8
L_a (Å)	29	30	28	25

2.3.5 Magnetic Susceptibility

Magnetic susceptibility (χ) measurements give a measure of the disorder in a given material through study of the paramagnetic contributions of unpaired electron spins to χ.

The magnetic susceptibility measurements were carried out in a Superconducting Quantum Interference Device (SQUID) Magnetometer built by Quantum Design. The magnetic field in this magnetometer points along the **z** direction, resulting in transverse magnetic susceptibility measurements. After weighing the samples, they are then mounted in drinking straws. and held in place within the straw with cotton. The straw is then lowered into an outer chamber of the SQUID magnetometer where evacuation of the sample space occurs. This evacuation helps to prevent the solidification of moisture and air in the straw as the system temperature is lowered from room temperature to 4 K. This evacuation is useful because oxygen, having a triplet ground state, contributes to the paramagnetic susceptibility. Once the sample space is evacuated, the sample can be lowered into the space containing the superconducting

magnet.

The SQUID is controlled by computer. There are settings for first centering the sample within the magnet. Measuring the susceptibility of the sample takes place using a scanning method, i.e., moving the sample up and down in the measurement coil. This results in an induced EMF in the coil, which is picked up by the probe and amplified. After signal processing, the amplified signal is then converted into a magnet moment readout. A scan length of 6 cm was used for this work.

Diamagnetism in graphite

For a free atom in the presence of a magnetic field, a magnetic moment can be measured as a result of: (a) the spin angular momentum inherent to the electrons about the atom, (b) the orbital angular momentum of these electrons about the nucleus, and (c) the induced moment due to the field. The first two effects result in paramagnetic behaviour, while the last effect results in diamagnetism.

Earlier studies [31, 32] have shown that graphite exhibits a very large magnetic anisotropy. In particular, the susceptibility perpendicular to the hexagonal basal plane, $\chi_\perp$, has a temperature dependence and is on the order of -21.5×10^{-6} emu/gm at room temperature. The value of the susceptibility along the basal plane, $\chi_\parallel$, is much smaller, on the order of -0.5×10^{-6} emu/gm. The value $\chi_e = (\chi_\perp - \chi_\parallel)$ tends toward a temperature independent value of $\sim -30 \times 10^{-6}$ emu/gm at low temperature [8]. This large anisotropy in the magnetic properties of graphite has been explained by McClure [33, 34] via electron energy band structure considerations.

The earlier work by Ganguli and Krishnan [32] also shows that the large anisotropy leads to free electron motion in the basal plane. However, there is no evidence of paramagnetism in graphite. The absence of a paramagnetic term in graphite has been attributed by Ganguli and Krishnan to occupation of energy levels by pairs of

[8] For this work, the diamagnetic term for graphite can thus be considered temperature-independent with an average value of -7×10^{-6} emu/gm for the range of temperatures studied here.

Table 2.7: Susceptibility values for RF-based carbon aerogels with R/C=50 and R/C=300. The data show values for the unpaired spin density (N) and the temperature-independent susceptibility, χ_0.

R/C	50	50	50	300	300
Density(g/cm^3)	0.182	0.672	0.190	0.117	0.801
T_{HT}(° C)	1050	1050	1800	1050	1050
N(10^{19} spins/g)	21	8.8	1.6	2.3	5.9
χ_0 (10^{-6} emu/g)	-2.1	-1.3	-0.27	-0.71	-1.1

Table 2.8: Susceptibility values for RF-based carbon aerogels with R/C=200

R/C	200	200	200	200	200	200	200	200
Density(g/cm^3)	0.134	0.128	0.133	0.542	0.571	0.565	0.123	0.670
T_{HT}(° C)	700	800	900	700	800	900	1050	1050
N(10^{19} spins/g)	9.3	5.8	4.7	9.0	5.8	4.5	2.8	1.5
χ_0 (10^{-6} emu/g)	–	–	–	-0.19	-0.36	-0.50	-2.3	- 1.0

electrons.

Susceptibility results

Tables 2.7 and 2.8 give the susceptibility parameters for the various RF-based carbon aerogels studied. From the tables, it can be seen that for fixed densities and heat-treatment temperatures, as the particle size is reduced, the number of unpaired spins increases. This is in agreement with studies that show that the polymeric carbon aerogels have larger specific surface areas than colloidal carbon aerogels [4, 5, 35]. Hence, smaller particles have more dangling bonds which make the material more susceptible to unpaired spins. The polymeric RF-based carbon aerogels are more microscopically disordered (see definition in Section 2.1) than their colloidal counterparts. The susceptibility hints at being a better measure of the surface area present in the aerogel than gas adsorption techniques.

To visualize some of the data in the tables, the effects of density and heat-

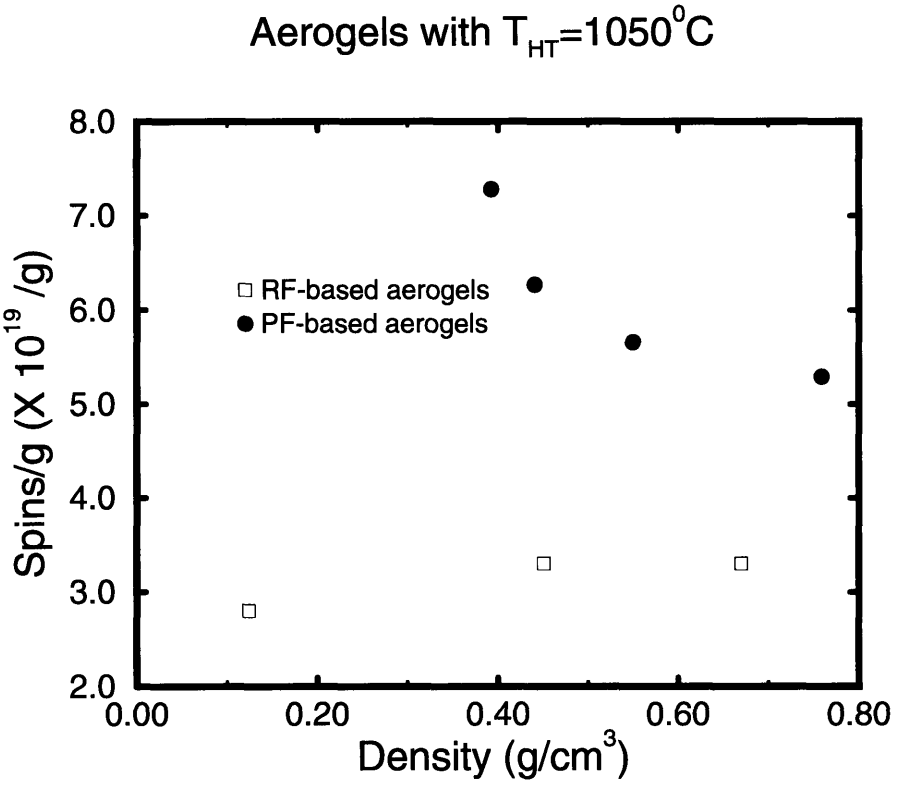

Figure 2-19: Density effects on the unpaired spins present in carbon aerogels. The RF-based aerogels have R/C=200 and T_{HT}=1050° C.

treatment changes are shown graphically in Figs. 2-19 and 2-20, respectively. For as-prepared carbon RF- and PF-based aerogels, Fig. 2-19 shows that increases in ρ_m do not have a pronounced effect on the number of unpaired spins per gram for the (RF) carbon aerogels.

Data for the PF-based aerogels show a slight dependence of N on density (see Fig. 2-19). The Raman spectra do not show any corresponding changes in L_a.

With heat-treatment, the number of unpaired spins per gram is seen to decrease, as shown in Fig. 2-20. This is consistent with the results of the Raman spectra which indicate that heat-treatment anneals disorder in the system, resulting in partial graphitization. Heat-treatment results in pore collapse, which is evidenced not only by a reduction in surface area [8] but also by the reduction in the number of unpaired

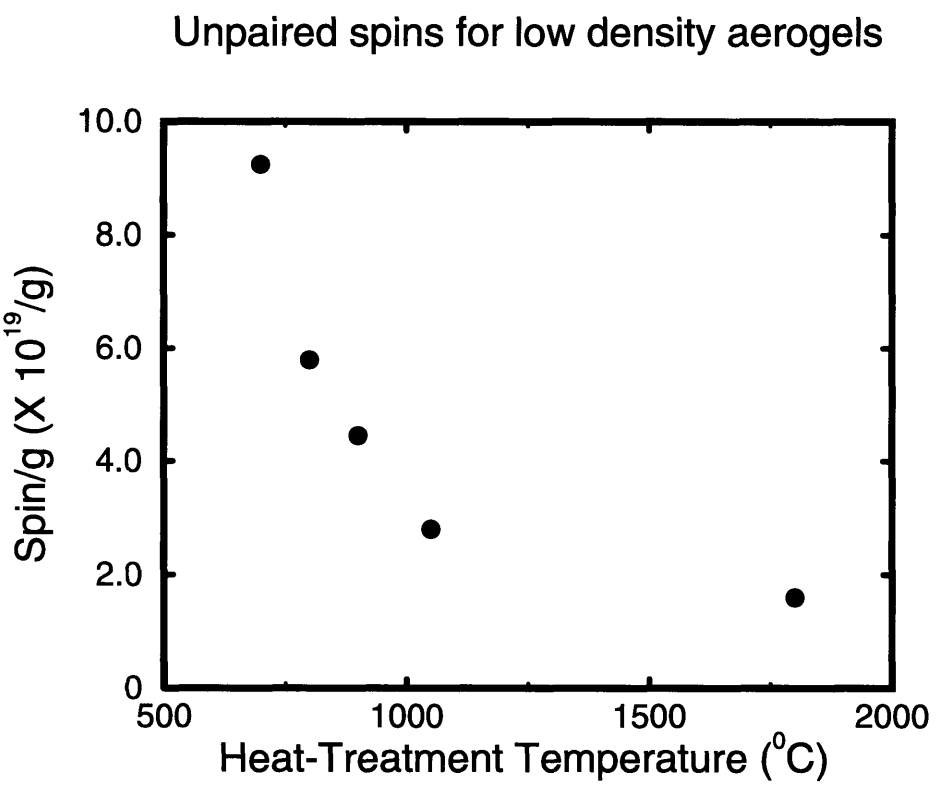

Figure 2-20: Heat-treatment effects on the unpaired spins present in carbon aerogels. Except for the 1800° C point (R/C=50, ρ_m = 0.190 g/cm^3), the data are for the colloidal R/C=200 low- density RF-based carbon aerogels with ρ_m = 0.13 $\pm$ 0.01 g/cm^3.

spins. The magnitude of χ_0 increases with heat-treatment as the system tends towards the average graphite value. This increase in χ_0 correlates with the observed increase in L_a with an increase in heat-treatment temperature.

2.4 Results

Chapter 2 has given an introduction to the structure of the carbon aerogel material (RF and PF-based). These materials have an intricate morphology which is intimately linked to the initial chemical synthesis. The aerogels studied consist, in general, of a connected network of carbon particles (grains) in a porous insulating ma-

trix. The interconnectivity of the particles depends on the particle size, mass density and heat-treatment temperature. The internal structure of the particles consists of an intertwined network of graphitic ribbons which do provide some connection between the particles. The internal graphitic network leads to the formation of nanopores within the particles. Heat-treatment is seen to be most effective in untangling the internal graphitic ribbon structure and causing pore collapse, making the aerogel more ordered. The dangling bonds that are present result in a topological type of disorder. The fractal analysis of the mesopores and nanopores suggests that the aggregation process follows a cluster-cluster formation, giving rise to the various porous dimensions exhibited by the carbon aerogel. The similarity of the fractal dimension of the nanopores confirms the Raman studies that have shown that the internal structure of the aerogels is the same for polymeric and colloidal carbon aerogels.

Most of the studies on aerogels have concentrated on obtaining dimensions and distributions for the porous network and the particles inherent to this system. In Chapter 3, the next step is taken towards understanding how the structure, in particular the solid particle matrix, contributes to the electrical transport in these materials. The carbon aerogels are the first conducting organic aerogels to be made. It will be shown in Chapter 3 that the structural parameter changes discussed here in Chapter 2 have effects on the transport behaviour.

Chapter 3

Electronic Transport Properties

Now that we are more familiar with the structure of the materials we are studying, we can begin to discuss the basic transport mechanisms that can be observed in these disordered materials. Chapter 3 examines the temperature-dependence of the electrical conductivity and transverse magnetoresistance as functions of parameters such as mass density, R/C molar ratio and heat-treatment temperature. The mesoscopic disorder inherent to the aerogel system is seen to lead to localization effects at low temperature. The effects of parameters in the localization and the role they play near the Insulator-Metal-Transition (IMT) are examined. A type of variable range hopping is used to explain the observed transport behaviour.

3.1 Experimental Setup

3.1.1 Conductivity Measurements

Transport measurements generally entail a four-point contact configuration i.e., a constant current is applied to the sample and the resulting voltage drop across the sample is measured. The samples are machined [1] for use in transport measurements

[1] Work carried out at Lawrence Livermore National Laboratory.

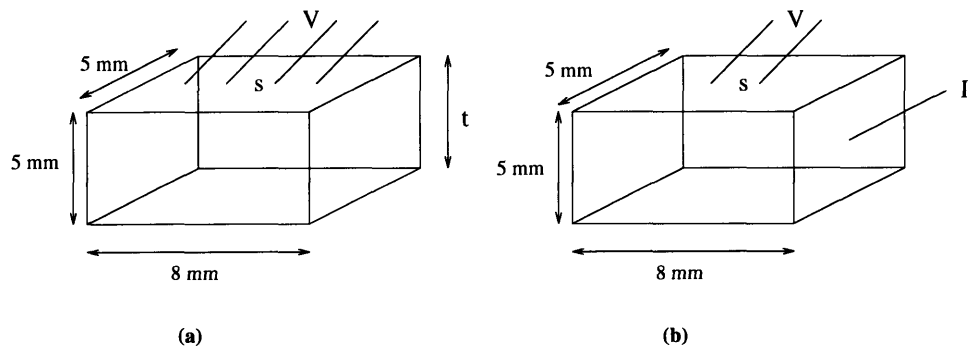

Figure 3-1: Various ways the contacts can be mounted onto samples: (a) Contacts placed col-linearly; (b) current contacts placed on the end faces, voltage leads on the surface of the sample.

by first being placed on a specially-designed vacuum chuck and then cut with a diamond-tipped tooling. The resulting machined samples have dimensions on the order of $\sim 8 \times 5 \times 5$ mm^3. Figures 3-1(a) and (b) show that contacts can be placed i) col-linearly on the surface of the sample (Fig. 3-1(a)) or ii) having the current passing through the end faces and measuring the voltage from the top (Fig. 3-1(b)). Both techniques result in the same temperature-dependent resistance, in feature as well as magnitude. By placing the the contacts col-linearly, the conductance can be calculated using [36]:

$$\sigma = \frac{I}{2\pi V s} \tag{3.1}$$

where V is the measured voltage, I is the applied current, and s is the spacing between contacts, with $s < t$, the sample thickness. For the present work, s is on the order of 0.5 to 1 mm.

By placing the current leads on the end faces of the sample and measuring the voltage from the top, then:

$$V = IR \tag{3.2}$$

and the conductance can be calculated from:

$$\sigma = (sI)/(VA) \tag{3.3}$$

where A is the samples cross-sectional area and s is the spacing between the voltage electrodes.

Once contacts are made to the sample, they are mounted onto integrated circuit (IC) chip carriers and placed into IC plugs in a sample holder. A copper tubing which serves as a heater is then placed around the sample. This ensures uniform cooling/heating of the samples. The sample holder is then placed into an inner jacket, which in turn is placed into the inner jacket of a Janis cryostat. By evacuating the sample space and the outer jacket surrounding the sample space and introducing a small amount of helium gas into these spaces, thermal cooling can occur. A constant current is passed though the samples and the voltage is measured. To minimize Joule heating effects, a power less than 10^{-7} Watts is applied to the sample. Temperature scans are taken by cooling the samples to 4.2 K and waiting for sample equilibrium before taking data via a natural warming process. The temperature and sample voltage are collected via computer.

3.1.2 Magnetoresistance Measurements

The transverse magnetoresistance studies were carried out at the Francis Bitter National Magnet Lab (FBNML) in a magnet capable of going to fields of 20 Tesla. Samples are mounted on a New Universal Sample Holder (NUSH) card which provides contact to equipment outside the cryostat via electrical feedthroughs. The NUSH card is also designed to provide the samples with thermal contact. Once samples are mounted to the NUSH, they are surrounded with a copper tubing which serves as the heater. This creates an enclosed space where the samples can gain uniform thermal equilibrium. The temperature of the system is measured with a Carbon glass resis-

tor, the temperature control being provided by a Capacitance meter. All these have contacts on the NUSH. After samples are mounted and all contacts are checked, the cryostat is lowered into the 2-inch bore of the magnet, making sure that the samples are centered in the magnet. Once the samples are centered, the system is ready to take data. Temperature control below 4.2 K (down to 1.4 K) is achieved by pumping on liquid Helium in the cryostat. Data acquisition is done with a Macintosh system. Currents are provided to each sample, and the voltages are measured. The magnetic field is directed along the **z** direction and is perpendicular to the current through the sample. This is defined as *transverse* magnetoresistance. The voltage changes, magnetic fields and temperatures are stored in a file. Once thermal equilibrium is reached, and the sample resistances are in equilibrium, the magnetic field is ramped from 0 Tesla to 15 or 20 Tesla. The ramp speed can be varied from 0.2 minutes to 20 minutes. However, to ensure that the samples' resistances follow the field, ramp times are set at 10 minutes. The field is also ramped down, to ensure that there are no shifts due to temperature changes. As the data is collected, the data acquisition for the samples can be seen on the computer screen in real time. After the magnetoresistance studies are done, the system can be cooled to 1.5 K. By operating in zero field, low-temperature conductivity measurements can be obtained as the sample is allowed to warm up naturally from 1.5 K.

3.2 Experimental Results: Electrical Conductivity

Figures 3-2 to 3-4 show typical semi-log plots of the electrical conductivity (σ) versus temperature (T) for a few of the (RF and PF) carbon aerogel samples studied. Figure 3-2 examines the density effects, while Figs. 3-3 and 3-4 show the heat-treatment and particle size effects, respectively. The room temperature conductivity of the high-density samples is generally an order of magnitude higher than the low-density

Table 3.1: Showing the effects of density changes on the electrical conductivity of as-prepared (T_{HT} = 1050° C) colloidal carbon aerogels (Resorcinol/Catalyst molar ratio = 200).

ρ_m (g/cm^3)	0.118	0.449	0.646
σ(300 K) (S/cm)	0.85	8.1	22.0
T_{HT} (° C)	1050		

Table 3.2: Showing the effects of heat-treatment temperature (T_{HT}) on the electrical conductivity for colloidal (RF) aerogels. For a fixed density type, (high- or low-density), the conductivity increases with an increase in T_{HT}.

T_{HT} (° C)	1050	1500	1800	1050	1500	1800
ρ_m (g/cm^3)	0.103	0.117	0.137	0.646	0.621	0.635
$\sigma(300K)$ (S/cm)	0.74	1.02	1.60	22	42.36	65.0
R/C	200					

samples, irrespective of heat-treatment temperature or particle size.

Before examining the temperature-dependence of the conductivity, we can look at the effects of variations in physical parameters on the electrical conductivity. Tables 3.1 to 3.3 show these effects. Of all the parameters that can be varied in the aerogel system, density (particle packing) is the most effective in determining the properties of the aerogel (see Table 3.1). Heat-treatment and particle size changes help to enhance (or degrade) the observed properties. For example, in Table 3.2, heat-treatment is seen to be more effective in enhancing the room-temperature dark conductivity of the high-density samples than that of the low-density samples. The (electrical) contacts between grains is further enhanced by heat-treatment. In Table 3.3, it is harder to pick out the particle size effects from the density effects. Generally, the trend shows that an increase in particle size increases the conductivity.

Table 3.3: Showing the effects of particle size changes on the electrical conductivity. Particle sizes for polymeric carbon aerogels (R/C=50) are $\sim$ 70-90 Å, while the R/C=200 and R/C=300 carbon aerogels have sizes of 120 and 150 Å, respectively. For the low-density polymeric carbon aerogel, the larger room-temperature conductivity (as compared to the low-density R/C=200 and 300 carbon aerogels) could also be associated with the slightly larger density of this sample.

R/C	50	200	300	200	300
ρ_m (g/cm^3)	0.182	0.123	0.117	0.670	0.801
σ(300 K) (S/cm)	1.3	0.61	0.65	16.4	46.6
T_{HT} (° C)	1050				

3.2.1 Effects of Physical Parameters on σ

Density effects

Previous studies [20, 37] have shown that increases in mass density, ρ_m, result in increases in the conductivity σ. Figure 3-2, a semi-log plot of σ versus T, shows this general behaviour. The inset shows that the trend continues with the PF-based carbon aerogels. Note that the PF-based samples shown do not have as large a density range as the RF-based carbon aerogels. As the mass density decreases, there is an overall decrease in the conductivity. Also, these is a pronounced increase in the temperature-dependence of σ at low temperatures (below 30 K) with decreasing ρ_m. These results can be attributed to the packing of the particles. Conduction pathways are reduced with decreases in density, leading to a more localized behaviour in σ(T).

Heat-treatment effects

Referring to Fig. 3-3 we can see the striking effect of heat-treatment on the dark-conductivity. The highest density samples, heat-treated at 1500° C and 1800° C, show little measurement temperature dependence in the conductivity, though as-prepared (T_{HT} = 1050° C) high-density samples generally exhibit a stronger σ(T) dependence similar to the behaviour for the low-density samples, as shown in Fig. 3-2. Thus,

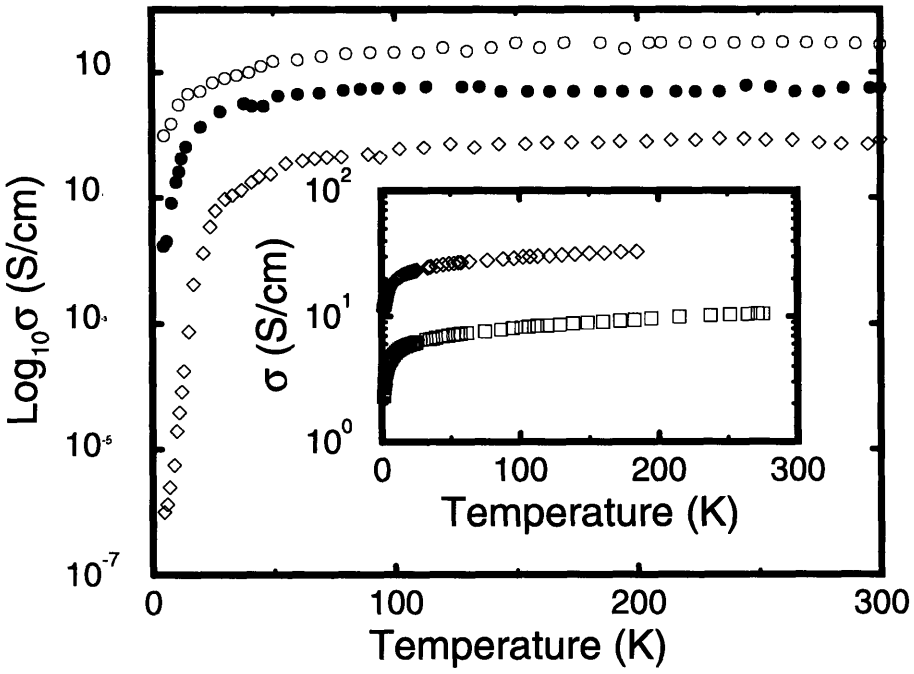

Figure 3-2: Semilog-plot of dark-conductivity (σ) versus measurement temperature (T) showing the density effects for as-prepared (T_{HT} = 1050° C) (RF) carbon aerogels with R/C=200. The inset shows a corresponding plot for the PF-based carbon aerogels. ○ : ρ_m = 0.646 g/cm^3; ● : ρ_m = 0.449 g/cm^3; ◇ : ρ_m = 0.118 g/cm^3; Inset (PF-based carbon aerogels): ◇ : ρ_m = 0.753 g/cm^3; □ : ρ_m = 0.383 g/cm^3.

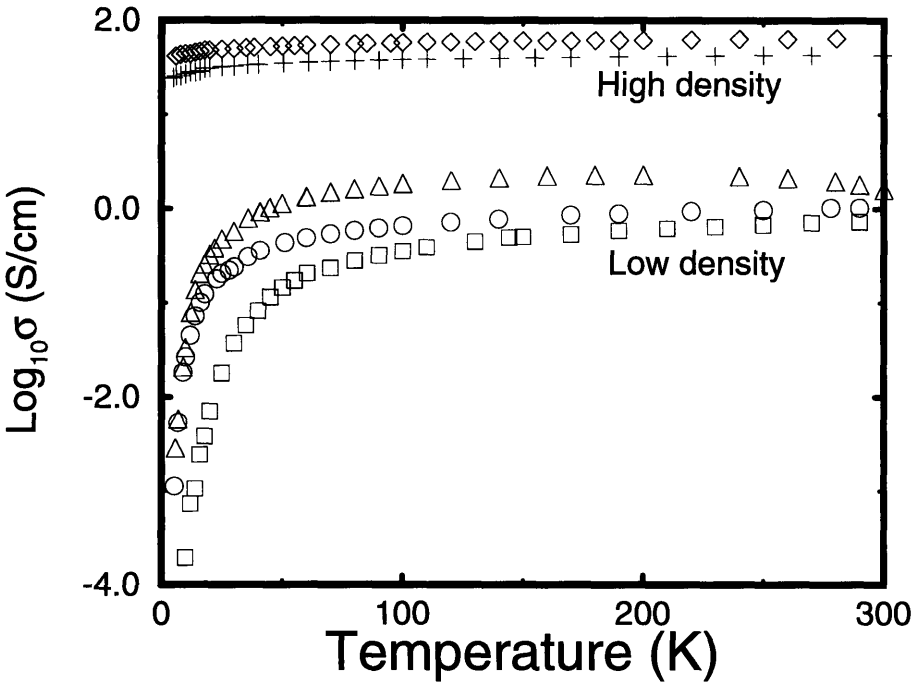

Figure 3-3: Semilog-plot of dark-conductivity (σ) versus temperature showing the heat-treatment effects for the (RF) carbon aerogel samples studied. □:T_{HT}=1050° C, ρ_m = 0.103 g/cm^3; ○:T_{HT}=1500° C, ρ_m = 0.117 g/cm^3; △:T_{HT}=1800° C, ρ_m = 0.137 g/cm^3; +:T_{HT}=1500° C, ρ_m = 0.621 g/cm^3; ◇:T_{HT}=1800° C, ρ_m = 0.635 g/cm^3. For the T_{HT}=1800° C (ρ_m=0.635 g/cm^3) and T_{HT}=1500° C (ρ_m=0.621 g/cm^3) high-density samples, the temperature dependence of the conductivity is very weak.

heat-treatment has a very large effect on the dark conductivity of the high-density carbon aerogel samples, though most of the change in σ(T) is realized before T_{HT} has reached 1800° C. The small temperature dependence in the conductivity for the high-density samples above 1500° C signifies that a metallic regime is reached with the high-density samples. We can consider T_{HT} = 1500° C to define the temperature at which the Insulation-Metal-Transition (IMT) point is reached in the carbon aerogel system. This agrees with the Raman studies of Section 2.3.4 which show that changes in the Raman spectra are more pronounced above 1500° C.

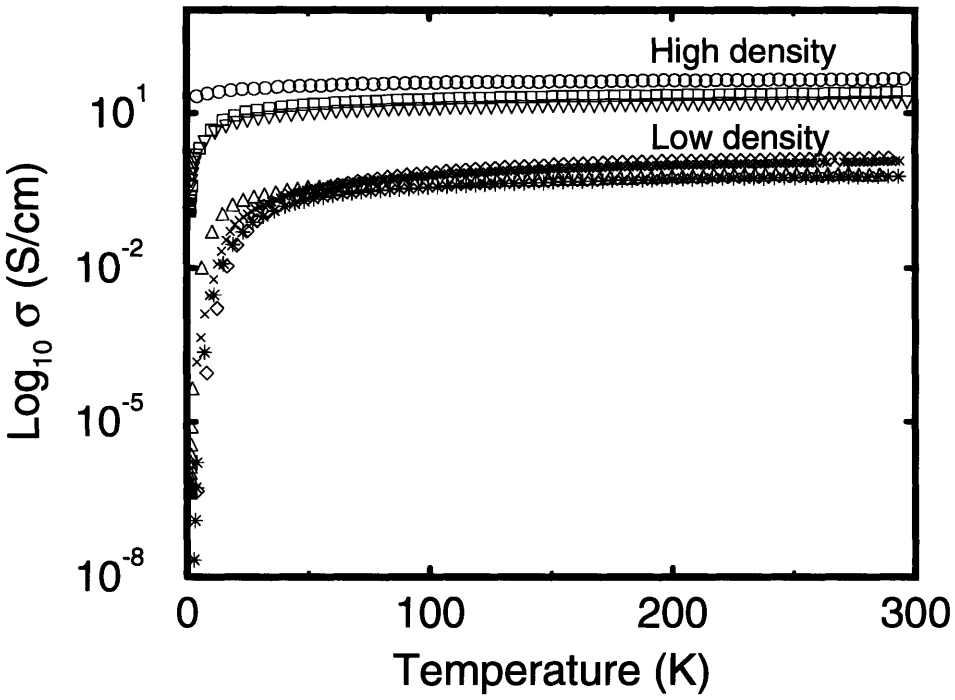

Figure 3-4: Plot of $\log_{10}\sigma$ versus T showing the particle-size effects for the (RF) carbon aerogels studied. ○: R/C=300, ρ_m=0.801 g/cm^3; □:R/C=50, ρ_m=0.672 g/cm^3; ▽: R/C=200, ρ_m=0.670 g/cm^3; △: R/C=300, ρ_m=0.117 g/cm^3; ∗: R/C=200, ρ_m=0.123 g/cm^3; ◇: R/C=50, ρ_m=0.182 g/cm^3; ×: R/C=50, ρ_m=0.190 g/cm^3; T_{HT}=1800° C.

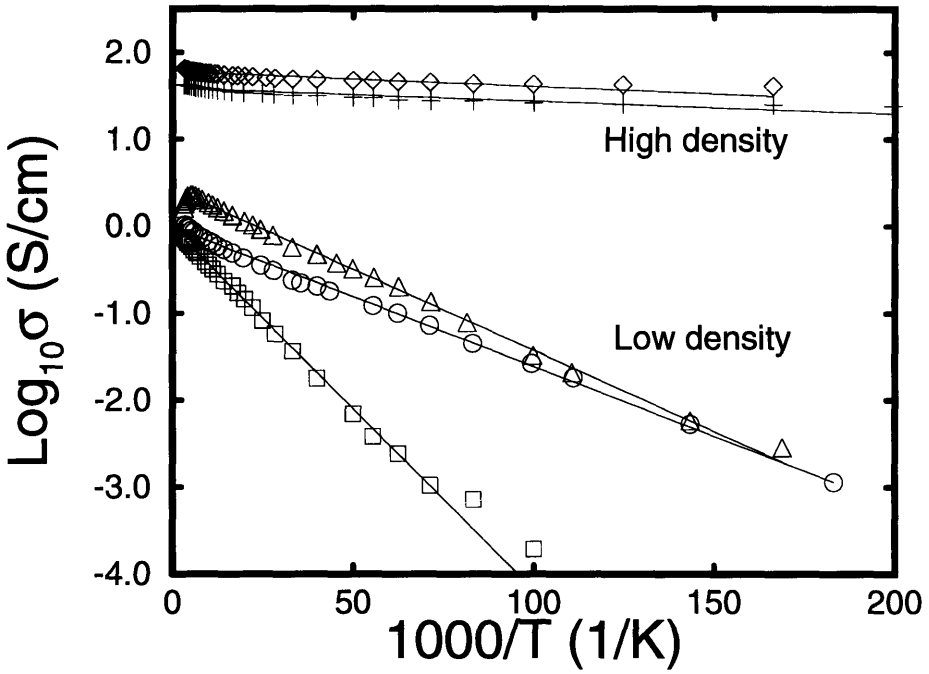

Figure 3-5: Semi-log plot of the conductivity as a function of 1000/T for the samples in Fig. 3-3. □:T_{HT}=1050° C, ρ_m = 0.103 g/cm^3; ○:T_{HT}=1500° C, ρ_m = 0.117 g/cm^3; △:T_{HT}=1800° C, ρ_m = 0.137 g/cm^3; +:T_{HT}=1500° C, ρ_m = 0.621 g/cm^3; ◇:T_{HT}=1800° C, ρ_m = 0.635 g/cm^3.

The data in Fig. 3-3 exhibit a linear relation over the temperature range T < 50 K, suggestive of a thermally activated conductivity, $\sigma(T) \propto \exp[-E_a/kT]$. It should be emphasized that this activated form for the conductivity is a limiting case of the type of variable range hopping to be discussed below.

Particle size effects

Figure 3-4 shows a semi-log plot of σ versus T for various particle sizes. The form of $\sigma(T)$ is similar to that in Figs. 3-2 and 3-3. However, the order of magnitude changes in σ at low temperature are more pronounced in Fig. 3-4. In particular, the low-density R/C=50 sample below 5 K has a resistance that falls off by six orders of

magnitude over a 1 K temperature range. Below 4 K, its resistance is on the order of gigaohms, making low temperature measurements on this sample very difficult. The behaviour of σ(T) for the low-density R/C=50 samples is similar to that of the low-density R/C=200 and 300 aerogels. However, the low-temperature conductivity for R/C=50 samples tends to be more strongly temperature-dependent than for the R/C=200 and 300 samples, for a fixed mass density. This behaviour is consistent with the polymeric carbon aerogels being a more mesoscopically disordered system.

Figure 3-6, a log-log plot of σ versus T, emphasizes the temperature dependence of σ(T) at low T. The observed behaviour at low temperature is once again indicative of a strongly localized system. In this sense, the electron's wavefunction is confined around a point r_0 in space. In this localization regime the carbon aerogel is no longer metallic, but exhibits insulating characteristics. Given the metallic and insulating behaviour of the aerogel system, we can expect varied temperature dependences of the conductivity, as will be seen below in the data analysis.

3.2.2 Temperature Dependence of σ

Features common to Fig. 3-2- 3-4 are i) an IMT transition between the high- and low-density samples, irrespective of R/C or T_{HT} ii) a strong temperature-dependence in the low density samples. The carbon aerogel, from TEM measurements, consists of a network of connected particles. Electrical transport should take place via i) motion of de-localized charge carriers within the particles and ii) hopping between particles to facilitate charge carrier transfer. By considering the particles to lie in an insulating matrix (air), they resemble Sheng's [38] model of carbon particles embedded in an insulating PVC matrix. There, Sheng used a model of fluctuation-induced tunneling (FIT) to explain the σ(T) mechanism. In the FIT model, it is assumed that thermally activated voltage fluctuations across the barrier between carbon particles drives the tunneling current of electrons through the potential barriers between carbon particles. In this vein, our previous analysis of the σ(T) data in Fig. 3-2 (effects

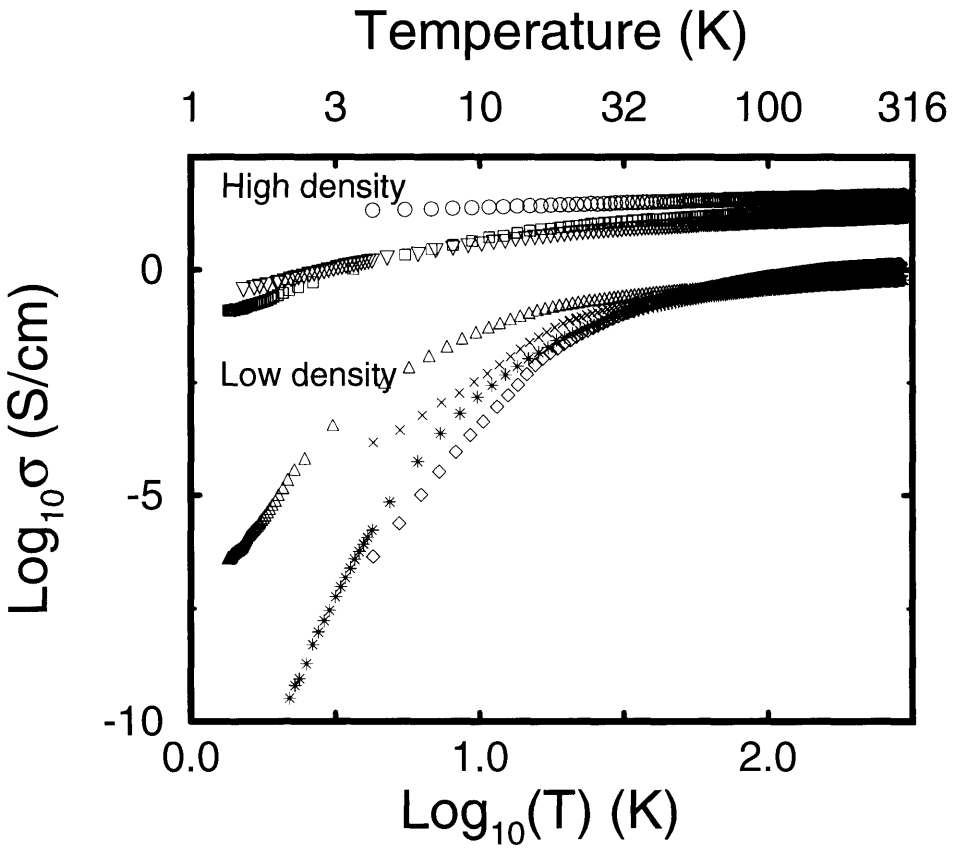

Figure 3-6: Showing a $\log_{10}$-$\log_{10}$ plot of σ versus T for the samples in Fig. 3-4, thereby emphasizing the low T behaviour. $\circ$: R/C=300, ρ_m=0.801 g/cm^3; $\square$:R/C=50, ρ_m=0.672 g/cm^3; $\triangledown$: R/C=200, ρ_m=0.670 g/cm^3; $\triangle$: R/C=300, ρ_m=0.117 g/cm^3; $*$: R/C=200, ρ_m=0.123 g/cm^3; $\diamond$: R/C=50, ρ_m=0.182 g/cm^3; $\times$: R/C=50, ρ_m=0.190 g/cm^3; T_{HT}=1800° C.

of ρ_m) was done using the FIT model. Recent findings show [39] that this model results in unreasonably large effective masses for the charge carriers ($\sim$ 40 m_e for the low-density sample). Recent findings also show that variable range hopping is a more likely conduction mechanism than FIT at very low temperatures (T < 10 K). Furthermore, $\sigma(T)$ measurements, made above 4.2 K, could not possibly distinguish between the thermally activated conduction and the FIT model (given by $\sigma(T) = \sigma_0 \exp\{-[T_1/(T+T_0)]\}$) when the observed values of T_0 are less than 4 K.

By performing conductivity measurements down to 1.2 K, the mechanism responsible for the localization at low temperature can be analyzed more thoroughly. With this in mind, Figs. 3-7(a)-(d) show semi-log plots of σ versus $(1/T)^p$ (where $p = 1, 1/2, 1/3, 1/4$) for the data in Fig. 3-4. The best linear fit to the data at low temperature is for $p = 1/2$. This gives a conductivity with a temperature dependence that follows $\exp(-\sqrt{T_0/T})$. The $p = 1/2$ dependence in Fig. 3-7(b) is universal for all the samples studied and is more pronounced at low temperatures (T < 10 K), especially for the low-density samples. The deviation in resistivity from a $p = 1/2$ to a $p = 1$ dependence at higher temperatures shows that at these temperatures, the carbon aerogel follows a simple activated form. The $p = 1/2$ dependence is suggestive of a Coulomb gap variable range hopping (CGVRH) [40] mechanism (see Sect. 3.4). In order to corroborate this identification of the transport mechanism, magnetoresistance studies have been conducted, the results of which are discussed in Sect. 3.3. There it will be shown that the CGVRH mechanism predicts a magnetoresistance which has a quadratic dependence on magnetic field.

Although no low-temperature (T < 4 K) data is available for the low-density R/C=50 heat-treated (T_{HT} =1800° C) sample, the transport mechanism associated with the $p = 1/2$ behaviour is likely to apply to this sample as well, since its conductivity follows a trend similar to that of the as-prepared low-density R/C=200 and 300 samples.

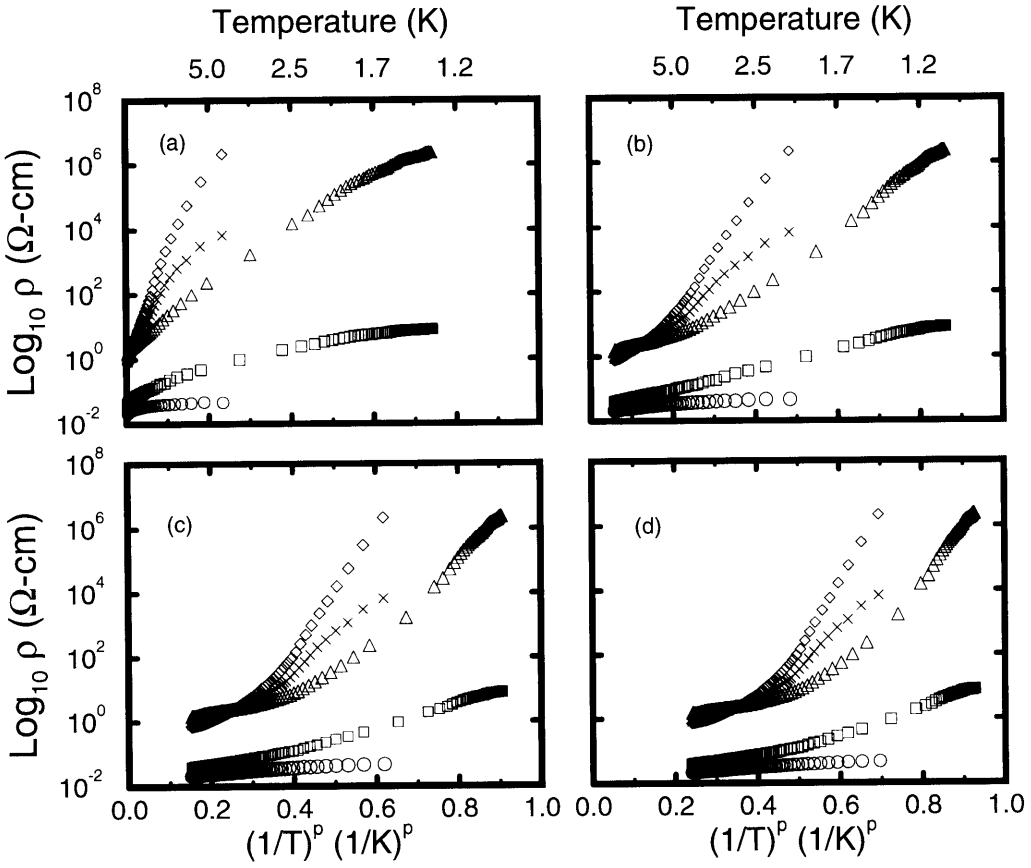

Figure 3-7: Semi-log plot of resistivity ρ versus $(1/T)^p$ for the (RF) carbon aerogels shown in Fig. 3-4. Labeling clockwise from the upper-left, p = (a) 1 (b) 1/2, (c) 1/3, (d) 1/4 for $\diamond$: R/C=50, ρ_m=0.182 g/cm^3; $\times$: R/C=50, ρ_m=0.190 g/cm^3; T_{HT}=1800° C; $\triangle$: R/C=300, ρ_m=0.117 g/cm^3; $\square$: R/C=50, ρ_m=0.672 g/cm^3; $\circ$: R/C=300, ρ_m=0.801 g/cm^3.

3.3 Experimental Results: Transverse Magnetoresistance

The transverse magnetoresistance was measured at temperatures ranging from 1.5 K to 27 K for the high-density R/C=50 and the low-density R/C=50 and 300 as-prepared samples. Figures 3-8(a)-(c) show the relative change in magnetoresistance $[\rho(H) - \rho(0)]/\rho(0) \equiv \Delta\rho/\rho$ as a function of magnetic field (H) for various values of measurement temperature for: (a) the low-density ($\rho_m = 0.117$ g/cm^3) R/C=300, (b) the low-density ($\rho_m = 0.182$ g/cm^3) R/C=50, and (c) the high-density ($\rho_m = 0.672$ g/cm^3) R/C=50 samples, respectively. The magnetoresistance for all the samples studied is positive and large in comparison to other disordered carbon materials [41]. Similar behaviour in $\Delta\rho/\rho$ as a function of field has been observed for the R/C=200 and the PF-based carbon aerogels. However, as the only available samples for these latter aerogels were high-density types (0.38 - 0.75 g/cm^3), their $\Delta\rho/\rho$ behaviour as a function of field is similar in magnitude to the high-density R/C=50 carbon aerogels (Fig. 3-8(c)), with $\Delta\rho/\rho$ being $\sim$ 20% at 15 Tesla for the PF-based aerogel with $\rho_m = 0.383$ g/cm^3. For all the samples studied, the magnetoresistance is temperature dependent, with the largest $\Delta\rho/\rho$ occurring at low temperature (T $<$ 4K).

In Fig. 3-9, in which $\Delta\rho/\rho$ is plotted versus H at 4.3 K for both high and low-density aerogels with various R/C molar ratios, we see that the low-density R/C=50 aerogel exhibits the largest $\Delta\rho/\rho$ (121% at 15T). This is consistent with the large temperature dependence of the resistivity exhibited by this sample at low temperature in the semi-log plot of $\sigma(T)$ versus T (see Fig. 3-4).

The transverse magnetoresistance follows a quadratic form at low fields as shown in Fig. 3-10, in which $\Delta\rho/\rho$ is plotted versus H^2 for the high-density R/C=50 sample in Fig. 3-8(b). This quadratic behaviour was observed in all of the samples studied and becomes suppressed (saturated) at high magnetic fields, with the saturation field

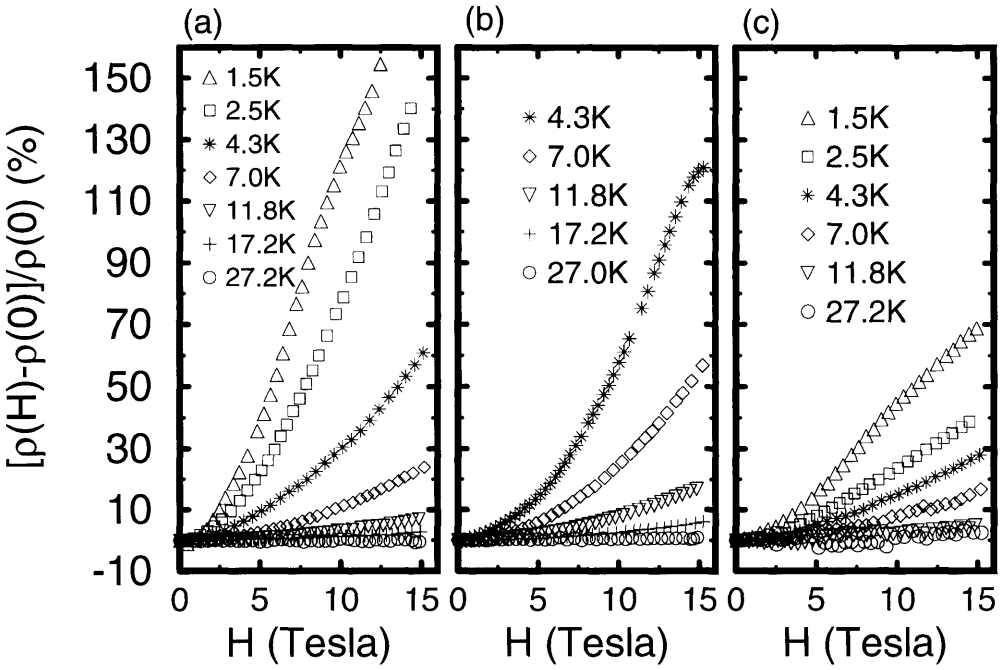

Figure 3-8: $[\rho(H) - \rho(0)/\rho(0)]$ versus H for carbon aerogels of (a) low density (ρ_m = 0.117 g/cc) and R/C=300, (b) low density (ρ_m = 0.182 g/cc) and R/C=50 and (c) high density (ρ_m = 0.672 g/cc) and R/C=50, at various measurement temperatures.

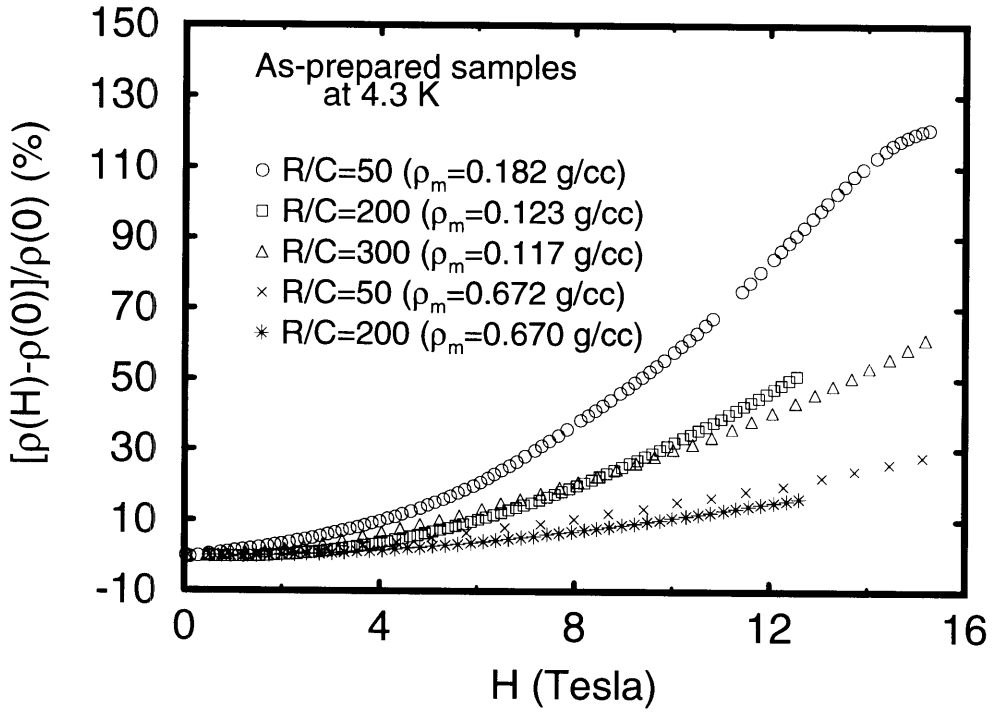

Figure 3-9: $[\rho(H) - \rho(0)/\rho(0)]$ versus H for carbon aerogel samples with different densities and R/C ratios at 4.3 K.

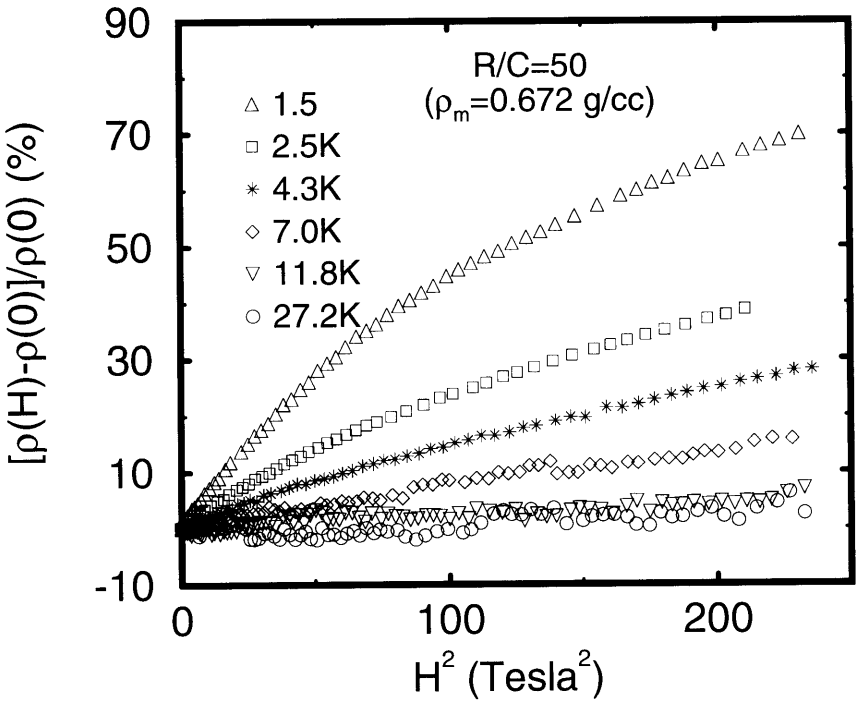

Figure 3-10: $[\rho(H) - \rho(0)/\rho(0)]$ versus H^2 for the R/C=50 sample with $\rho_m = 0.672$ g/cm^3.

decreasing with decreasing temperature. Further discussion of the temperature and magnetic field dependence of the magnetoresistance is given in Sect. 3.4.

3.4 Discussion of Transport in Carbon Aerogels

Fung *et al.* [39] have observed an exponential $p = 1/2$ temperature-dependence in the conductivity of R/C=200 colloidal carbon aerogels. This behaviour was attributed to variable range hopping (VRH) in a Coulomb gap in the density of states. The observance of a $p = 1/2$ dependence in the conductivity for the colloidal and polymeric carbon aerogels studied in Sec. 3.2.2 is also consistent with a Coulomb gap VRH mechanism. It is noted that the determination of the p-value by plotting $\log_{10}\sigma$ versus $(1/\mathrm{T})^p$ for different p values is somewhat ambiguous because of the finite temperature range for which the $(1/\mathrm{T})^{1/2}$ plot is linear. It is also possible that the observed $p = 1/2$ behaviour is not due to a CGVRH mechanism. Since the CGVRH model also predicts a unique temperature-dependence for the magnetoresistance, the conductivity findings in Sect. 3.2 can be confirmed by measuring the magnetoresistance as a function of temperature.

The presence of a positive magnetoresistance is suggestive of a hopping conductivity mechanism. The presence of the magnetic field in a VRH system is to cause a reduction in the wave function overlap, which in turn results in an increase in the tunneling probability and an increase in resistance. When a Coulomb gap is present in the density of states, the magnetoresistance in the VRH regime is given by [40]:

$$\ln\left[\frac{\rho(H)}{\rho(0)}\right] = t\left(\frac{\xi}{\lambda}\right)^4\left(\frac{T_0}{T}\right)^{3p} \equiv MH^2 \tag{3.4}$$

where $\lambda \equiv \sqrt{c\hbar/eH}$ is the magnetic length, ξ a localization length, $\mathrm{T_0}$ the same characteristic temperature as in Eqn. (3.7), $p = 1/2$ and t, a p-dependent term, is ~ 0.0015 for a 3-D system. Equation (3.4) is valid in the weak field regime, i.e., for

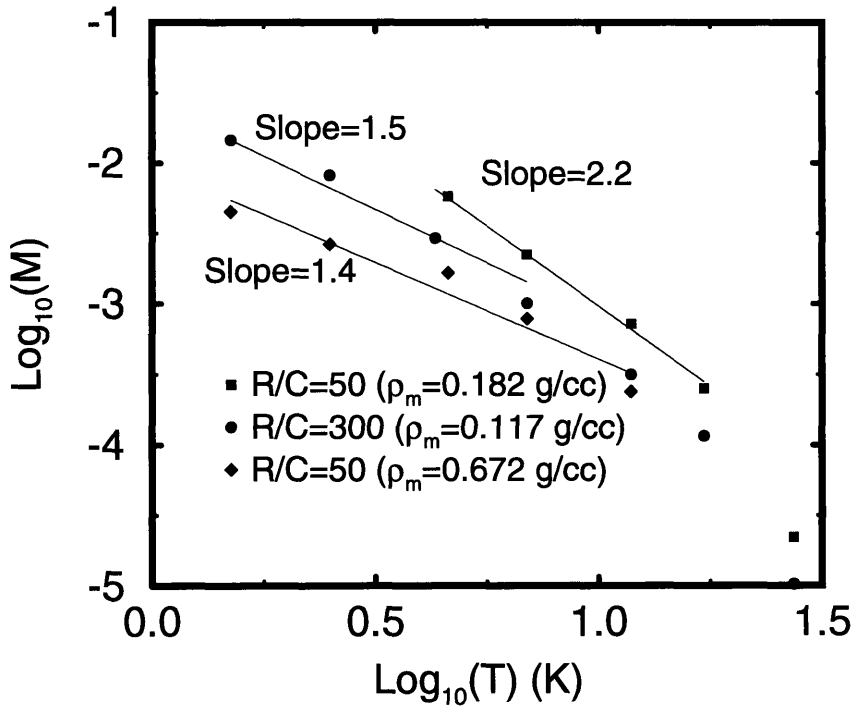

Figure 3-11: Log_{10}-log_{10} plot of slope, M, in Eqn. (3.4) versus T for three as-prepared carbon aerogel samples (see text). The slopes of the curves in this figure give the values of $3p$ in Eqn. (3.4).

$\lambda \gg \xi$. By fitting the low-field linear regime in a plot of $\ln[\rho(H)/\rho(0)]$ versus H^2, a value for M in Eqn. (3.4) as a function of T can be obtained. A log-log plot of M versus T is used to give the p dependence in Eqn. (3.4). Thus, an observed value of $p = 1/2$ would be consistent with both the observed conductivity and the CGVRH mechanism.

Figure 3-11 shows a log-log plot of slope M versus T for three measured aerogel samples. For both the high-density R/C=50 sample and the low-density R/C=300 sample, the data in Fig 3-11 show that $p \sim 0.5$. Since the magnetoresistance for the low-density R/C=50 sample could not be measured at very low temperatures, no good estimate for p could be obtained for this sample. The approximate value of $p = 0.7$ indicated by the four points in Fig. 3-11 for the R/C=50 ($\rho_m = 0.182$ g/cm^3)

sample is likely to be an overestimate of p for this sample, since the onset of the $\sqrt{1/T}$ behaviour occurs around 4 K for this sample. The value of $p = 1/2$ obtained from Fig. 3-11 confirms the value of p obtained from the plot of $\log_{10}\rho$ versus $1/\sqrt{T}$ in Fig. 3-7(b), and suggests that CGVRH is indeed possible at low temperatures in colloidal as well as polymeric aerogels. It is interesting to understand how VRH is possible in carbon aerogels with varied morphologies. This can be done by first reviewing how the CGVRH mechanism manifests itself in a disordered system and then adapting this mechanism to the carbon aerogel system.

In an amorphous system, as the temperature is lowered, the conduction mechanism is by hopping between states with energies lying close to the Fermi level. For a non-vanishing constant density of states at the Fermi level, the conductivity follows Mott's law [42]

$$\sigma = \sigma_0 \exp[-(T_0/T)^p] \tag{3.5}$$

with $p = 1/(n+1)$ for an n-dimensional system. The hopping distance is temperature-dependent, unlike the case of nearest-neighbour (NN) hopping; hence the Mott's law behaviour is referred to as variable range hopping conduction. When electron-electron interactions are taken into account, Efros and Shklovskii [40, 43] have shown that a quasi-gap appears in the density of states at the Fermi level, and that the resulting conductivity exhibits a Coulomb gap VRH (CGVRH) conduction mechanism given by:

$$\sigma = \sigma_0 \exp[-(T_0/T)^{1/2}] \tag{3.6}$$

where

$$T_0 = \frac{\beta e^2}{\kappa k_B \xi} \tag{3.7}$$

with κ being the dielectric constant, ξ the localization length, k_B Boltzmann's constant and $\beta = 2.8$ for a three-dimensional system [40]. This $p = 1/2$ dependence has been observed in both amorphous semiconductors [44] and granular metals [45] (GMs), although the origin of this dependence is not well established in the latter

system.

The GM material consists of metallic grains of some average size d randomly dispersed in an insulating matrix with an average separation s between the grains. The aerogel system is similar to the GM material in its structure of grains and pores. However, unlike the GM, the grains in the carbon aerogel system are necessarily closely connected in order to maintain the solid structure, resulting in a granular separation s much less than the grain size d.

Various studies have been done on the transport properties of GMs in order to explain the $p = 1/2$ dependence of the conductivity. Studies have shown that this dependence was possible under the assumption of s/d =constant [45, 46]. However, this assumption is not always experimentally verified in all systems, including carbon aerogels. For uncorrelated distributions of s and d (with $s \sim d$), the critical path method (CPM) [47, 48] results in an approximate $p = 1/2$ dependence in the intermediate regime between VRH and tunneling.

The idea of VRH in GMs has not been widely adopted since the electron wavefunction decays rapidly in the insulating gap between neighbouring grains. The study of Fung *et al.* [39] has addressed the issue of how VRH could occur in carbon aerogels with their connected-grain morphology. The grains and the insulating gaps between the grains can present barriers of height ϕ_d and ϕ_s, respectively. If the wavefunction decays rapidly across the gaps and $s \sim d$, then NN hopping should dominate over VRH because the probability of locating an electron beyond a NN grain decreases almost exponentially with distance. However, because of the fluctuations in the grain energy due to the surrounding random disorder potential (see below), the wavefunction decay over the grain could be larger than that between the grains, especially for $s \ll d$, as is the case for carbon aerogels. When an image force is taken into account, ϕ_s could be significantly lowered, further reducing the wavefunction decay in the gaps between neighbouring grains, leaving ϕ_d as the only effective means for carrier localization.

Adkins [49] proposed that fluctuations in the charging energy E_c of the grains are caused by a random disorder potential near each grain. The charging energy is defined as the energy required to move a charge from infinity onto a neutral conducting grain and is given by:

$$E_c \sim \frac{e^2}{\kappa d} \tag{3.8}$$

where e is the charge, κ the effective dielectric constant of the medium through which the charge is moving, and d the size of the grain. As E_c can only change in the presence of the random disorder potential by an amount of $2E_c$ without discharging, the energy of the system as a whole varies between $E_F \pm 2E_c$, where E_F is the Fermi energy. The average effective barrier height ϕ_d is then on the order of the fluctuations of E_c, i.e.,

$$\phi_d \sim 2E_c \ . \tag{3.9}$$

With the introduction of the fluctuations in the grain energy, the localization length ξ can be replaced with an effective wavefunction decay length (χ_{eff}^{-1}) within the grain, given as a function of the effective barrier height ϕ_d,

$$\chi_{eff} = \sqrt{\frac{2m^*\phi_d}{\hbar^2}} \tag{3.10}$$

in which m* is the effective mass of the carriers.

From the above discussion, the finite grain size does not prevent one from observing VRH in the Coulomb gap regime. From the $p = 1/2$ dependences in the magnetoresistance and the conductivity data, the CGVRH mechanism, as previously applied to explain the low-temperature conduction in carbon aerogel samples with R/C=200, is seen to be retained, despite changes in grain size ranging from $\sim 70 - 150$ Å.

Table 3.4 lists values of T_0, κ, χ_{eff}^{-1} and m* as obtained from the CGVRH model. These values were obtained from experiment as follows. A fit of the conductivity curves to Eqn. (3.6) resulted in values of T_0. The curves were fit in a temperature

Table 3.4: Coulomb gap variable range hopping (CGVRH) parameters for as-prepared carbon aerogels with various R/C molar ratios and densities. Values for the characteristic temperature T_0, the dielectric constant κ, particle sizes d, wavefunction decay lengths $\chi_{\rm eff}^{-1}$ and the effective mass, m* are shown.

R/C	50	50	200	200	300
Density(g/cm^3)	0.182	0.672	0.123	0.670	0.117
T_{HT}(° C)	1050	1050	1050	1050	1050
T_0 (K)	1849	45	2100	30	502
κ	6.5	105.4	6	110	16.6
d (Å)	70-90	70-90 (70)[a]	(120)	(120)	150(160)
χ_{eff}^{-1} (Å)	39	99	35	140	56
m* (units of m_e)	0.04-0.05	0.10-0.13	0.08	0.09	0.10

[a] Grain sizes in parentheses based on m*=0.1 m_e

range corresponding to an onset of $\sqrt{1/T}$ behaviour at low temperature. The T_0 values were then used along with values of the slope M [from Eqn. (3.4)] to obtain χ_{eff}. The values for κ were then obtained from Eqn. (3.7) and used, along with χ_{eff}, to procure values of m* from Eqn. (3.10). The lack of low-temperature data for the low-density as-prepared R/C=50 sample resulted in an underestimation of T_0, and hence the unphysically small values of m* in Table 3.4. Since the grain size d is not uniform within the aerogels of R/C=50 and 300, a range of possible values for m* results, as shown in Table 3.4. Previous work [39] done on R/C=200 aerogels has shown that an average effective mass of $m^* \simeq 0.1m_0$ has consistently resulted in reasonable grain sizes. Using this value of m^* results in the grain sizes listed in parentheses in Table 3.4. These grain sizes, as obtained from the CGVRH model, are consistent with the average grain sizes measured with high-resolution TEM [11].

Table 3.4 suggests that the wavefunction decay length (χ_{eff}^{-1}) is correlated with the mass density. The high-density samples have larger χ_{eff}^{-1} than the low-density samples, in accordance with the closer packing of the grains and hence the observed increase in κ. Increases in κ signify a reduction in the spread of the charging energy as the IMT

is reached. T_0 gives a measure of this energy spread and decreases accordingly with increases in ρ_m. The hopping distance, given approximately by $\chi_{eff}^{-1}(T_0/T)^{1/2}$, can be estimated and compared with the grain sizes obtained using an effective mass of 0.1 m_e. From Fig. 3-7(b), the $\sqrt{1/T}$ dependence is valid for T < 20 K and T < 16 K for the high-density R/C=50 and the low-density R/C=300 aerogels, respectively. Using values for T_0 and χ_{eff}^{-1} from Table 3.4, minimum hopping distances of 136 Å and 315 Å are obtained for the R/C=50 and 300 samples, respectively. These distances are approximately two times the average grain sizes, suggesting that not only is VRH possible, but that the grains, and not the dangling bonds, act as localization sites. The number of carriers localized to these sites can be estimated from the photoconductivity data (see Sect. 4.4). There it is shown that the hole carrier density, p_0, is on the order of 10^{17} carriers/cm^3. For a particle of diameter 120 Å, this implies that each particle is occupied by only one electron for a one-to-one relation of electrons and holes in the system, thereby implying large fluctuations in local electron density. The strong localization at low temperatures exhibited by the low-density carbon aerogels suggests that these aerogels obey the condition $k_F l < 1$, where l is the mean free path of the conduction carriers. As the particles themselves act as the localization sites, the mean free paths are on the order of the particle sizes (70 - 150Å). A rough estimate of the values of k_F for carbon aerogels compared to that of graphite can be obtained using $k_F = (3\pi^2 n)^{1/3}$ where n is the carrier density. For graphite, $n \sim 10^{19}$ carriers/cm^3, so that $k_{\text{Faerogels}} \sim 0.2\ k_{\text{Fgraphite}}$, since the Fermi surfaces for the carbon aerogels are smaller than those for graphite.

3.5 Relation Between Microscopic Disorder and Electrical Conductivity

Despite the smearing of the grains in R/C=50 samples, the magnitude of L_a from Raman studies (see Table 2.4) suggests that the structure internal to a grain in carbon aerogels is independent of both the R/C ratio and the mass density. The magnitude of L_a is in good agreement with the size of the RF filaments within the grains, as observed by high-resolution TEM [50]. With heat-treatment, L_a increases slightly and the microscopic disorder in the system also becomes annealed somewhat, both as shown by the Raman scattering measurements in Chapter 2.

The specific surface area increases with decreasing R/C, and this manifests itself in a large concentration of unpaired spins (as denoted by N), as can be seen from the values of N in Table 2.7. It is noted that the increase in the specific surface areas (SSAs) from R/C=300 to 50, quoted in Sect. 2.1 from results of gas adsorption measurements, could not account for the much larger increase in N, probably because part of the actual SSA is inaccessible to the vapour used in the adsorption measurement. However, the increase in N can be explained by the SSA increase calculated from the average grain sizes listed in parentheses in Table 3.4, suggesting that the grain size calculated from the CGVRH model is indeed correct, and that the SSA available for charge storage might be more accurately measured by transport and capacitance measurements than by adsorption methods.

There is no clear correlation between the spin concentration and the conductivity. For example, in Table 2.7, the number of unpaired spins per gram for the low-density heat-treated (T_{HT} =1800° C) R/C=50 aerogel, which also exhibits a strong localization behaviour (see Sec. 3.2.1), is smaller than that of the high-density as-prepared R/C=50 aerogel. From Fig. 3-7(b), the high-density as-prepared R/C=50 sample has a larger conductivity (smaller resistivity) than the low-density heat-treated R/C=50 sample, seemingly suggesting that the conductivity increases with increasing micro-

scopic disorder. However, by comparing the low-density as-prepared and heat-treated R/C=50 aerogels, it is observed that the conductivity seemingly decreases with increasing microscopic disorder. This suggests that the low temperature conduction mechanism is more related to the density than to the unpaired spin concentration, since with increasing density, there is always an increase in the conductivity. Since the density is correlated with the packing ratio of the grains, it is likely that the grains, rather than the defects, act as the carrier localization sites in the CGVRH process.

For the low-density R/C=200 and R/C=300 as-prepared samples, although the mass density and the unpaired spin concentration in both systems are similar (i.e., equal microscopic disorder), their conductivities are very different. The only variable is the grain size. Once again, the unpaired spins do not correlate with the observed conductivities, thus further supporting the CGVRH model in which the grains are the localization sites and the grain size (i.e., the granularity or mesoscopic disorder) is an important parameter in determining the sample resistance.

The colloidal and polymeric aerogels not only differ in grain size but also in the distinction of individual grains. Despite the morphological differences, the transport experiments suggest that colloidal and polymeric aerogels exhibit similar transport behaviour. This tends to suggest that polymeric and colloidal aerogels do not represent two structural extremes, as also pointed out in a previous high-resolution TEM study [11]. The synthesis process for both types of aerogels should follow similar pathways, except that under high catalyst concentrations, the process of cluster (grain) formation is short-lived because RF chains are quickly being connected to other RF chains nearby, resulting in smaller grain sizes in the polymeric carbon aerogels. Though obscured in a high-resolution TEM micrograph by the presence of highly branched carbon filaments, these small grains should constitute the insulated conducting regions (and localization sites for charge carriers) in polymeric aerogels, as suggested by the transport results.

Finally, it is worth mentioning that the structural links between neighbouring grains are not necessarily electrically conducting. As such, more non-conducting regions (defects) would be expected in polymeric carbon aerogels, leading to lower electrical conductivity at a given density as compared to colloidal carbon aerogels. These data are nevertheless consistent with the superior mechanical properties of polymeric carbon aerogels since the nonconducting defects can support mechanical loads [51].

Chapter 4

Photoconductivity In Carbon Aerogels

The carbon aerogel represents a disordered carbon system. In Chapter 3 it was shown that there was not a very strong correlation between the microscopic disorder and the electrical conductivity. The conductivity is strongly dependent on the mesoscopic disorder (packing of the particles). Chapter 4 focuses on the role the microscopic defects play in the carbon aerogel system by using photoconductivity as a probe. A few concepts of photoconductivity are presented. The experimental set-up as it pertains to the types of measurements (time and power dependences, for example) being done are examined. Finally, the results and a model for the photoconductivity are presented.

4.1 Demarcation levels, Recombination Centres and Traps

When light is incident on a material, (photo-excited) electron-hole pairs can be created which can then go on to enhance the electrical conductivity. This increase in the number of charge carriers due to the incident radiation is called photoconductivity

($\Delta\sigma$). The effect is more pronounced in an insulator in which the thermal dark carrier density (n_0, p_0) is less than the photo-generated carrier density ($\Delta n, \Delta p$). If both carriers contribute to the increased conduction, then

$$\Delta\sigma = e(\Delta n\mu_n + \Delta p\mu_p) \ , \tag{4.1}$$

where e is the electron charge and $\mu_{n,p}$ are the electron and hole mobilities, respectively. The absorbed photon energy can excite photoelectrons to the conduction band in a variety of ways:

i) Direct band-to-band transitions

ii) Donor level ionization

iii) Impurity level (located in the valence band) to conduction band transitions.

Photo-electrons excited to the conduction band via light excitation will generally recombine with free holes indirectly, through defects in the material. Defects can act as either recombination centres or traps for the photo-carriers. Recombination centres differ from traps only in terms of their location with respect to the demarcation level (defined below). Figure 4-1 shows the differences between the two types of centres. The diagram shows an electron and a hole sitting at the demarcation level, D. In the steady-state, the demarcation level is the energy level at which a hole (electron) has equal probability of being thermally excited to the valence (conduction) band or being able to capture a free electron (hole). Referring to Fig. 4-1, energy levels above D (levels closer to the conduction band, CB), act as traps for electrons as it is easier to thermally excite the electron to the conduction band from this point. These same levels act as recombination centres for holes as it is easier to capture an electron into these levels and thus release the hole into the valence band. It should be noted that recombination is a two-step process, whereas trapping is a one-step process.

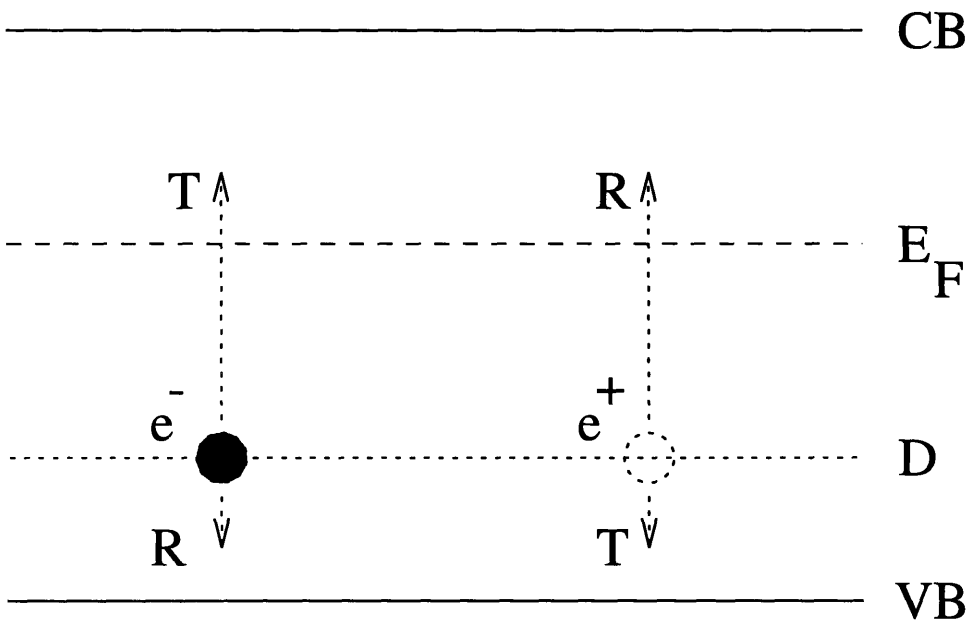

Figure 4-1: Schematic diagram showing the general definition of demarcation levels (D), recombination (R) and trapping (T) centres. The conduction and valence bands are denoted by CB and VB, respectively, while E_F is the Fermi energy.

4.1.1 Monomolecular and Bimolecular Recombination

Recombination can take place in a variety of ways. If the photo-carrier density is smaller than that of the thermal dark carriers ($\Delta\sigma < \sigma$), then recombination occurs with thermal dark carriers. This type of recombination is known as a monomolecular process. If, however, the photo-carrier density is larger than that of the thermal dark carriers, the photo-carriers have a larger probability of recombining with each other, independent of the dark carriers. This results in a bimolecular process [52].

Both types of processes result in the photocurrent Δi having a dependence on the incident light intensity, I. For the monomolecular case, $\Delta i \propto I$, while the bimolecular process has $\Delta i \propto I^{1/2}$. By doing power-dependence studies, the type of recombination mechanism inherent to the aerogel system can be examined.

The time the photo-carrier spends contributing to the photoconductivity is considered its lifetime. This lifetime can be short (on the order of microseconds) or long (persistent photoconductivity - on the order of days). Another measure of time is the response time. This is defined as the time for the photocurrent to reach 1/e of its steady-state value after the light is turned on (rise time) or off (decay time). The presence of traps can be observed in the decay time profiles. When the light is turned off, for the system to relax to equilibrium, the recombination centres will capture electrons, say, but any traps in the system will have to empty electrons into the recombination centres by first exciting electrons thermally into the conduction band. In this way, the response time in the absence of light, can be longer than the response time in the presence of light.

4.2 Experimental Setup

The photoconductivity measurements consisted of three parts: Measuring (a) the temperature-dependent photoconductivity, (b) the intensity dependence and (c) the transient (time-dependent) photoconductivity. The various electronics required for

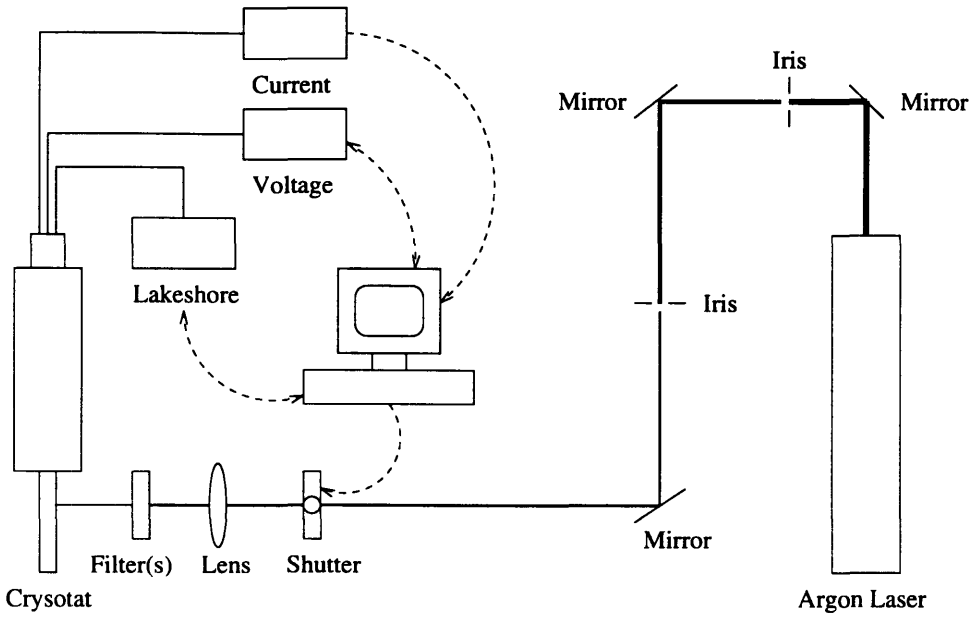

Figure 4-2: Schematic showing the overall experimental set-up for the photoconductivity experiments. The sample is connected to external instruments via electrical feedthroughs from the cryostat. The computer is connected to the Lakeshore temperature controller, the shutter and the voltage and current meters. The arrows on the dashed lines show the flow of information. The width of the laser lines in the diagram signifies a reduction in the laser diameter/focusing.

these measurements are described in this section.

The illuminating source is an Argon-ion laser, of wavelength 4880 Å. The general photoconductivity set-up also consists of an optics table, an IBM compatible 486 DX computer, an automated shutter control system, a Lakeshore DRC-93CA temperature controller and a Keithley current source and voltmeter. The computer has software which is used to create programs for remotely controlling the Lakeshore, the shutter and the programmable Keithley voltmeter. Figure 4-2 gives an overall schematic of the experimental set-up. Various parts of the experiment are described in more detail below.

Samples are mounted as discussed in Section 3.4. The samples are then placed in a Janis continuous flow optical cryostat, the schematic of which is shown in Fig. 4-3.

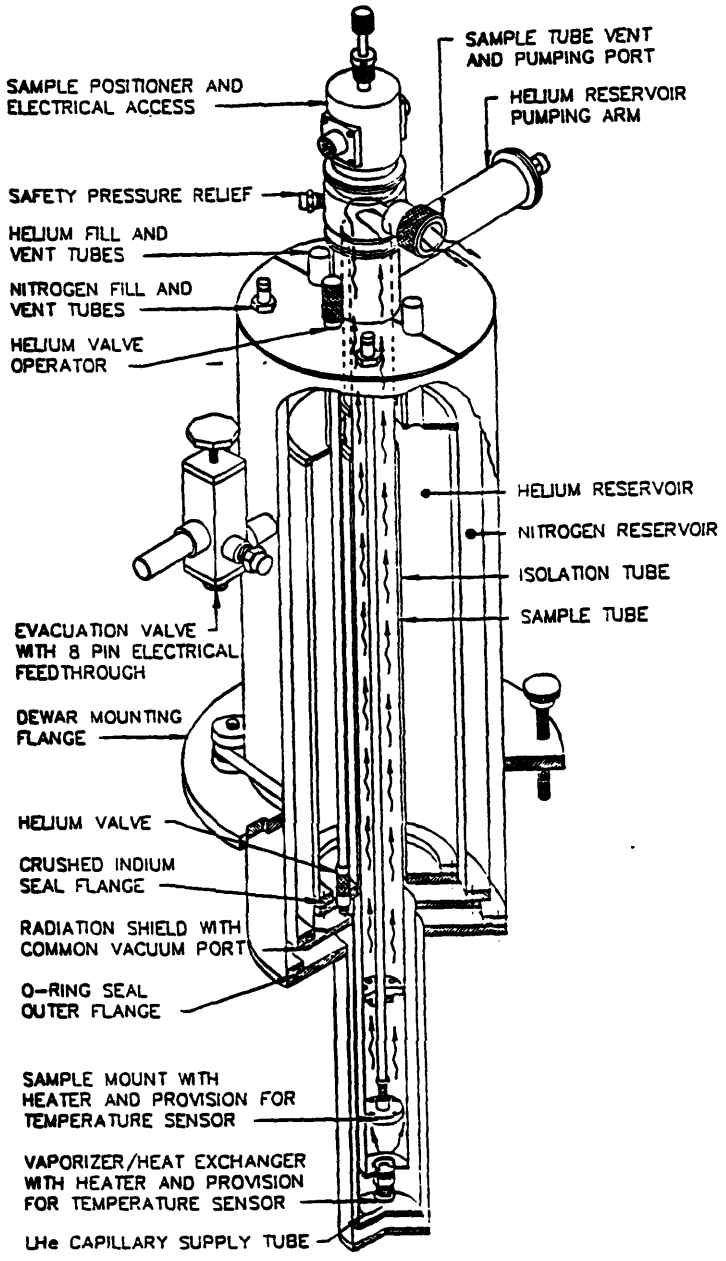

Figure 4-3: Schematic showing the optical cryostat used for the photoconductivity experiments. The main features are the needle valve control for allowing the Helium to enter the sample space for sample cooling and the sample space with its vapourizer/temperature sensor for control of the Helium temperature.

The cryostat consists of an outer jacket which is kept evacuated and acts as a thermos. An outer Nitrogen reservoir is used for thermal cooling of the liquid Helium in the inner jacket. The sample space is thermally connected to the Helium reservoir via the Helium valve operator (needle valve). The other end of the needle valve opens into a liquid Helium capillary supply tube. Liquid Helium can enter the sample space through this tube. However, the presence of a vapourizer (heater) and a temperature sensor are responsible for controlling the temperature of the gas going into the sample space. By using the Lakeshore and the temperature sensor to control the heat supplied to the vapourizer, the temperature of the gas flowing over the sample, and hence the sample temperature, can be controlled from 4.2 K to 300 K. Another temperature sensor mounted near the sample provides the Lakeshore with the present sample temperature.

The optical setup consists of mirrors, irises, filters and focusing lenses. The primary goal of the optics is to focus the beam into a 1-2 mm spot size onto the sample. The irises are used to pick out the central part of the beam. The filter(s) is (are) used to adjust the laser power intensity reaching the sample surface.

For the time and power-dependence studies, a Uniblitz shutter is used. The shutter system is automated, as shown in the electronic schematic in Fig. 4-4. The computer consists of a DAQ PC-LM-16 I/O board (National Instruments) capable of providing digital output voltages up to ± 10 V with a maximum current output of 4 mA. The shutter needs a minimum of 5 V for operation. However, as the coils in the shutter require a larger current than is available on the board, an amplification system had to be employed. A 1 V digital output (V_i) was amplified to 5.5 V (V_o). The operational amplifier (op-amp) requires a ± 15 V supply, and this is where most of the current for the shutter comes from. After amplification, the output was passed through an oscilloscope for visual confirmation before being sent to the shutter. The computer program was written such that the shutter could be opened and closed for any period of time, automatically.

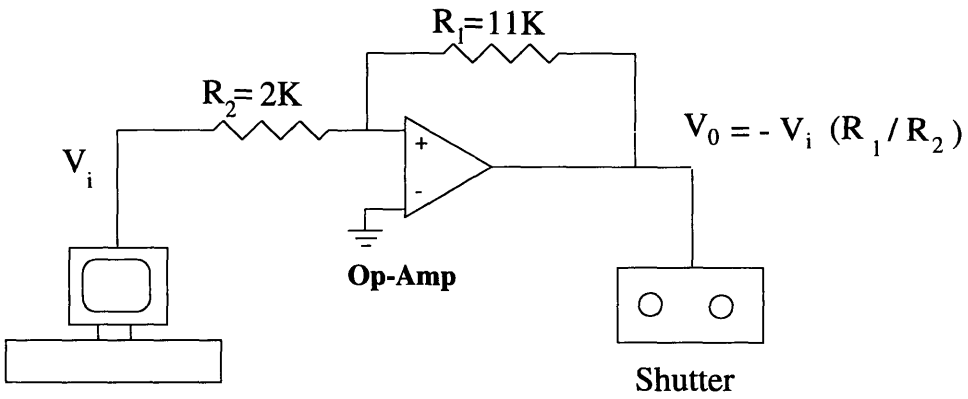

Figure 4-4: Schematic for the shutter control. The op-amp is used to amplify the voltage output (V_i) from the board on the computer. The amplification factor for the output voltage (V_0) is given by the ratio of resistors R_1 and R_2.

To conduct a time-dependent measurement, the shutter open/close times are set such that the photo-signal comes to an equilibrium value. A Keithley 182 programmable voltmeter is used to store the data in its buffer. Once the data are collected into the buffer, it is extracted using another computer program which saves the measured photo-voltage as a function of time.

4.3 Results

Figure 4-5 shows a semi-log plot of photoconductivity versus temperature [1] for three colloidal (R/C=200) carbon aerogel samples with various mass densities. One interesting feature in the photoconductivity data is the occurrence of a maximum in the plots of $\Delta\sigma$ versus T. The photoconductivity follows a simple activated form, $\Delta\sigma \propto \exp[-T_0/T]$ at low T and $\Delta\sigma \propto \exp[T_1/T]$ at high T. The temperature where the photoconductivity is maximum, denoted by $T_{\max}$, occurs at approximately the same temperature where the dark conductivity falls off sharply (recall Fig. 3-2) into its

[1] Unlike the dark-conductivity measurements, the photoconductivity measurements are taken above 4.2 K.

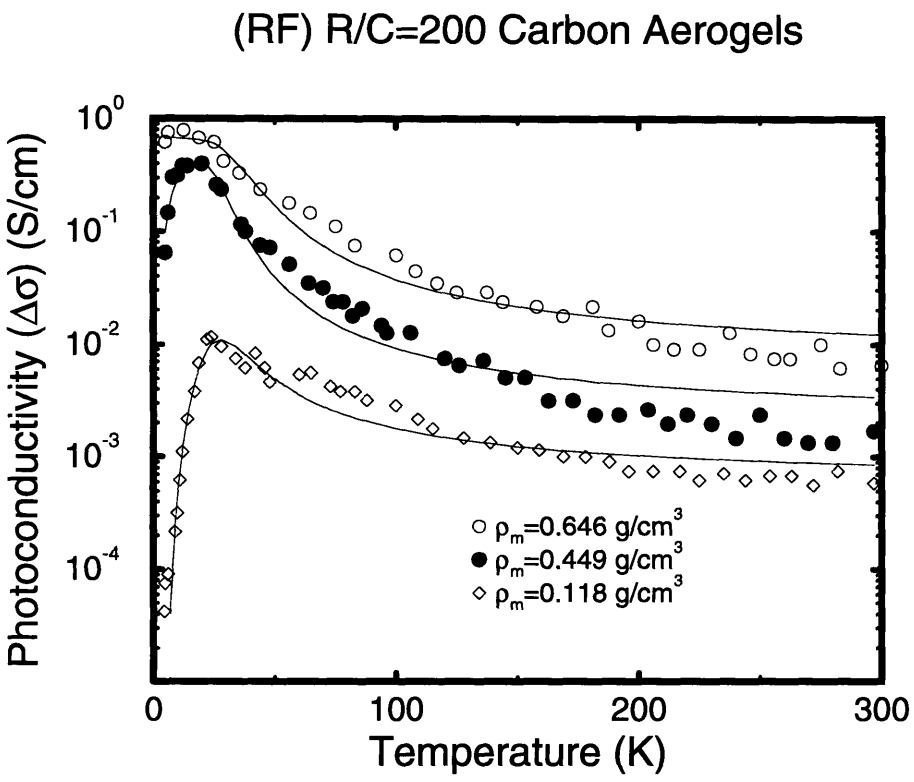

Figure 4-5: Semi-log plot of photoconductivity $\Delta\sigma$ versus temperature for R/C=200 as-prepared carbon aerogels with various densities. Solid lines show the results of a least-squares fit obtained using Eqn. (4.17). These data are the photoconductivity values for the samples whose dark conductivity was given in Fig. 3-2: $\circ$: ρ_m = 0.646 g/cm^3; $\bullet$: ρ_m = 0.449 g/cm^3; $\diamond$: ρ_m = 0.118 g/cm^3.

localized regime. This suggests that the photoconductivity mechanism at low temperatures is limited by a process similar to the transport and that the mobility is thermally activated. On the high-temperature side of T_{max}, the photoconductivity decreases and is smaller in magnitude than $\sigma(T)$. This decrease in photoconductivity suggests that recombination is occurring with thermal dark carriers that are generated with increasing temperature.

Fig. 4-6 shows the photoconductivity, $\Delta\sigma$, for as-prepared carbon aerogels with different heat-treatment temperatures plotted as a function of measurement temperature, T. Again there is the presence of a peak in $\Delta\sigma(T)$. As T_{HT} is increased,

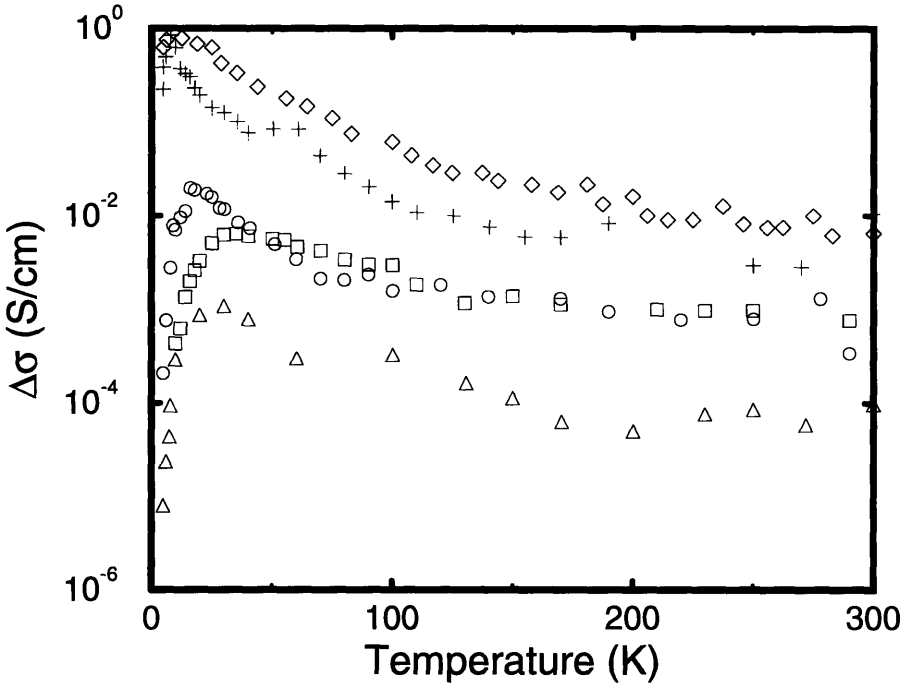

Figure 4-6: Semi-log plot of photoconductivity $\Delta\sigma$ versus temperature for R/C=200 carbon aerogels with various heat-treatment temperatures. These data are the photoconductivity values for the samples whose dark conductivity was given in Fig. 3-3. $\diamond$:T_{HT} = 1050° C, ρ_m = 0.646 g/cm^3; + :T_{HT} = 1500° C, ρ_m = 0.621 g/cm^3; $\square$:T_{HT} = 1050° C, ρ_m = 0.103 g/cm^3; $\circ$:T_{HT} = 1500° C, ρ_m = 0.117 g/cm^3; $\triangle$:T_{HT} = 1800° C, ρ_m = 0.137 g/cm^3.

T_{max} moves to lower temperatures, tracking the behaviour of the dark conductivity. The onset of localization at low temperatures becomes suppressed with an increase in heat-treatment. An increase in density (from the low to high density regime) results in an overall increase in the magnitude of the photoconductivity.

Similar to the data in Fig. 4-5, the slope of $\Delta\sigma$ versus T on the low-temperature side of T_{max} is larger than that on the high-temperature side. No photoconductivity signal could be detected for the high-density sample (ρ_m=0.635 g/cm^3) with T_{HT}=1800° C, although the high-density sample with T_{HT}=1500° C and the high-density as-prepared sample (ρ_m=0.646 g/cm^3) in Fig. 4-5 do exhibit a measurable pho-

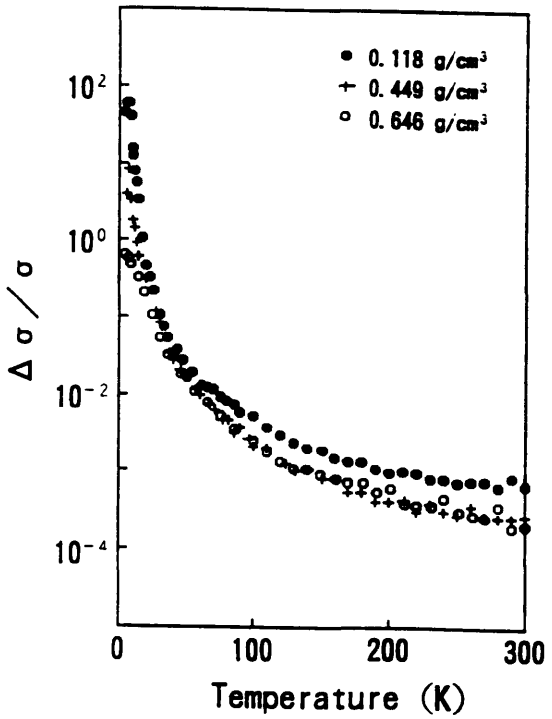

Figure 4-7: Semi-log plot of $\Delta\sigma/\sigma$ versus T for the colloidal carbon aerogel data in Figs. 3-2 and 4-5. • : $\rho_m = 0.118$ g/cm^3; + : $\rho_m = 0.449$ g/cm^3; ○ : $\rho_m = 0.646$ g/cm^3.

toconductivity. The large photoconductivity value for the high-density heat-treated sample ($\rho_m = 0.621$ g/cm^3, $T_{\rm HT}$=1500° C) can be understood by noting that the dark conductivity is very large for this sample, signifying a mobility greater than that for the low-density aerogels. Since $\Delta\sigma \propto \mu$, the magnitude of the photoconductivity should also scale as the mobility, conforming to the experimental data.

To further investigate the properties of the photoconductivity, Figs. 4-7 and 4-8 show semi-log plots of $\Delta\sigma/\sigma$ versus T for the data in Figs. 4-5 and 4-6, respectively. Both plots show a monotonic decrease in $\Delta\sigma/\sigma$ with increasing T and no maximum in $\Delta\sigma/\sigma$ is observed, in contrast to the behaviour of $\Delta\sigma$(T) itself. For the density dependence in Fig. 4-7, the ratio $\Delta\sigma/\sigma$ for the two least dense samples would seem to imply that there are few free carriers present in the as-prepared carbon aerogel system. However, the AC measurements [2] of $\Delta\sigma$ show a much faster drop in the

[2]Not shown here, but discussed in [37].

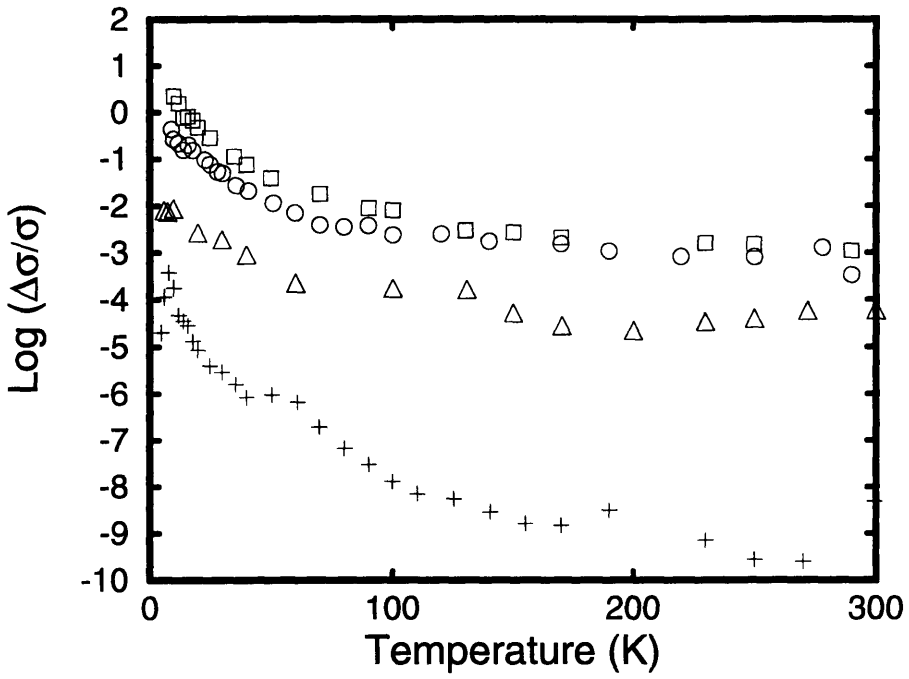

Figure 4-8: Semi-log plot of $\Delta\sigma/\sigma$ versus T for the data in Figs. 3-3 and 4-6. □ :T_{HT} = 1050° C, $\rho_m = 0.103$ g/cm^3; ○ :T_{HT} = 1500° C, $\rho_m = 0.117$ g/cm^3; △ :T_{HT} = 1800° C, $\rho_m = 0.137$ g/cm^3; + :T_{HT} = 1500° C, $\rho_m = 0.621$ g/cm^3.

magnitude of $\Delta\sigma/\sigma$ with increasing T than the DC data (by 2 orders of magnitude). The DC data represent changes in both p and Δp, whereas the AC data, where a gate time shorter than the recombination time is employed, represent changes only in p while Δp effectively remains constant. Hence, the AC data really imply that $\Delta\sigma/\sigma < 1$, and hence the presence of free carriers. The presence of free carriers signifies that the recombination should occur via a monomolecular process, as will be seen later in the power-dependence study. With increases in ρ_m the reduction in $\Delta\sigma/\sigma$ signals an increase in the speed with which recombination occurs. This increase in recombination is also manifested in the response times' dependence on density (see Fig. 4-12). As will be shown in the model below, the number of traps in the system, and the energy associated with these traps, is reduced with an increase in ρ_m.

Figure 4-8 shows that not only is there a decrease in $\Delta\sigma/\sigma$ with increases in ρ_m, but also there is a decrease with increasing T_{HT} at all temperatures. The compounded effects of increases in T_{HT} and ρ_m can be seen in the high-density sample heat-treated to 1500° C. Here, the recombination process is purely monomolecular in nature with the recombination process increasing with increases in heat-treatment temperature.

Figures 4-9 and 4-10 show the plots of photoconductivity versus laser intensity for the various samples shown in Figs. 4-5 and 4-6. The data were taken at low (10 K) temperature (Figs. 4-9 and 4-10) and at room temperature (Fig. 4-9). For Fig. 4-9, there is evidence of a variety of recombination processes. However, at 300 K, the process is strictly monomolecular in nature. At 10 K, in contrast, there is evidence for monomolecular recombination at low light intensities. With increases in intensity, this behaviour crosses over to the bimolecular regime. In essence, with increases in light intensity, states that were traps can become recombination centres. As the density of recombination centres increases, the carrier lifetime will decrease. This is the definition for a power dependence less than unity [53]. Referring now to the data in Fig. 4-10 (taken at 10 K), it is seen that there is only evidence for bimolecular recombination for all intensities studied, implying the presence of free carriers even

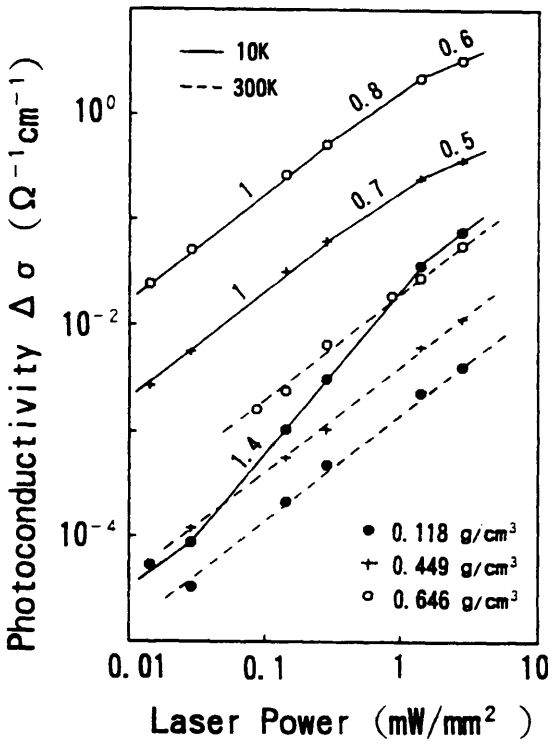

Figure 4-9: Plot of photoconductivity ($\Delta\sigma$) versus laser power for the data in Fig. 4-6. There is evidence of monomolecular processes at 300 K (dashed lines) for all light intensities. At low temperature (solid lines) and high light intensities, the data show the existence of bimolecular recombination. • : $\rho_m = 0.118$ g/cm^3; + : $\rho_m = 0.449$ g/cm^3; ○ : $\rho_m = 0.646$ g/cm^3.

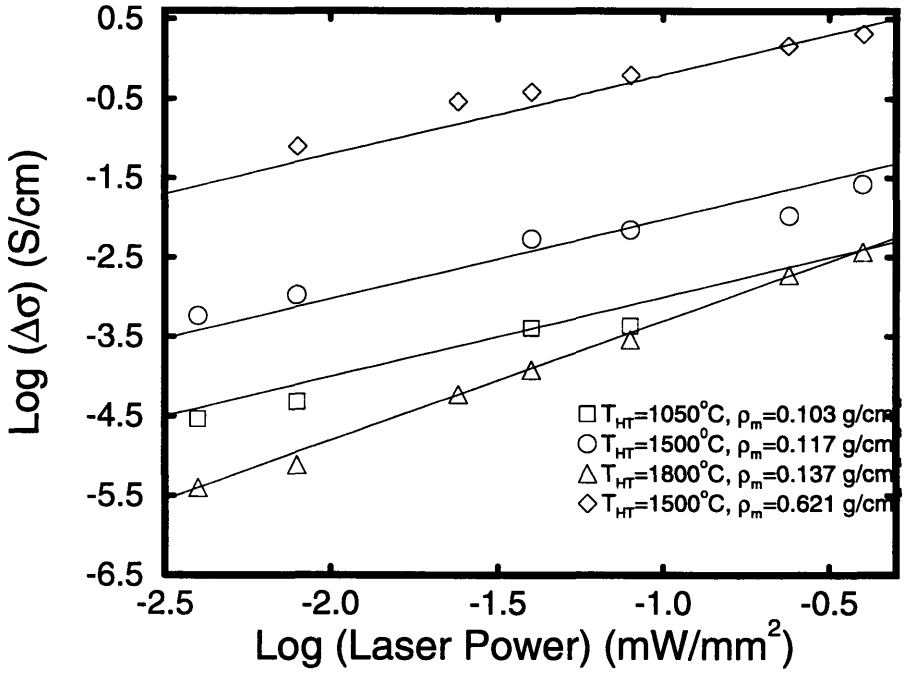

Figure 4-10: Log-log plot of photoconductivity measured at 10K versus laser intensity for carbon aerogel samples with various mass densities ρ_m and heat-treatment temperatures T_{HT}. The data points are compared to solid lines with a slope of 1 for three of the data sets. For the $\triangle$ sample with $T_{\rm HT}$ = 1800° C and ρ_m=0.137 g/cm^3, the comparison is to a slope of 1.5. $\square$:$T_{\rm HT}$ = 1050° C, ρ_m = 0.103 g/cm^3; $\circ$:$T_{\rm HT}$ = 1500° C, ρ_m = 0.117 g/cm^3; $\triangle$:$T_{\rm HT}$ = 1800° C, ρ_m = 0.137 g/cm^3; + :$T_{\rm HT}$ = 1500° C, ρ_m = 0.621 g/cm^3.

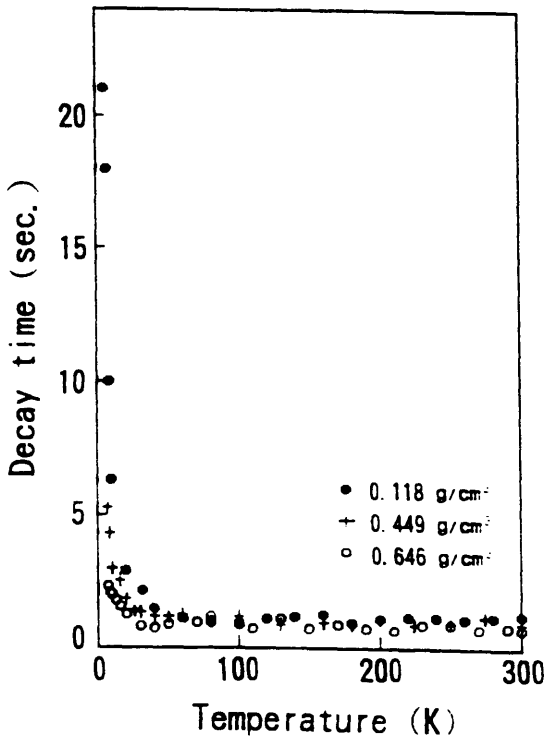

Figure 4-11: Plot of decay time versus temperature for R/C=200 carbon aerogels: • : $\rho_m = 0.118$ g/cm^3; + : $\rho_m = 0.449$ g/cm^3; ○ : $\rho_m = 0.646$ g/cm^3.

at low temperatures.

Figure 4-11 shows the decay times for the aerogels with various densities as a function of temperature. The observed behaviour is typical of the samples studied. The decay times are very long at low temperature and subsequently decrease with increases in temperature. There is a rapid fall-off in decay times for T > 10 K. This coincides with the increases in the recombination rate as discussed earlier. In Fig. 4-11, the least dense sample exhibits the longest decay times at low temperatures. The density effects on decay times are also shown in Fig. 4-12, a plot of ρ_m versus decay time at 10 K and 300 K. With increases in density, the decay time is seen to decrease. Although the decay times at 10 K seem only slightly longer than the times at 300 K, it must be noted that the low-temperature decay times fall off very rapidly above 6 K. The long decay times that occur will be discussed below and are attributed to a possible screening of trapped carriers.

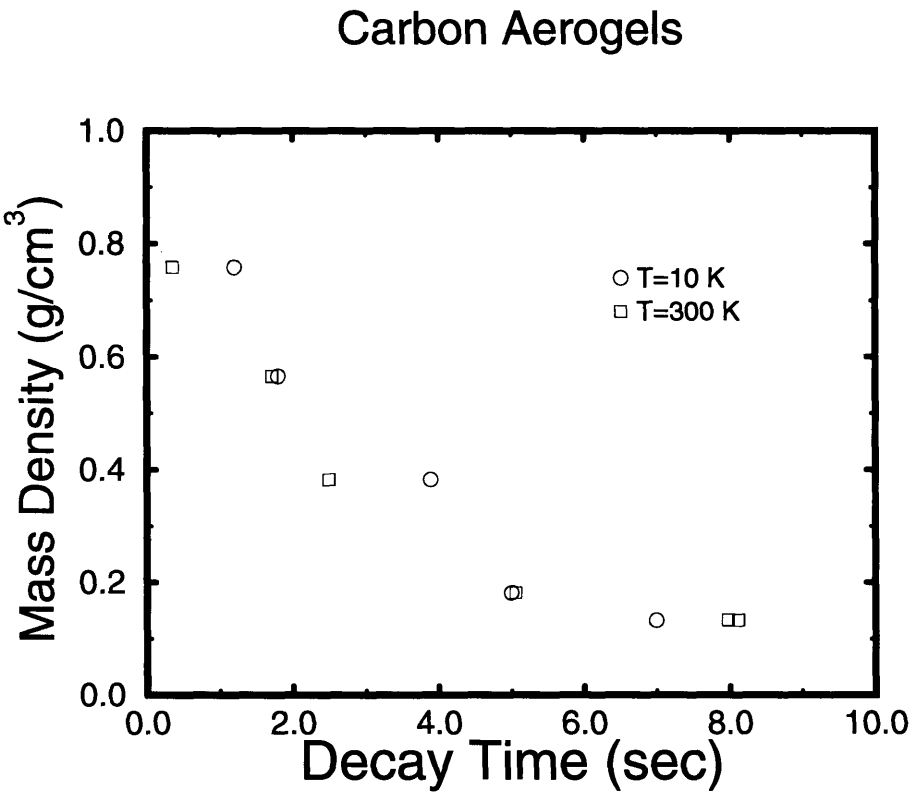

Figure 4-12: Plot of density versus decay time for colloidal carbon aerogels at 10 K and 300 K.

4.4 Model for Photoconductivity

In order to understand the behaviour of the photoconductivity of carbon aerogels, it is instructive to recall the results of the dark conductivity data in Chapter 3. The thermal activation form of the conductivity at low temperature, $\sigma(T) \propto \exp[-E_a/kT]$, suggests nearest-neighbor hopping as the dominant conduction mechanism in carbon aerogels (a limiting case of the variable range hopping observed from magnetoresistance data at very low T (<10K)). As we know, the aerogel system has a 'string-of-pearls' morphology with graphitic ribbons within the particles. Charge carriers are delocalized within the particles and transport takes between particles via a CGVRH mechanism. The ribbons within the particles are stacks of well-formed graphene platelets with a width of $\sim$ 25 Å as deduced from the Raman scattering experiments. Theoretical calculations [54, 55] have shown that for a graphite sheet with finite size, there exists a band gap E_g determined by the size of the platelet (W) according to

$$E_g = \frac{21}{W} \tag{4.2}$$

where E_g is in electron-volts and W is in Å. For a ribbon of width 25 Å, Eqn. (4.2) suggests a bandgap $E_g \sim$ 1eV, which is much larger than the experimentally measured values of E_a, which are on the order of a few meV. Thus, the temperature dependent behaviour of σ cannot be attributed to the thermal activation of charge carriers across this band gap. Hence, this thermal activation behaviour is attributed to hopping between nearest-neighbor grains (particles) which now become localization sites.

With these mechanisms in mind for the conductivity and photoconductivity, Fig. 4-13 illustrates schematically the density-of-states model being considered. Energies are measured as indicated by the arrow in the diagram. Typically, disordered carbon materials tend to be p-type [56], resulting in a Fermi energy, E_F, situated in the valence band. The conduction and valence band mobility edges are denoted by E_C and E_V, respectively. Localized states (shaded regions) exist below E_C and above E_V, while

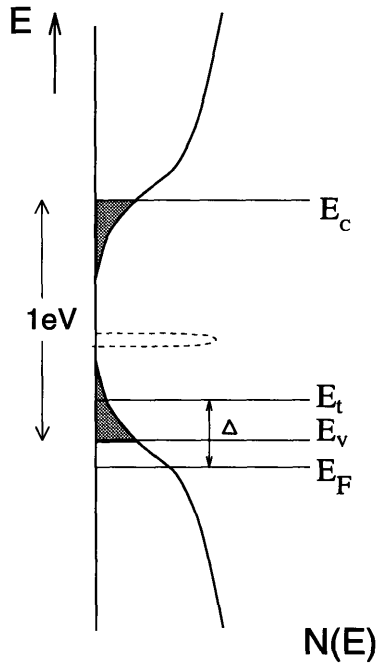

Figure 4-13: Schematic diagram showing a physical form of the density-of-states used to explain the observed photoconductivity data. E_v and E_c define the mobility edges for the conduction and valence bands, respectively, while E_F denotes the Fermi energy level. Two kinds of trap distributions are considered; i) An exponential distribution (shaded region) and ii) A delta-like function (dashed region) near the valence band. Δ defines E_t-E_F, where E_t is the energy of the trapping level.

quasi-continuum states exist above E_C and below E_V. The quasi-continuum states result from the spatial confinement introduced by the quantum size of the particles. Free carriers exist between E_F and E_V. With this model, photoexcited carriers can get trapped in localized states above E_V. To account for the long decay times that are observed, screening of the trapped carriers induced by lattice relaxation would have to occur.

To link the above model to the photoconductivity data, a mathematical model is proposed to quantitatively explain the observed T-dependence of the photoconductivity. As stated earlier, the prominent features of the temperature dependence of the photoconductivity include a maximum in the plots of $\Delta\sigma$ versus temperature. Above

and below this maximum, the photoconductivity exhibits an exponential temperature dependence. These similar features have been observed in various chalcogenide glasses such as a-As_2Te_3 and $Ge_{15}Te_{81}Sb_2S_2$ [57, 58, 59]. The goal of the model is to elucidate the essence of the photoprocesses in carbon aerogels from which important information about the effects of heat treatment and density on the defect properties of these materials can be extracted.

To pinpoint the recombination process in the aerogel system, a degenerate p-type semiconductor, it is informative to locate the demarcation levels, and from these determine whether the defects present behave as traps or recombination centres for free carriers.

The hole demarcation level, E_{Dp}, can be found from the definition given in Section 4.1 by equating the probability of capturing an excited electron into a trap ($\bar{n}$) to the probability of thermally exciting (emitting) a hole from this same trap level (e_p) to the valence band, E_V. Hence,

$$\bar{n} \equiv n\sigma_n v = e_p \ . \tag{4.3}$$

Here, σ_n is the capture cross section for electrons, $n = n_0 + \Delta n$ is the electron density in the steady-state, n_0 is the electron density in thermal equilibrium, $v = v_n = v_p$ is the electron (hole) velocity and e_p is the probability for thermal emission of holes from the trapping level. The hole emission rate e_p can be found from detailed balance considerations in thermal equilibrium [60]. For detailed balance, the rate of emission of holes equals the rate of capture of holes.

$$e_p N_t(1 - f) = \bar{p} N_t f \tag{4.4}$$

with f being the trap occupancy function, N_t the density of the trapping level and

$\bar{p} \equiv p\sigma_p v$ with similar definitions as given above for electrons. Hence, we obtain

$$e_p = v\sigma_p p_0 \exp[-(E_{Dp} - E_F)/kT])] \tag{4.5}$$

for a trap state at the demarcation level E_{Dp} and p_0 is the hole density in thermal equilibrium ($p_0 >> \Delta p$ in the degenerate semiconductor case). From Eqns. (4.3) and (4.5), the demarcation level for holes is given by:

$$E_{Dp} - E_F = kTln(\frac{\sigma_p p_0}{\sigma_n \Delta n}) \ . \tag{4.6}$$

Similar calculations for the electron demarcation level E_{Dn} give:

$$E_{Dn} - E_F = kTln(\frac{\sigma_p p_0}{\sigma_n n_0}) \ , \tag{4.7}$$

using $\bar{p} = p_0\sigma_p v$ in thermal equilibrium and $e_n = n_0 v\sigma_n \exp[(E_{Dn} - E_F)/kT]$. In both cases the demarcation level is located at kT's above E_F (since $p_0/\Delta n, p_0/n_0 >> 1$). Hence, any defect states lying close to the valence band edge act as recombination centres for electrons, and traps for holes; as can be seen later, the defect states in carbon aerogels lie close to E_V. Photoconductivity can then be attributed to the photo-holes. Photo-electrons falling into the recombination centres are not likely to get re-excited because of the large bandgap and they only recombine when holes fall into the same traps. Recombination is not instantaneous as the electrons are effectively screened by lattice relaxation when they become trapped, thus accounting for the long decay times. Also, holes excited to traps of the same energy may not necessarily recombine with the trapped electrons, as their spatial locations can be different.

The next step is to find the photoconductivity itself. Consider a single trapping level of density, N_t. The time rate of change of the carrier density in the valence band will depend on i) the external electron-hole pair generation rate, G, ii) whether

a trap is full or empty and iii) the amount of direct recombination of electrons and holes across the gap (denoted by βpn). Hence, we obtain

$$\frac{dp}{dt} = G - \bar{p}N_t f_t + N_t e_p(1 - f_t) - \beta pn \tag{4.8}$$

where f_t is the occupancy function of the trapping level and $\bar{p} = (p_0 + \Delta p)\sigma_p v$. The direct recombination term is negligible since most excited electrons become trapped and so do not contribute to direct recombination. A similar equation holds for the conduction electrons:

$$\frac{dn}{dt} = G - \bar{n}N_t(1 - f_t) + N_t e_n f_t - \beta pn \ . \tag{4.9}$$

The steady-state trap occupancy function f_t can be found by subtracting Eqns. (4.8) and (4.9) and applying the steady-state conditions, $dn/dt = 0$ and $dp/dt = 0$. Hence,

$$f_t = \frac{\bar{n} + e_p}{\bar{n} + \bar{p} + e_n + e_p} \ . \tag{4.10}$$

By taking into account the condition of charge neutrality in the system (i.e., accounting for all the photo-electrons and photo-holes generated), Δp can be found. For charge neutrality, consider the creation of photo–electron-hole pairs. For the model being proposed, some of the photo-electrons become caught in the recombination centres (trapping centres for holes). The total photo-generated charges have to be accounted for as follows. The total photo-holes in the valence band equals the photo-electrons in the conduction band, minus the photo-electrons in the traps, plus the electrons already contributing to the trap occupancy (steady-state). So

$$\Delta p = \Delta n - N_t f_{ot} + N_t f_t \tag{4.11}$$

and

$$\Delta p - \Delta n = N_t[\frac{\bar{n} + e_p}{\bar{n} + e_n + \bar{p} + e_p} - \frac{e_p}{e_p + \bar{p}_0}] \tag{4.12}$$

where the right-hand side corresponds to the steady-state trap occupancy (f_t) minus the thermal equilibrium trap occupancy for electrons (f_{0t}). This latter term is obtained from the thermal equilibrium condition of equating the emission rate to the capture rate $[e_p/(e_p + \bar{p}_0) = 1/\{1 + \exp[(E_t - E_F)/kT]\}$ with $\bar{p}_0 = p_0\sigma_p v$ in thermal equilibrium]. Because the hole emission from traps close to E_V is large, and since $p_0 >> \Delta p$, we can assume $e_p >> (\Delta p\sigma_p + \Delta n\sigma_n)v$, or equivalently,

$$\frac{\Delta n\sigma_n + \Delta p\sigma_p}{\sigma_p p_0 \exp[-(E_t - E_F)/kT]} << 1 \ . \tag{4.13}$$

Using a Taylor series expansion to the first order on Eqn. (4.13), we obtain

$$\Delta p - \Delta n = N_t[\frac{\bar{n}}{\bar{p}_0 + e_p} - \frac{(\bar{n} + e_p)(\Delta n\sigma_n v + \Delta p\sigma_p v)}{(\bar{p}_0 + e_p)^2}] \ . \tag{4.14}$$

Because most of the photo-electrons become trapped and do not get re-excited to the conduction band, we can consider $\Delta n << \Delta p$. Using this assumption and $\bar{n} << e_p$ from above, we obtain, after collecting terms in Δp,

$$\Delta p \simeq \frac{(N_t \Delta n\sigma_n/p_0\sigma_p)}{\{1 + (2 + \frac{N_t}{p_0})\exp[-(E_t - E_F)/kT] + \exp[-2(E_t - E_F)/kT]\}} \ . \tag{4.15}$$

Using the fact that from the dark conductivity, $\mu \propto \exp(-E_A/kT)$ to a good approximation, we obtain

$$\Delta\sigma = \Delta pe\mu \propto \frac{N_t e(\Delta n\sigma_n/p_0\sigma_p)\exp(\frac{-E_A}{kT})}{1 + (2 + \frac{N_t}{p_0})\exp(\frac{-(E_t - E_F)}{kT})} \tag{4.16}$$

$$\propto \frac{A\exp(\frac{-E_A}{kT})}{1 + B\exp(\frac{-\Delta}{kT})} \tag{4.17}$$

where the term in $\exp[-2\Delta/kT]$ is ignored because it is much less than the $(2 + \frac{N_t}{p_0})\exp(-\Delta/kT)$ term, as is shown in the fits. The data were fit using a least-squares method.

Table 4.1: Showing the photoconductivity parameters for colloidal carbon aerogels of varied densities as obtained by fitting the data to Eqn. (4.17). The values for N_t are obtained from the susceptibility data. The trapping energy (Δ) and the parameter B are given.

R/C	200			
Heat-treatment Temperature (° C)	1050			
Density(g/cm^3)	0.103	0.118	0.449	0.646
Conductivity E_a (meV)	8.23	3.37	1.21	0.86
Photoconductivity ($\Delta\sigma$) $T_{\max}$ (K)	40.2	24.0	20.0	12.5
$\Delta\sigma$ activation energy E_A (meV)	3.3	5.9	0.87	0.92
$\Delta \equiv (E_t - E_F)$ (meV)	16.8	13.1	11.1	10.6
$B \equiv \frac{N_t}{p_0}$	37	281	163	47
N_t (/cm^3)	10^{20}	2×10^{19}	3×10^{19}	2×10^{19}
p_0 (/cm^3)	3×10^{18}	7×10^{16}	2×10^{17}	4×10^{17}

The fitting values of E_A for the photoconductivity (see Tables 4.1 and 4.2) are on the same order of magnitude as the activation energies E_a obtained from the dark conductivity data, confirming the self-consistency of the model. Values for B, N_t and p_0 are listed in Tables 4.1 and 4.2. The free carrier density, p_0, does not seem to decrease as much with increases in ρ_m as it does with increases with T_{HT}. There it is seen in Table 4.2 that the decrease in the trapping density with increasing heat-treatment temperature shows up as a corresponding decrease in p_0. Mrozowski [56] has shown that with increases in heat-treatment temperature (from 1000° C to $\sim$ 2500° C), the Fermi level starts to slowly move from out of the valence band towards the band gap. Hence, a decrease in the number of free carriers that lie between the valence band mobility edge and the Fermi level would be expected with increases in T_{HT}. For low values of p_0, the model is still valid as the assumption of $p_0 >> \Delta p$ holds in the high temperature regime where the effect of the term in $1/(1+B\exp(-\Delta/kT))$ begins to dominate in Eqn. (4.17) and the thermal generation of holes becomes prominent.

So far, consideration has been given to a system consisting of one kind of defect,

Table 4.2: Showing the photoconductivity parameters for colloidal carbon aerogels of varied heat-treatment temperatures as obtained by fitting the data to Eqn. (4.17). The values for N_t are obtained from the susceptibility data. The trapping energy (Δ) and the parameter B are given.

Heat-treatment Temperature (° C)	1500° C	1500° C	1800° C
Density(g/cm^3)	0.117	0.621	0.137
R/C		200	
Conductivity E_a (meV)	3.18	0.143	3.63
Photoconductivity ($\Delta\sigma$) $T_{\max}$ (K)	18.0	8.0	30.1
$\Delta\sigma$ activation energy E_A (meV)	2.2	0.67	2.4
$\Delta \equiv (E_t - E_F)$ (meV)	10.3	4.31	13.7
$B \equiv \frac{N_t}{p_0}$	120	100	73
N_t (/cm^3)	3×10^{19}	10^{19}	10^{19}
p_0 (/cm^3)	2×10^{17}	10^{17}	10^{17}

resulting in a single trapping level in the band gap. If the defect states are considered to be a result of dangling bonds situated near the valence band (dashed region in Fig. 4-13), then from Tables 4.1 and 4.2, the trapping energy, $\Delta \equiv (E_t - E_F)$, is seen generally to decrease with increasing $T_{\rm HT}$ and ρ_m. The decrease in Δ with increasing $T_{\rm HT}$ is due to the system becoming less disordered, effectively pushing E_F closer towards E_V.

If the energy levels associated with the dangling bonds are situated close to mid-gap, the observed values of Δ are too small to account for the deep position of the dangling bond energies. In that case, there is still justification for using a single energy level. We can go from an exponential distribution of localized states above E_V, as in Fig. 4-13, to a delta-function-like distribution for the trapping levels in the gap as follows. According to Tiedje and Rose [61], the density of states, $N(E)$, above E_V is exponential in nature. Hence $N(E)$ can be written in the form of

$$N(E) \propto \exp\{-[E - (E_V + E_p)]/E_W\} \ . \tag{4.18}$$

The localized states above E_V can be considered as having a characteristic width of

energy E_W. As $E_W \rightarrow 0$, $N(E) \rightarrow E_W\ \delta\{E - (E_V + E_p)\}$. The lowering of the tail state energies by the value E_p is attributed to polaron formation, which is common in disordered systems in which lattice distortions are favoured by the presence of vacancies and defects. The energy of the polarons formed in the tail states is given by:

$$E_p = \frac{E_1^2}{2Ka^3} \tag{4.19}$$

where E_1 is the deformation potential, K is the bulk modulus and a^3 is the deformation volume [62]. For $(E_V - E_F) \sim 1$ meV (a typical value for disordered carbons) and using $\Delta = E_p + (E_V - E_F)$, for an in-plane deformation potential [63] on the order of 28 eV and an in-plane bulk modulus [64] on the order of 10^{13} dynes/cm^2, the values listed for Δ would result in lengths on the order of 17 Å for the effective lattice distortion, which is reasonable for the widths of the carbon ribbons being considered. As heat-treatment temperatures and mass density increase, the reduced values of E_p imply larger bulk moduli.

4.5 Photoconductivity in Polymeric Carbon Aerogels

The polymeric carbon aerogels exhibit a photoconductivity behaviour that is different from that in colloidal carbon aerogels. At temperatures below 5 K, a steep increase in the photoconductivity $\Delta\sigma$ is observed, as shown in Fig. 4-14 for both the low- and high-density samples. At temperatures below the peak photoconductivity (T_{max}), $\Delta\sigma$ is very small. As the temperature increases to T_{max}, the photoconductivity rises rapidly to its maximal value. For the high-density sample, for temperatures above T_{max}, the photoconductivity falls off exponentially in a manner similar to that observed in the colloidal carbon aerogels (see Fig. 4-5). However, as the fall-off for the polymeric carbon aerogels is sharper than previously observed for the colloidal carbon

aerogels, the mathematical model as it stands does not fit this regime very well.

The most disordered (mesoscopically) polymeric aerogel, with $\rho_m = 0.182$ g/cm^3, exhibits a photoconductivity smaller in magnitude than its high-density counterpart, a trend that has already been observed in Section 4.3. There is also the presence of a maximal value of $\Delta\sigma$. However, the fall-off at higher temperatures is so extreme that now there is a very small amount of photoconductivity at temperatures above T_{max}.

The difference in the general form of $\Delta\sigma(T)$ for the low and high-density polymeric carbon aergeols should stem from the differences in disorder exhibited by these two samples. In particular, the low-density sample exhibits a conductivity at low temperatures (< 6 K) that decreases over 6 orders of magnitude, as compared to the high-sample which only falls off about 1 to 2 orders of magnitude in this same temperature range. One assumption of the photoconductivity model is that the behaviour of $\Delta\sigma$ at temperatures less than T_{max} follows that of the dark-conductivity. In this vein, the sharp increase in $\Delta\sigma$ as T_{max} is approached from below is a response to the localized behaviour exhibited by these samples. In general, the photoconductivity observed in polymeric carbon aerogels cannot be explained by Eqn. (4.17). The reasons for this failure of the model are discussed below.

From the studies done in Chapters 2 and 3, the polymeric aerogels, when compared to colloidal aerogels, tend to have stronger localization behaviour at low temperature, larger magnetoresistances and a larger concentration of unpaired spins. There are a few possible reasons for the breakdown of the photoconductivity model in the polymeric aerogels:

i) Increases in disorder can manifest themself as an increase in the density of defect states in the band gap. These defects play an important role in the recombination process, as has been shown with the colloidal aerogels. Once photo-holes and photo-electrons are created, the photo-electrons can fall into the recombination centres. The mobility of the photo-holes is limited at low temperatures, as there is not enough thermal energy to cause tunneling between sites. At T_{max} there is enough thermal

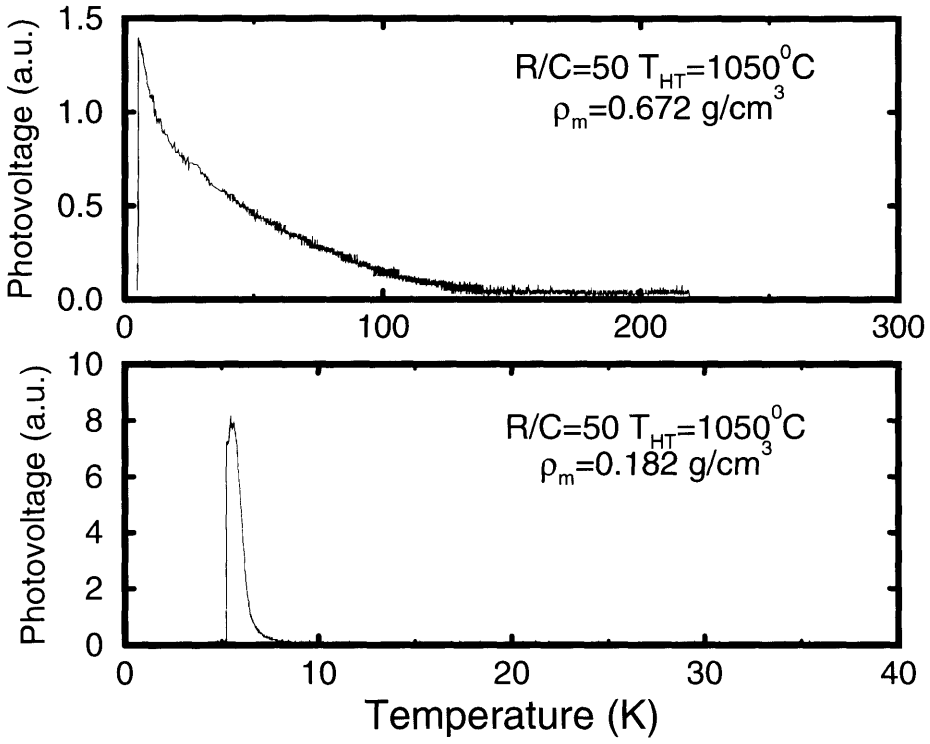

Figure 4-14: Showing the general features of the photoconductivity exhibited by polymeric carbon aerogels.

energy for tunneling to occur and hence the photo-holes can contribute to the photoconduction process. Increases in temperature also increase the probability of the recombination process, hence the decay in $\Delta\sigma$ at higher temperatures.

ii) If the photon energy is not sufficient to cause the photo-electron and photo-hole to drift far enough away from each other, then germinate recombination [65] can occur. Germinate recombination comes about when a photo–electron-hole pair attract each other. The attraction is Coulombic in nature and results in no photoconductivity. As thermal energies increase, this Coulomb attraction is reduced and the electron-hole pair can contribute to the photoconductivity.

Chapter 5

Conclusions

5.1 Summary

- i) The Raman spectroscopy measurements show that the carbon aerogel, PF and RF-based, have similar structure. In particular, the structure consists of particles of dimension 70 Å - 150 Å. For polymeric carbon aerogels, the particles are non-uniform in shape. The particles are connected via internal graphitic ribbons as well as by physical contact with each other. The connections between particles and thus the transport properties can be improved by heat-treatment or mass density increases. The former tends to enhance the formation of a graphitic structure within the particles.

- ii) The TEM analysis has proven useful in confirming results of Raman and SAXS studies. By using a unique image analysis technique, the structure of the mesopores (2 - 50 nm) could be observed. The fractal dimension was also calculated from this technique. For mesopores, polymeric (RF) carbon aerogels tend to have a more regular geometry than the colloidal (RF) carbon aerogels. Preliminary results on the nanopore structure ($<$ 2 nm) within the particles shows that polymeric and colloidal carbon aerogels have similar fractal dimensions. This confirms the results of the Raman studies that show that the internal

structure of the particles is independent of morphology and mass density.

- iii) The aggregation process has been shown from the fractal studies to consist of cluster-cluster formation. Nanopores are formed within small clusters, mesopores form between clusters and macropores form among clusters.

- iv) The photoconductive process is dominated by photo-holes. The model developed for the photoconductivity shows that the defects present in carbon aerogels act as recombination centres for photo-electrons. The decay times in aerogels are on the order of 20 seconds at low temperatures. These long decay times have been attributed to a screening effect. For the colloidal carbon aerogels, increases in density increase the magnitude of the observed photoconductivity, but also help to increase the recombination rate at higher temperatures. Heat-treatment is seen to enhance the recombination rate by effectively reducing the number of trap states in the system. The polymeric carbon aerogels exhibit a sharp peak in their photoconductivity response. This behaviour has tentatively been attributed to germinate recombination, but has yet to be proven mathematically.

- v) The transport properties of carbon aerogels are dominated by localization behaviour at low temperature (< 10 K). The conductivity follows a temperature dependence

$$\sigma = \sigma_0 \exp[-\sqrt{T_0/T}] \tag{5.1}$$

in this regime. The particles in the carbon aerogel system act as localization sites. The transport is then dominated by free-carrier-type behaviour within the particles, and variable range hopping (Coulomb gap) between particles at low temperatures. At higher temperatures, the transport between the particles is activated.

5.2 Future Work

- i) Focus should be addressed to the TEM analysis of the micropore and nanopore distributions in the carbon aerogel system. The analysis employed in Section 2.3.3 for the mesopores can be used again to determine the fractal nature of these smaller pores. The effects of heat-treatment are surmised to cause pore collapse within the grains. It would be interesting to see the effect this collapse has on the fractal dimension, D.

- ii) Small-angle X-ray scattering and bulk moduli experiments have shown that there is doubt as to whether the particles in the carbon aerogel form a fractal system. The TEM studies done in this work have shown that the porous network exhibits fractal behaviour. Mathematical models should be carried out to investigate whether it is possible to have a system that can have fractal and non-fractal states co-existing.

- iii) It is conceivable that a new line of experiments could be conducted on the PF-based carbon aerogels. This thesis concentrated only on PF-based aerogels with high densities. More studies should be done on samples with $\rho_m < 0.4$ g/cm^3. Such studies would facilitate mapping out the insulator-metal transition regime in these materials. Also, heat-treatment effects could also be studied via Raman and magnetic susceptibility measurements.

Bibliography

[1] S. T. Mayer, R. W. Pekala, and J. L. Kaschmitter. The aerocapacitor: An electrochemical double-layer energy-storage device. *J. Electrochem. Soc.*, 140(2):446–451, Feb 1993.

[2] M. S. Ahmed and Y. A. Attia. Aerogels materials for photocatalytic detoxification of cyanide wastes in water. *J. of Non-Cryst. Solids*, 186:402–407, 1995. Fourth International Symposium on Aerogels, Berkeley, 1994.

[3] Joseph C. Farmer, David V. Fix, Gregory V. Mack, Richard W. Pekala, and John F. Poco. The use of capacitive deionization with carbon aerogel electrodes to remove inorganic contaminants from water. In *International Low Level Waste Conference*, Florida, 1995. to be published.

[4] R. W. Pekala and F. M. Kong. A synthetic route to organic aerogels - mechanism, structure, and properties. *J. Phys. (Paris) Coll. Suppl.*, 50:c4–33–c4–40, 1989.

[5] R. W. Pekala and F. M. Kong. Resorcinol-formaldehyde aerogels and their carbonized derivatives. *Polymer Preprints*, 30:221–223, 1989.

[6] A. Emmerling and J. Fricke. Small angle scattering and the structure of aerogels. *J. of Non-Cryst. Solids*, 145:113–120, 1992.

[7] J. D. LeMay, R.W. Hopper, L. W. Hrubesh, and R. W. Pekala. Low-density microcellular materials. *Mat. Res. Soc. Bull.*, 15(12):19–45, Dec 1990.

[8] R. W. Pekala, C. T. Alviso, F. M. Kong, and S. S. Hulsey. Aerogels derived from multifunctional organic monomers. *J. of Non-Cryst. Solids*, 145:90–98, 1992.

[9] Larry L. Hench and Jon K. West. The sol-gel process. *Chem. Rev.*, 90(1):33–72, 1990.

[10] R. W. Pekala. Organic aerogels from the polycondensation of resorcinol with formaldehyde. *J. of Mat. Sci.*, 24:3221–3227, 1989.

[11] G. C. Ruben, R. W. Pekala, T. M. Tillotson, and L. W. Hrubesh. Imaging aerogels at the molecular level. *J. of Mat. Sci.*, 27:4341–4349, 1992.

[12] R. W. Pekala, C. T. Alviso, X. Lu, J. Gross, and J. Fricke. New organic aerogels based upon a phenolic-furfural reaction. *J. of Non-Cryst. Solids*, 188(1,2):34–40, 1995. Fourth International Symposium on Aerogels, Berkeley CA, 1994.

[13] D. M. Smith, D. Stein, J. M. Anderson, and W. Ackerman. Preparation of low-density xerogels at ambient pressure. *J. of Non-Cryst. Solids*, 186:104–112, 1995. Fourth International Symposium on Aerogels, Berkeley CA, 1994.

[14] Amal Kumar Naj. Scientists close in on practical aerogels, insulation that's almost as light as air. In *The Wall Street Journal*, Mar 30 1995.

[15] P. Tsou. Silica aerogel captures cosmic dust intact. *J. of Non-Cryst. Solids*, 186:415, 1995. Fourth International Symposium on Aerogels, Berkeley CA, 1994.

[16] R. W. Pekala, S. T. Mayer, J. F. Poco, and J. L. Kaschmitter. Structure and performance of carbon aerogel electrodes. In C. L. Renschler, D. M. Cox, J. J. Pouch, and Y. Achiba, editors, *Novel Forms of Carbon II*, Materials Research Society symposium prooceedings vol. 349, page 79, Pittsburgh, 1994. Materials Research Society.

[17] X. Lu, M. C. Arduini-Schuster, J. Kuhn, O. Nilsson, J. Fricke, and R. W. Pekala. Thermal conductivity of monolithic organic aerogels. *Science*, 255:971–972, 1992.

[18] S. J. Gregg and K. S. W. Sing. *Adsorption, Surface Area and Porosity.* Academic Press, London, 1967.

[19] Manfred Schroeder. *Fractals, Chaos, Power Laws: Minutes from an Infinite Paradise.* W. H. Freeman and Co., New York, 1990.

[20] A. W. P. Fung, Z. H. Wang, K. Lu, M. S. Dresselhaus, and R. W. Pekala. Characterization of carbon aerogels by transport measurements. *J. of Mat. Res.*, 8(8):1875–1885, 1993.

[21] G. A. M. Reynolds, A. W. P. Fung, Z. H. Wang, M. S. Dresselhaus, and R. W. Pekala. Morphological effects on the transport and magnetic properties of polymeric and colloidal carbon aerogels. *Phys. Rev. B*, 50(24):18590–18600, 1994.

[22] D. A. Long. *Raman Spectroscopy.* McGraw-Hill International Book Co., New York, 1977.

[23] M. S. Dresselhaus and G. Dresselhaus. Light scattering in graphite intercalation compounds. In M. Cardona and G. Güntherodt, editors, *Light Scattering in Solids III*, volume 51, chapter 2, pages 3–57. Springer-Verlag, Berlin, 1982.

[24] Diane S. Knight and William B. White. Characterization of diamond films by Raman spectroscopy. *J. Mater. Res.*, 4(2):385–393, Mar/Apr 1970.

[25] P. C. Eklund, G. Dresselhaus, M. S. Dresselhaus, and J. E. Fischer. Raman scattering from in-plane lattice modes in low-stage graphite-alkali-metal compounds. *Phys. Rev. B*, 16(8):3330–3333, 1977.

[26] P. C. Eklund and K. R. Subbaswamy. Analysis of Breit-Wigner line shapes in the Raman spectra of graphite intercalation compounds. *Phys. Rev. B*, 20(12):5157–5161, 1979.

[27] U. Fano. Effects of configuration interaction on intensities and phase shifts. *Phys. Rev.*, 124(6):1866–1878, 1961.

[28] R. W. Pekala and C. T. Alviso. Novel forms of carbon. In C. L. Renschler, J. J. Pouch, and D. M. Cox, editors, *MRS Symposia Proceedings No. 270*, page 3, Pittsburgh, 1992. Materials Research Society.

[29] J. J. Chen, private communications.

[30] G. A. M. Reynolds, Z. H. Wang, M. S. Dresselhaus, A. W. P. Fung, and R. W. Pekala. Photoconductivity: A probe of defect states in carbon aerogels. *Phys. Rev. B*, 49(21):15027–15034, 1994.

[31] K. S. Krishnan. Magnetic anisotropy of graphite. *Nature*, 133:174–175, Feb 1934.

[32] N. Ganguli and K. S. Krishnan. The magnetic and other properties of the free electrons in graphite. *Proc. R. Soc. London*, 177:168–182, 1941.

[33] J. W. McClure. Diamagnetism of graphite. *Phys. Rev.*, 104(3):666–671, Nov 1956.

[34] J. W. McClure. Theory of diamagnetism of graphite. *Phys. Rev.*, 119(2):606–613, Jul 1960.

[35] R. W. Pekala, C. T. Alviso, and J. D. LeMay. Organic aerogels: A new type of ultrastructured polymer. In *Chemical Processing of Advanced Materials*, chapter 60, pages 671–683. John Wiley and Sons, Inc., New York, 1992.

[36] H. H. Wieder. Laboratory notes on electrical and galvanomagnetic measurements. In C. Laird, editor, *Materials Science Monographs*, volume 2. Elsevier Scientific, Amsterdam, 1979.

[37] M. Hosoya, G. Reynolds, M. S. Dresselhaus, and R. W. Pekala. Photoconductivity of carbon aerogels. *J. of Mat. Res.*, 8:811–819, 1993.

[38] Ping Sheng, E.K. Sichel, and J.L. Gittleman. Fluctuation-induced tunneling conduction in carbon-polyvinylchloride composites. *Phys. Rev. Lett.*, 40(18):1197–1200, 1978.

[39] A. W. P. Fung, Z. H. Wang, M. S. Dresselhaus, G. Dresselhaus, R. W. Pekala, and M. Endo. Coulomb-gap magnetotransport in granular and porous carbon structures. *Phys. Rev. B*, 49(24):17325–17335, 1994.

[40] B. I. Shklovskii and A. L. Efros. *Electronic Properties of Doped Semiconductors*, volume 45 of *Springer Series in Solid-State Sciences*. Springer-Verlag, New York, 1984.

[41] P. Delhaès. Positive and negative magnetoresistances in carbons. In Philip L. Walker, Jr., editor, *Chemistry and physics of carbon*, volume 7, pages 193–235. Marcel Dekker, Inc., New York, 1971.

[42] N. F. Mott. Conduction in glasses containing transition metal ions. *J. Non-Cryst. Solids*, 1:1–17, 1968.

[43] A. L. Efros and B. I. Shklovskii. Coulomb gap and low temperature conductivity of disordered systems. *J. Phys. C: Solid State Physics*, 8:L49–L51, 1975.

[44] H. Tokumoto, R. Mansfield, and M. J. Lea. Correlation effect in variable range hopping in n-InSb. *Solid State Comm.*, 35(12):961–964, 1980.

[45] P. Sheng, B. Abeles, and Y. Arie. Hopping conductivity in granular metals. *Phys. Rev. Lett.*, 31(1):44–47, 1973.

[46] B. Abeles, P. Sheng, M. D. Coutts, and Y. Arie. Structural and electrical properties of granular metal films. *Adv. Phys.*, 24:407, 1975.

[47] E. Šimánek. The temperature dependence of the electrical resistivity of granular metals. *Solid State Comm.*, 40:1021–1023, 1981.

[48] P. Sheng and J. Klafter. Hopping conductivity in granular disordered systems. *Phys. Rev. B*, 27(4):2583–2586, 1983.

[49] C. J. Adkins. Conduction in granular metals with potential disorder. *J. Phys. C: Solid State Phys.*, 20:235–244, 1987.

[50] R. W. Pekala, S. T. Mayer, J. L. Kaschmitter, and F. M. Kong. Carbon aerogels: An update on structure, properties, and applications. In Yosry A. Attia, editor, *Proceedings of the International Symposium on Advances in Sol-Gel Processing and Applications*, pages 369–377, New York, 1994. Plenum Press.

[51] R. W. Pekala, C. T. Alviso, and J. D. LeMay. Organic aerogels: microstructural dependence of mechanical properties in compression. *J. Non-Cryst. Solids*, 125:67–75, 1990.

[52] P. Nagels. *Amorphous Semiconductors*, volume 36 of *Topics in Applied Physics*. Springer-Verlag, Berlin, 1979.

[53] Albert Rose. *Concepts in Photoconductivity and Allied Problems*. Interscience Publishers, New York, 1963.

[54] J. P. Chausse and J. Hoarau. Calcul quantique de l'anisotropie magnètique de bandes graphitiques. *J. Chim. Phys.*, 66:1062–1072, 1969.

[55] J. Hoarau and G. Volpilhac. Theory of the diamagnetic susceptibility of condensed ring systems: Reinterpretation of diamagnetism of pregraphitic carbons. *Phys. Rev. B*, 14(9):4045–4053, 1976.

[56] S. Mrozowski. Electronic properties and band model of carbons. *Carbon*, 9(2):97–109, 1971.

[57] J. Mort and D. M. Pai, editors. *Photoconductivity and Related Phenomena*. North-Holland, Amsterdam, 1976.

[58] T. D. Moustakas and K. Weiser. Transport and recombination properties of amorphous arsenic telluride. *Phys. Rev. B*, 12(6):2448–2454, 1975.

[59] T. C. Arnoldussen, R.H. Bube, E.A. Fagen, and S. Holmberg. Analysis of photoconductivity in amorphous chalcogenides. *J. Appl. Phys.*, 43(4):1798–1807, 1972.

[60] W. Shockley and W. T. Read, Jr. Statistics of the recombinations of holes and electrons. *Phys. Rev.*, 87(5):835–842, 1952.

[61] T. Tiedje and A. Rose. A physical interpretation of dispersive transport in disordered semiconductors. *Solid State Comm.*, 37(1):49–52, 1981.

[62] N. F. Mott and E. A. Davis. *Electronic Processes in Non-Crystalline Materials.* Clarendon Press, Oxford, second edition, 1979.

[63] S. Ono and K. Sugihara. Theory of the transport properties in graphite. *J. Phys. Soc., Japan*, 21(5):861–868, 1966.

[64] W. N. Reynolds. *Physical Properties of Graphite.* Elsevier, Amsterdam, 1968.

[65] R. A. Street. *Hydrogenated Amorphous Silicon.* Cambridge solid state science series. Cambridge University Press, Cambridge, 1991.